Droplet impacts onto porous substrates: pre- and post-impact dynamics

Gavin Moreton

A thesis submitted to the University of East Anglia in partial fulfilment of the Doctor of Philosophy

University of East Anglia
School of Mathematics
July 2022

Abstract

In physical settings such as droplets impacting onto soils, ink-jet printing, concrete and tarmac, the substrate plays a significant role in altering the flow. Such droplet impacts can lead to a penetration of fluid into the substrate in an unwanted or uncontrolled manner. Better modelling of the fluid mechanics during impact is crucial to a better understanding the fate of the liquid.

During droplet impact onto an impermeable plate the air acts as a cushioning layer. Moments before contact the air layer is thin and its pressure high. The high pressure deforms the drop's free surface, forming an air bubble, which delays the droplet's impact. Introducing a porous substrate allows air to enter the substrate and alter the approach to impact. After impact the liquid splashes along the substrate's surface as a thin jet. Simultaneously, some liquid enters the substrate, slowing down the jet and increasing its thickness.

In chapters 2 and 3 we derive a mathematical model for an impact with an air cushioning layer onto an impermeable substrate, considering normal and oblique impacts with surface tension. Chapter 4 introduces a thin porous substrate. We couple the influence of the substrate through governing equations for the air and water, and we solve them numerically. Chapter 5 introduces deeper porous substrates: complex variable methods are used to couple the substrate behaviour with the gas and liquid governing equations. Chapter 6 begins to consider the post-impact dynamics. Here, for a

drop meeting an impermeable substrate, Wagner theory is applied, and we solve the problem analytically with complex analytical methods. Chapter 7 introduces a porous substrate. We derive a model that couples the substrate behaviour with the spreading of the droplet and the motion of the jet along the substrate surface. Chapter 8 contains conclusions and open questions.

Acknowledgements

I would like to thank both of my supervisors, Dr Richard Purvis and Dr Mark Cooker for their unparalleled support, guidance and knowledge during my studies. I was delighted when I found out I would be working with both of them. I would also like to think my friends and family for their support through my studies.

Contents

1

Thesis introduction

1.1 Physical motivation

There are several different scenarios, in natural and industrial settings, that motivate the research for this thesis. Three examples illustrate these. First, the impact of raindrops onto soil. The fluid mechanics of absorption and or splashing of one typical raindrop needs to be modelled to understand better the proportions of water involved in run-off and entry into the soil. Both processes contribute to soil erosion. How much water splashes on the top surface? Mouzai and Bouhadef (2003) discuss soil erosion from droplets with varying parameters such as diameter, kinetic energy and pressure with splash distance and the influence this has on the soil. Relationships between drop diameter and both drop diameter and soil splash indicated that the diameter of the droplet is an important characteristic.

A second scenario is from the paint-spray industry. Fine droplets of paint are thrown onto a solid surface in order to coat it. The solid may be smooth and impermeable, but very often the solid's surface is far from plane, containing indentations/irregularities, pillars or crevices, whose dimensions are similar to the droplets' diameters. The final form of the dried coating may depend on the mechanics of initial droplet impact and splashing. For ink jet printing, understanding the impact behaviour is vital in optimising the printing process: to obtain high-resolution images knowledge of the splash post-impact, and ways to reduce this splash to allow for more controlled

distribution of the ink. Moments before impact of a droplet, significant air cushioning changes the droplet's free-surface shape and allows a bubble to form in the droplet.

A third scenario, the freezing of water on an aircraft in flight, can involve liquid-water-coated ice particles initially hitting the metal surface of the wing. But once ice starts to build up on the wing, the subsequent particles impact an irregular, icy surface. This presents a complicated geometry in which to consider impact splashing. What proportion of the water stays on the wing to freeze? Gent et al. (2000) provide a review of how ice forms and the subsequent deterioration of aerodynamic performance. Their modelling process begins by looking at droplet trajectories from clouds, focussing on where and how frequently droplets impact the wing. After this is known, analysis of how much of this water freezes, and the location of the ice formations, can be done. It is with this information that the affects of the ice on the aerodynamic properties of the wing can be studied. Grizen et al. (2020) discusses engineered textured surfaces which are hydrophobic to delay the forming of ice. The application was on aluminium which has countless industrial uses, some of which are materials used in aircraft where icing can pose serious hazards.

1.2 Literature review

Despite impacts being studied for over a century these flows are not fully understood, Worthington and Cole (1900) were some of the first to document these impacts. Their photographs illustrated the bubble that is formed centrally below where the emerging column of liquid rebounds from the surface of the liquid. Splashing is a very complicated, multi-phased process which depends heavily on the surrounding fluids. No corona will form if the impact happens in a vacuum onto a smooth flat substrate, jets (thin layers of liquid) will still form on the surface of the substrate; Xu et al. (2005)

shows this occurrence with high speed photography. In that study different background air pressures were used, for the lowest pressure, there was very little splashing compared to higher pressures. Van Dam and Le Clerk (2004) report an experimental study for the impact of water droplets onto a solid substrate with emphasis on the splashing and spreading of the fluid. The radius of the air bubble was shown to have good agreement with previous numerical models. The spreading rate was found to be larger at later times which are related to the Weber and Reynolds numbers of the flows. Tan et al. (2007) used high-speed cameras to capture in great detail droplet impacts and the ice formation that occurred. Droplet generators were used to simulate water droplets impacting a moving object, in these experiments the objects were stationary and droplets were fired towards them. It is thought that ice particles covered with thin layers of water are also an important aspect. Observations of the impact splashing mechanisms and droplet deformations were captured by photography. Lee et al. (2012) use x-ray photography to capture the progression of the full impact at very small time intervals, this allowed the bubble formation, spreading and splash to be easily observed. Li and Thoroddsen (2015) capture the bubble formation as the droplet is descending. These experimental findings of the free surface shapes are compared to numerical predictions by Duchemin and Josserand (2011) in Josserand and Thoroddsen (2016) and show good agreement. During the later part of the impact (after contact is made) the spreading, jet formation and rebounding are photographed which can be seen in Bartolo et al. (2005). Brunet et al. (2009) show droplet impacts onto arrays of pillars and engineered hydrophobic and hydrophilic surfaces are considered and using photography stages of the impacts are captured. The images show small amounts of fluid which have entered the array and the rest of the droplet spreading across the surface. Hao et al. (2019) and Zhao et al. (2020) show different examples of jet formation in the early times of an impact, look-

ing at how to suppress a splash. Josserand and Thoroddsen (2016) present detailed experimental results for impacts onto both impermeable and more complicated substrates. Using photography, images for the progression of the spreading, jet formation and rebounding are captured at very small time intervals. Marston et al. (2010) uses glass beads to simulate a permeable powder as a more complicated substrate to observe an impact onto. Some of the liquid from the droplet impacting this surface was allowed to enter the matrix of voids between spherical glass beads while the rest spread over the surface of the beads. An experimental study of droplet impacts with hydrophobic concrete is Ramachandran et al. (2015). Photographs show the evolution of a falling droplet onto the concrete and the subsequent splash or bounce by the droplet. The behaviour of the droplet was determined by the velocity and Weber numbers of the incoming droplets, larger Weber numbers encouraged the droplets to bounce off the surface. Oblique impacts were considering in this study with the substrate at an angle, this change in the substrate encouraged the droplets to bounce rather than to spread.

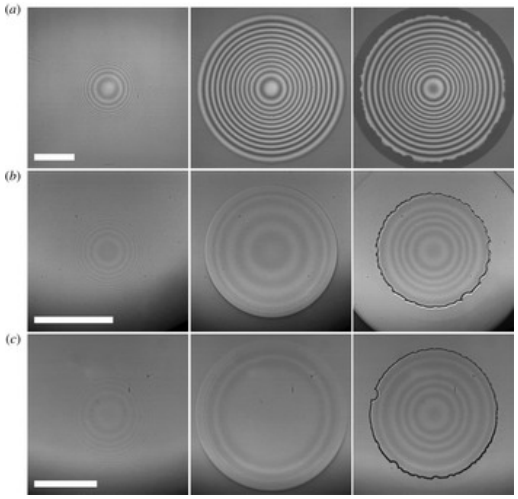

Figure 1.1: Photograph showing the spreading over time of a droplet over an impermeable substrate for different impact velocities, taken from Li and Thoroddsen (2015).

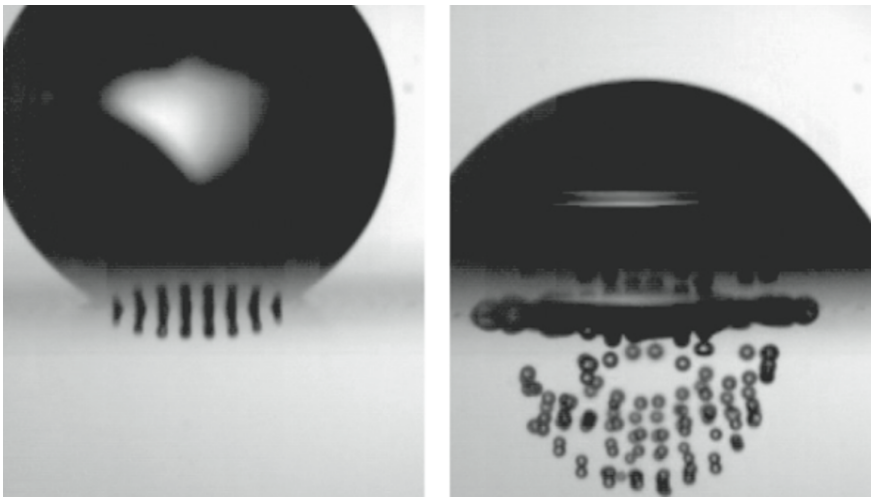

Figure 1.2: Droplet impacting a regular grate illustrating the smaller droplets produced under the grate from Brunet et al. (2009).

There are many theoretical studies of droplet impacts with an air cushioning layer. Wilson (1991) provides some early work with the model formulation of rigid body impact onto a liquid surface with air cushioning. Wilson assumes air and liquid are inviscid. They give both numerical and analytic solutions for the coupled equations, including inertia, which they derive. Wilson begins by non-dimensionalalising Euler's equations to simplify them before making some analytic progress by considering asymptotic solutions assuming very small times. Smith et al. (2003) build on the work by Wilson and extend the theory. In their study we have a droplet of inviscid liquid, approaching a solid wall, with an air layer between them. The air layer is assumed viscous so this differs from previous work by Wilson. From the derivations with zero viscosity in the air layer (so the Reynolds number is much greater than one) the equations in Wilson (1991) are recovered. Smith et al. (2003) report numerical results for solving the coupled equations, which are similar to those in the inviscid air layer. Analytical results close to touchdown are formulated and local solutions of the free-surface and pressure are given, a high local pressure peak close to touchdown matches

with the numerical findings. A further extension comes from Purvis and Smith (2004b): here surface-tension effects and post-impact analysis are considered. An alternative set of coupled equations, incorporating surface tension, are derived and solved numerically. The addition of surface tension alters one of the coupled equations and comes from the discontinuity in pressure across the air-water interface, this added effect causes a significant delay in touchdown.

Further work on droplet impacts includes an extension of earlier two-dimensional work given in Hicks and Purvis (2010) by solving the derived coupled equations in a three-dimensional geometry, these governing equations were formulated by non-dimensionalising the three-dimensional Navier-Stokes equations. The numerical results shown were axi-symmetric (for a normal impact). Further extension to this three-dimensional model considered substrates with different topographies and the resulting changes in the free-surface and pressure plots. In addition to this the bubble size was predicted. From the numerical results a non-dimensional bubble size could be found and the scalings undone to obtain a realist prediction for a bubble size. These radii had good agreement with previous experimental work. Surface tension is neglected from the study in Hicks and Purvis (2010). Obliqueness is the inclination, away from the normal, of the velocity vector of the droplet during its approach towards impact. Obliqueness is included and numerical solutions for a droplet impacting a moving plate are given as a parameter. Oblique impacts have one side of the droplet accelerate into impact faster than the other, so there is no trapped bubble.

Another extension of the simple model given in Hicks and Purvis (2011) gives solutions for droplets impacting other droplets, and liquid layers with air cushioning. These models are similar to the previously mentioned papers. Hicks and Purvis (2011) considers liquid-liquid impacts as opposed to liquid-solid impacts. There are parameters of liquid layer depth and the ratio of

the two droplet radii which can vary. Numerical results here show the free-surface and pressure distribution for various values of these parameters. Obliqueness and surface tension are neglected in this study.

Concerning the impacts of solids with water layers we have: Korobkin (1999) where a solid box entering a thin layer of liquid and the liquid flow and the jets are calculated. Asymptotic methods were used to derive equations to describe the flow in multiple local regions around the solid body. Further studies on this subject include Korobkin et al. (2008). They studied a solid object impacting a thin layer of water on an impermeable substrate. Surface tension and obliqueness are omitted in this study. Numerical results, as well as an analytical model for the motion close to touchdown were given. The key difference between the coupled equations for shallow-water and deep-water is the deep-water fluid equation involves a global relation between the free-surface and pressure distribution, however, the shallow-water fluid equation involves a local relation. Another study that consider impacts between solid and shallow water layers is Hicks and Smith (2011). In this study the impact and the rebound of a solid impacting a shallow water layer is investigated. The solid is coming towards the liquid layer at an oblique angle and rebounds disturbing the liquid layer. Vanden-Broeck and Smith (2008) considers a the effect of surface tension between two fluids near a wall. Periodic and non-period solutions were found for the effects of surface tension on the approaching fluids.

Very little theoretical study has been made on porous impacts. A study group report Parker and Nally (2012) investigated a basic model of a droplet impact with a porous media, by taking the very basic assumption that the pressure caused by the impact is uniform across the wetted region of impact. Hicks and Purvis (2015) study the air cushioning of a droplet impacting onto a porous substrate, with parameters for porosity and depth of the porous substrate. The porous medium is considered here to be a dense array of

identical pillars. Pressures across the air and bubble volumes were found to be lower than an impact onto an impermeable substrate due to air being able to pass into the substrate.

After the droplet has impacted the substrate a new system needs to be formulated to govern the spreading of the droplet. This theory was first studied in the context of ship slamming in Von Karman (1929). Some time later Wagner modified the system posed by Von Karman in Wagner (1932). Here Wagner accounted for the displaced liquid (the rising water level) in the description of the edges of the wetted regions. Water entry problems have been widely studied in Wilson (1989) and Howison et al. (1991), here we have the impacts of solids with small deadrise angles into bodies of fluid. More recently Oliver has revisited the work in Wagner (1932) by formally deriving the Wagner condition asymptotically in Oliver (2002) by considering the multiple regions in this problem and matching the solutions in each region using asymptotic methods. They also extended the theory by considering second-order corrections in Oliver (2007). Moore (2014) primarily uses asymptotic methods for formulating and solving the systems for droplet impacts. They extend Wagner theory with an oblique impact and formulates and solves this problem numerically. Also they consider the impact problem with air cushioning present and the leading order solution is found.

This thesis addresses the fundamental fluid mechanics of impact of droplets onto porous solids, in mathematical terms. We consider the initial penetration of fluid into a solid target driven by the large transient liquid pressures associated with sudden impact. We treat the problems isothermally, so that freezing, thawing and heat-transfer are all neglected and the droplets are assumed to be small. The porous media is assumed to be an array of identical pillars with pores smaller than the droplets. The droplet-impact speeds are relatively low. These assumptions allow us to treat the liquid flow outside and within the porous medium as an incompressible continuum. The

more complicated compressible air flow is discussed below. The duration of impact is very short and we treat only the initial stages of impact during which the contact line moves a distance smaller than the droplet's diameter, and while the impact pressures remain high. The brief high pressures are associated with the liquid flow being inertial. Viscosity plays an important role in the air layer between the droplet and the solid before impact.

1.3 Thesis structure

Chapters 2,3,4 and 5 concern the presence of an air layer in the pre-impact stage of dynamics. Later chapters model the post-impact dynamics - the flow after the liquid drop has made contact with the substrate. In chapter 2 we first set up the basic modelling assumptions which are key to all problems considered in this thesis. We then move on to consider the specific problem for the deep-water droplet impacts onto an impermeable substrate, where we nondimenionalise and derive the governing equations. Then we look at two additional physical features of the problem: obliqueness and surface tension. Coupled equations (ODEs with suitable boundary and initial conditions) are derived and computational results are displayed and discussed. In Chapter 3 we consider impacts of shallow-water layers onto impermeable substrates. We begin by deriving the coupled equations for the simplest type of substrate - an impermeable rigid flat plate. We then add obliqueness to the problem which hasn't been considered before. Chapter 4 considers another new case where we introduce a thin porous substrate into the problem. The governing equations are derived and new results are presented. Chapter 5 explores the problem where we have thicker layers of the porous media, we use complex analytical methods to couple the substrate to the air layer and solve the problem numerically.

Chapter 6 begins to look at the post-impact dynamics. Initially a literature review is given to outline previous work done in the field. Then we

consider formulating the problem of an impact with an impermeable substrate. This is solved analytically and results are presented and discussed. Chapter 7 introduces a porous substrate to this post-impact problem. The governing equations are formulated and solved numerically. Further analysis is done looking at the jet region formed along the surface of the substrate. In Chapter 8 we conclude the thesis and provide more complicated models for the inclusion of a porous layer in the post-impact analysis covered in Chapter 7 left as open questions.

2

Cushioning of deep water impact with an impermeable substrate

2.1 Introduction and literature review

This chapter examines an inviscid body of liquid, bounded by a free surface approaching a wall or substrate, with another region consisting of a gas, air, in between. As the distance between the liquid domain and wall decreases, the free-surface of the water become deformed by the cushioning air layer. The deformation is caused by rising pressures across the air layer; this rise in pressure is caused by the narrowing of the air layer between the droplet and the substrate or wall. This can lead to the trapping of a bubble of air. Experimental evidence for this comes from Lesser and Field (1983) who photographed these bubble formations. The air cushioning decelerates the centre of the droplet, causing the sides of the droplet to touchdown first, which causes a bubble to be entrapped. A more recent study of bubble formations comes from Hicks et al. (2012). Solid impermeable rigid discs were dropped into water such that the circular face of each disc made normal impact with the initially plane water surface. High speed photography was used to record the spread of the wetted surface on the discs and hence the dry region indicated the position of the bubble. Comparisons were made to theoretical work carried out in Hicks and Purvis (2010) showing good agreement between experimental and theoretical results.

Experimental studies on droplets impacting a liquid surface can be seen in Thoroddsen et al. (2003) and impacts on a solid surface are presented in Thoroddsen et al. (2005); both papers show examples of entrapped bubbles. The results from the pre-impact analysis provide the initial conditions for the post-impact behaviour. The bubble formation and multiple touchdown positions may potentially add interesting changes to post-impact models.

In all the physical problems described above the common theme is the influence of the air layer. The modelling of the air layer (and the role of the air in the porous layer when considering permeable substrates) is important in understanding the droplet impacts in these physical problems. We define, for a droplet, the word *touchdown* to mean the instant when the droplet's *free surface* makes contact with the substrate.

2.1.1 Modelling assumptions

We assume the liquid and air layers are both incompressible Newtonian fluids, the model can be extended to include compressible air effects, see Hicks and Purvis (2013) for details. For simplicity we will only consider flows in two spatial dimensions. The assumptions underlying the derivations made here carry over readily into both axi-symmetric and fully three-dimensional geometries. Another significant assumption is that the typical impact speed is much less than the speed of sound in air (340 ms^{-1}) in these situations. Hence the Mach number for the air phase has a low value much less than one (and an even lower Mach number in the water phase, where the sound speed is about 1500ms^{-1}). Hence the air and water can be treated simply as two incompressible fluids. Scales for the various quantities follow from an order of magnitude argument close to impact. For this chapter starred quantities denote dimensional variables: $\mathbf{u}^*$ is the dimensional velocity of the fluid, p^* is the dimensional pressure, ρ^* is the density of the fluid, ν^* is the kinematic viscosity of the fluid. The subscript w refers to quantities

relating to the water and a refers to quantities relating to the air. Every other subscript is a derivative with respect to the variable denoted by the subscript. The y^* axis points vertically upwards, the x^* axis is horizontal, the origin lies directly below the centre of the droplet. Let R be the radius of curvature of the free surface at the point of expected first contact in impact. U is the relative speed of approach of the droplet, and we assume this is also the velocity scale for the air. The liquid is incompressible and the gas can be assumed incompressible due to the low Mach number. Throughout this thesis we are neglecting gravity.

We begin by non-dimensionalising the two-dimensional, incompressible form of the Navier-Stokes equations, we apply these equations to both air and water.

$$\mathbf{u}^*_{t^*} + (\mathbf{u}^* \cdot \nabla)\mathbf{u}^* = -{\rho^*}^{-1}\nabla p^* + \nu^* \nabla^2 \mathbf{u}^*, \tag{2.1}$$

$$\nabla \cdot \mathbf{u}^* = 0, \tag{2.2}$$

with the following scales:

$$(\mathbf{u}^*_w, p^*_w, x^*, y^*, t^*) = \left(U\mathbf{u}_w, \rho_w U^2 p_w, Rx, Ry, \frac{R}{U}t\right), \tag{2.3}$$

$$(\mathbf{u}^*_a, p^*_a, x^*, y^*, t^*) = \left(U\mathbf{u}_a, \rho_w U^2 p_a, Rx, Ry, \frac{R}{U}t\right). \tag{2.4}$$

Thus we obtain:

$$\frac{U^2}{R}\mathbf{u}_{w_t} + \frac{U^2}{R}(\mathbf{u}_w \cdot \nabla)\mathbf{u}_w = -\frac{U^2\rho_w}{R\rho_w}\nabla p_w + \frac{U\nu_w}{R^2}\nabla^2\mathbf{u}_w, \tag{2.5}$$

$$\frac{U^2}{R}\mathbf{u}_{a_t} + \frac{U^2}{R}(\mathbf{u}_a \cdot \nabla)\mathbf{u}_a = -\frac{\rho_w U^2}{R\rho_a}\nabla p_a + \frac{U\nu_a}{R^2}\nabla^2\mathbf{u}_w. \tag{2.6}$$

Rearranging and defining the water's Reynolds number to be $Re = \frac{UR}{\nu_w}$ we have the governing equations for the water and air layers:

$$\mathbf{u}_{w_t} + (\mathbf{u}_w \cdot \nabla)\mathbf{u}_w = -\nabla p_w + {Re_w}^{-1}\nabla^2\mathbf{u}_w, \tag{2.7}$$

$$\mathbf{u}_{a_t} + (\mathbf{u}_a \cdot \nabla)\mathbf{u}_a = -\frac{\rho_w}{\rho_a}\nabla p_a + \frac{\nu_a}{\nu_w}{Re_w}^{-1}\nabla^2\mathbf{u}_a. \tag{2.8}$$

We also have the conservation of mass equations which have identical forms after substituting in both sets of scales and rearranging:

$$\nabla \cdot \mathbf{u}_a = 0, \qquad \nabla \cdot \mathbf{u}_w = 0. \tag{2.9}$$

Our boundary conditions are the kinematic condition and the normal stress condition:

$$v_w^* = F_t^* + u_w^* F_x^* \qquad \text{on } y^* = F^*, \tag{2.10}$$

$$p_a^* = p_w^* - \sigma \frac{{F^*}_{x^* x^*}}{\left(1 + ({F^*}_{x^*})^2\right)} \qquad \text{on } y^* = F^*, \tag{2.11}$$

where the droplet has a lower free surface given by $y^* = F^*(x^*, t^*)$. We are also assuming that the ratios $\frac{\rho_a}{\rho_w}$ and $\frac{\mu_a}{\mu_w}$ are small, (taking approximate values at 20^oC and one atmosphere of pressure) 1.2×10^{-3} and 1.8×10^{-2} to two significant digits. We are assuming large Reynold number flows so the ratio $\frac{\nu_a}{\nu_w Re_w}$ is very small.

2.2 Equations for the droplet

Consider a droplet of water, falling towards a rigid horizontal surface (at $y^* = 0$) see Figure 2.1. The droplet has a lower free surface given by $y^* = F^*(x^*, t^*) \geq 0$. We introduce $\epsilon \ll 1$.

In order to have deformation of the free-surface the air pressure needs to be sufficiently high which doesn't happen until the air gap is very thin. The air pressure needs to become large enough to be comparable to the pressure in the water. As the air layer gets very thin the continuum assumption breaks down and other effects such as the gas kinetic effects become more important, see Chubynsky et al. (2020). Close to impact we will take a more local view and scale our spatial coordinates by ϵ, the velocity to be that of the droplet falling and the time scale to be that time taken to fall the distance of the small air gap hence we apply the following scales to (2.7)

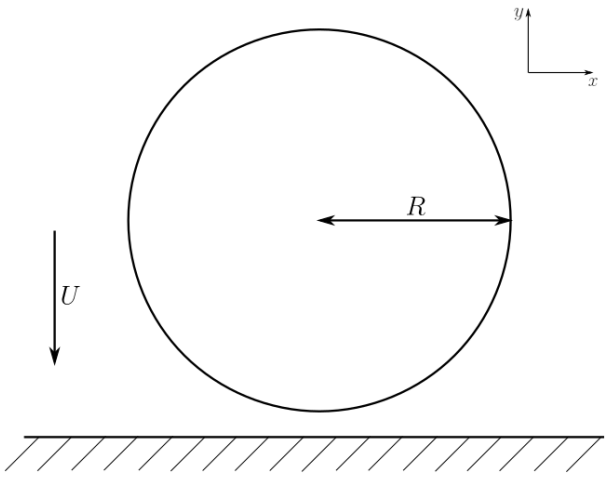

Figure 2.1: Diagram showing schematic of the problem to be solved, the origin of the axis is below the centre of the sphere.

and (2.9):

$$(\mathbf{u}_w^*, p_w^*, x^*, y^*, t^*) = \left(\mathbf{u}_w, \mathcal{P}_w p_w, \epsilon x, \epsilon y, \epsilon^2 t\right), \tag{2.12}$$

the scale for the pressure is unknown and is to be determined. After substituting in the scales we obtain:

$$\epsilon^{-2}\mathbf{u}_{w_t} + \epsilon^{-1}\left(\mathbf{u}_w \cdot \nabla\right)\mathbf{u}_w = -\mathcal{P}_w\epsilon^{-1}\nabla p_w + {Re_w}^{-1}\epsilon^{-2}\nabla^2\mathbf{u}_w, \tag{2.13}$$

$$\epsilon^{-1}\nabla \cdot \mathbf{u}_w = 0. \tag{2.14}$$

After rearrangement we have non-dimensional field equations (which are valid in the water droplet):

$$\mathbf{u}_{w_t} + \epsilon\left(\mathbf{u}_w \cdot \nabla\right)\mathbf{u}_w = -\epsilon\mathcal{P}_w\nabla p_w + {Re_w}^{-1}\nabla^2\mathbf{u}_w, \tag{2.15}$$

$$\nabla \cdot \mathbf{u}_w = 0. \tag{2.16}$$

The Reynolds number is large compared with unity, if we assume our droplet radius is approximately $0.001 - 0.1$m and impact velocity approximately $1 - 10\text{ms}^{-1}$ we have $Re_w > 10^3$.

This results in the viscous terms being small compared to unity. An alternative case is to have inviscid water and air, derived by Wilson (1991)

this happens for $Re = O(10^7)$. To achieve balance of terms in (2.15), to have a non-trivial equation we have the pressure scale as $\mathcal{P}_w = O(\epsilon^{-1})$ (so the pressure is present in the leading order and matches with the air layer). Taking the leading order $O(\epsilon^0)$ terms in (2.15) -(2.16), we have:

$$\mathbf{u}_{w_t} = -\nabla p_w, \tag{2.17}$$

$$\nabla \cdot \mathbf{u}_w = 0. \tag{2.18}$$

Separating the components of (2.17) and (2.18), we have three equations:

$$u_{w_t} = -p_{w_x}, \tag{2.19}$$

$$v_{w_t} = -p_{w_y}, \tag{2.20}$$

$$u_{w_x} + v_{w_y} = 0. \tag{2.21}$$

These are the linearised Euler equations. Equations (2.19) - (2.21) also need to satisfy suitable boundary conditions. First is the kinematic condition on the free surface ($y = F(x,t)$) of the droplet. The dimensional version of this kinematic condition is given in (2.10), after non-dimensionalising and retaining the leading order terms we have:

$$v_w = F_t \qquad \text{on } y = 0. \tag{2.22}$$

The second boundary condition is the linearised normal stress condition, namely:

$$p_a = p_w - \sigma F_{xx} \qquad \text{on } y = F, \tag{2.23}$$

where:

$$\sigma = \frac{\sigma^* \epsilon^2}{RU^2 \rho_w}, \tag{2.24}$$

is the scaled surface tension coefficient (where σ^* is the surface-tension coefficient) note that this is order ϵ^2 and thus is very small. Surface tension is negligible until we have very large curvatures which occur close to touchdown after significant deformations by the air layer. If $\sigma = 0$ we see that the

pressure is continuous across the free surface. For the rest of the derivation we assume the effect of surface tension is negligible as we have shown it is very small compared to unity. From (2.19) - (2.21) we can see that v_{w_t} and p_{w_x} satisfy the Cauchy-Riemann relations, so we can define a complex function, $w(z,t) = p_{w_x} + iv_{w_t}$ with $z = x + iy$ and applying Cauchy's integral formula we have:

$$(p_{w_x} + iv_{w_t}) = \frac{1}{2\pi i}\int_{-\infty}^{\infty} \frac{p_{w_\zeta} + iv_{w_t}}{\zeta - z} d\zeta. \tag{2.25}$$

Taking the imaginary part and evaluating at $y = 0$ we have $z = x$ and now we have a singularity at $\zeta = x$ which will give us a principal value integral (PV):

$$-v_{w_t} = \frac{1}{\pi} PV \int_{-\infty}^{\infty} \frac{-p_{w_\zeta}}{\zeta - x} d\zeta, \tag{2.26}$$

and finally after the substitution of (2.22) into (2.26) we arrive at:

$$F_{tt} = \frac{1}{\pi} PV \int_{-\infty}^{\infty} \frac{p_{w_\zeta}}{\zeta - x} d\zeta. \tag{2.27}$$

2.3 Equations for the air layer

Close to impact in the air layer we expect disparate horizontal and vertical length scales due to needing a thin air gap to create a high pressure and trigger a deformation. We expect the horizontal scale to be comparable to the droplet's scale and a vertical scale an order of magnitude smaller, until this point the air pressure is not large enough to cause deformation. The time scale remains the same as with the droplet scale, from the continuity equation we have disparate velocity scales. We start from equations (2.8) and (2.9) but now for the air, and we apply the following scales:

$$(\mathbf{u}_a^* = (u_a^*, v_a^*), p_a^*, x^*, y^*, t^*) = \left(\mathbf{u}_a = (\epsilon^{-1}u_a, v_a), \mathcal{P}_a p_a, \epsilon x, \epsilon^2 y, \epsilon^2 t\right), \tag{2.28}$$

where $\mathcal{P}_a$ is the air scale to be found. Substituting these scaled variables into (2.12) and (2.13), and looking at each component individually, we obtain:

$$\epsilon^{-3}u_{a_t} + \epsilon^{-3}\left(u_a u_{a_x} + v_a u_{a_y}\right) = -\frac{\mathcal{P}_a\rho_w}{\rho_a\epsilon}p_{a_x} + \frac{\nu_a}{\nu_w\epsilon^3 Re}u_{a_{xx}} + \frac{\nu_a}{\nu_w\epsilon^5 Re}u_{a_{yy}}, \tag{2.29}$$

$$\epsilon^{-2}v_{a_t} + \epsilon^{-2}\left(u_a v_{a_x} + v_a v_{a_y}\right) = -\frac{\mathcal{P}_a\rho_w}{\rho_a\epsilon^2}p_{a_y} + \frac{\nu_a}{\nu_w\epsilon^2 Re}v_{a_{xx}} + \frac{\nu_a}{\nu_w\epsilon^4 Re}v_{a_{yy}}, \tag{2.30}$$

$$\epsilon^{-2}u_{a_x} + \epsilon^{-2}v_{a_y} = 0. \tag{2.31}$$

After rearrangement we have:

$$\epsilon^{2}u_{a_t} + \epsilon^{2}\left(u_a u_{a_x} + v_a u_{a_y}\right) = -\frac{\mathcal{P}_a\rho_w\epsilon^4}{\rho_a}p_{a_x} + \frac{\epsilon^2\nu_a}{\nu_w Re}u_{a_{xx}} + \frac{\nu_a}{\nu_w Re}u_{a_{yy}}, \tag{2.32}$$

$$\epsilon^{2}v_{a_t} + \epsilon^{2}\left(u_a v_{a_x} + v_a v_{a_y}\right) = -\frac{\mathcal{P}_a\rho_w\epsilon^2}{\rho_a}p_{a_y} + \frac{\nu_a\epsilon^2}{\nu_w Re}v_{a_{xx}} + \frac{\nu_a}{\nu_w Re}v_{a_{yy}}, \tag{2.33}$$

$$u_{a_x} + v_{a_y} = 0. \tag{2.34}$$

We can see from equation (2.32) we can balance the pressure gradient with viscous force, $u_{a_{yy}}$. In order to satisfy the dynamic free-surface condition we must have $\mathcal{P}_a = \mathcal{P}_w$ hence $\mathcal{P}_a = O(\epsilon^{-1})$, thus to balance the pressure gradient with the viscous force we must have $\frac{\rho_w\epsilon^3}{\rho_a} = \frac{\nu_a}{\nu_w Re}$, this gives us an expression for ϵ, namely:

$$\epsilon^3 = \frac{\nu_a\rho_a}{\nu_w\rho_w Re} = \frac{\mu_a}{UR\rho_w}. \tag{2.35}$$

The dynamic viscosity and water density are fixed material constants, for ϵ to be small, $\epsilon < 0.1$, then we must have $UR > 10^{-2}$ m^{2}s^{-1}. Taking leading order of equations (2.32) - (2.34) we have:

$$0 = -p_{a_x} + u_{a_{yy}}, \tag{2.36}$$

$$-p_{a_y} = 0, \tag{2.37}$$

$$u_{a_x} + v_{a_y} = 0, \tag{2.38}$$

these are the lubrication equations. The boundary conditions for the air are a no-slip condition between the air and water phases, and secondly at the air-water interface the two fluids share the same normal component of velocity. The third condition is the kinematic condition on the free surface of the droplet. These conditions are:

$$u_w^* = u_a^*, \tag{2.39}$$

$$v_w^* = v_a^*, \tag{2.40}$$

$$v_a^* = F_{t^*}^* + u_a^* F_{x^*}^*, \tag{2.41}$$

on $y^* = F^*$. After applying the appropriate scales and taking the leading order we have the following boundary conditions for the non-dimensional problem:

$$u_a = 0, \tag{2.42}$$

$$v_w = v_a, \tag{2.43}$$

$$v_a = F_t, \tag{2.44}$$

on $y = F$.

For a rigid impermeable substrate we also have a fourth boundary condition on the air flow, a no-slip condition on the substrate at $y = 0$ namely:

$$u_a = 0 \qquad \text{and} \qquad v_a = 0 \qquad \text{on } y = 0. \tag{2.45}$$

The second equation will change for a flexible, porous or moving substrate.

From (2.37), p_a has no dependence on y, so we can integrate (2.36) directly twice with respect to y, thus giving us in the air layer:

$$u_a(x, y, t) = p_{a_x}(x, t)\frac{y^2}{2} + Ay + B, \tag{2.46}$$

where $A = A(x, t)$ and $B = B(x, t)$ are functions to be determined. Applying the no-slip condition on the substrate it follows that $B = 0$. Applying (2.42)

we find that $A(x,t) = -\frac{F}{2}p_{a_x}$, we now have an expression for u_a in terms of y, the pressure and the free surface, namely:

$$u_a(x,y,t) = \frac{p_{a_x}y}{2}\left(y - F\right). \tag{2.47}$$

Differentiating (2.47) with respect to x we obtain an expression for u_{a_x}. Substituting this into (2.37) and integrating with respect to y, we obtain an expression for v_a:

$$v_a(x,y,t) = \frac{p_{a_{xx}}y^2}{12}\left(3F - 2y\right) + \frac{p_{a_x}F_x y^2}{4} + C(x,t), \tag{2.48}$$

where $C(x,t)$ is another function to be found. After applying the no-slip condition (2.45) at $y = 0$, we find that $C = 0$ thus:

$$v_a(x,y,t) = \frac{p_{a_{xx}}y^2}{12}\left(3F - 2y\right) + \frac{p_{a_x}F_x y^2}{4}. \tag{2.49}$$

We now apply condition (2.44) on $y = F$, to obtain:

$$F_t = \frac{p_{a_{xx}}F^2}{12}\left(3F - 2F\right) + \frac{p_{w_x}F_x F^2}{4}, \tag{2.50}$$

$$F_t = \frac{1}{12}\left(p_{a_x}F^3\right)_x. \tag{2.51}$$

We have that $p_a = p_w$ on the interface so their x-derivatives are equal. To summarise, the coupled equations governing the air layer during droplet impact are:

$$F_t = \frac{1}{12}\left(p_{a_x}F^3\right)_x, \tag{2.52}$$

$$F_{tt} = \frac{1}{\pi}\int_{-\infty}^{\infty}\frac{p_{a_\zeta}}{\zeta - x}d\zeta. \tag{2.53}$$

We have assumed there is no surface tension present, so from (2.23) $p_a = p_w$ at the air-water interface. We can see that the right-hand side of (2.53) is simply the Hilbert transform of p_{a_x}. These model equations are valid for all t. We have initial free surface conditions of:

$$F(x,t) = \frac{x^2}{2} - t \qquad \text{as } t \to -\infty, \tag{2.54}$$

$$p(x,t) \to 0 \qquad \text{as } t \to -\infty, \tag{2.55}$$

$$p(x,t) \to 0 \qquad \text{as } x \to \pm\infty. \tag{2.56}$$

2.3.1 Additions to model

A term for surface tension can be added by a substitution of (2.23) into (2.53) giving:

$$F_{tt} = \frac{1}{\pi}\int_{-\infty}^{\infty} \frac{p_{a_\zeta} + \sigma F_{\zeta\zeta\zeta}}{\zeta - x} d\zeta. \tag{2.57}$$

We can also model an oblique impact of the droplet onto the substrate. By moving in a frame of reference translating horizontally to the left with the water droplet the flat plate has a constant horizontal velocity, c^*, to the right. From the non-dimensionalising this is only applicable for very large angles of obliqueness, for smaller angles, one will see little to no effect given the difference of orders of magnitude. In order to have this present at leading order $c^* = O(\epsilon^{-1})$. This only alters the no-slip condition for the horizontal velocity component of the air, (2.45). Starting from (2.46), however, we have:

$$u_a = c \qquad \text{on } y = 0, \tag{2.58}$$

where $c = \frac{U_{plate}}{U}$ (U_{plate} is the plate velocity). This gives us $B = c$ and $A = -\left(\frac{c}{F} + p_{a_x}\frac{F}{2}\right)$, hence the expression for u_a is:

$$u_a = \frac{p_{a_x} y}{2}(y - F) + c\left(1 - \frac{y}{F}\right). \tag{2.59}$$

After proceeding the same way as before, we alter (2.51) to:

$$F_t = \frac{1}{12}\left(P_{a_x} F^3\right)_x - cF_x, \tag{2.60}$$

where c is the scaled velocity of the plate given above.

2.4 Computational results and discussion

The coupled equations (without surface tension) are solved by discretizing (2.53) using implicit finite differences, third order in time and second order in space, this provided a good balance between accuracy and runtime, increasing these orders made little change to the results. Let I be the current

spatial grid point and J be the current time step, δt is the time step, δx is grid size, so we have:

$$F(I,J) = \frac{12}{35}\left(\frac{26}{3}F(I,J-\delta t) - \frac{19}{2}F(I,J-2\delta t) + \frac{14}{3}F(I,J-3\delta t) - \frac{11}{12}F(I,J-4\delta t) + \frac{(\delta t)^2}{\delta x}\mathcal{H}\left(\frac{1}{12}P(I-2\delta x,J) - \frac{2}{3}P(I-\delta x,J) + \frac{2}{3}P(I+\delta x,J) - \frac{1}{12}P(I+2\delta x,J)\right)\right), \tag{2.61}$$

where $\mathcal{H}$ is the Hilbert transform. We discretise (2.60) in a similar way:

$$\begin{aligned}&\frac{1}{12}F(I,J-2\delta t) - \frac{2}{3}F(I,J-\delta t) + \frac{2}{3}F(I,J+\delta t)\\ &- \frac{1}{12}F(I,J+2\delta t) + \frac{c\delta t}{\delta x}\left(\frac{1}{12}F(I-2\delta x,J) - \frac{2}{3}F(I-\delta x,J)\right.\\ &\left.+\frac{2}{3}F(I+\delta x,J) - \frac{1}{12}F(I+2\delta x,J)\right)\\ &= \frac{\delta t}{12(\delta x)^2}\left[\left(F^3(I-\delta x,J)+F^3(I,J)\right)\left(P(I-\delta x,J)-P(I,J)\right)\right.\\ &\left.-\left(F^3(I,J)+F^3(I+\delta x,J)\right)\left(P(I,J)-P(I+\delta x,J)\right)\right].\end{aligned} \tag{2.62}$$

In the results a time step $\delta t = 10^{-3}$ with 4001 x values are used, with the boundaries for the computation being at $\pm x_{\max}$, typically we use $x_{\max} = 32$ this is where the boundary conditions are applied increasing this number has little affect on the results, this gives the grid size of $\delta x = 0.016$. We start our calculations at $t = -12$, this is sufficiently far to assume an undisturbed free-surface, after testing being further away from the substrate no changes were seen in results. At the new time step we use (2.61) to guess the updated free-surface shape and use this to update the pressure using (2.62). We iterate this process until we have convergence. Convergence is achieved when after substituting in the guess of the free-surface and the updated pressure into (2.62) we have a relative error of less than 10^{-4}, and this happens in fewer than 20 iterations. The relative error is the ratio of the absolute error to the

order of magnitude of separation distance between the free surface and the substrate, we scale this because a small perturbation closer to touchdown is more significant than a small perturbation earlier on in the simulation. However, if surface tension is included this method isn't as effective unless the grid is very fine which drastically increases runtime, so an alternative method is used.

An alternative method is to use truncated Fourier series approximations for the pressure and free-surface, and again the equations are iterated. We approximate our functions of free surface position and pressure as Fourier series approximations with N terms in the series for $-x_{\max} \leq x \leq x_{\max}$ and the same grid size and time step:

$$f(x,t) = \sum_{n=1}^{N} F_n(t) \cos\left(\frac{n\pi x}{x_{\max}}\right), \tag{2.63}$$

$$p(x,t) = \sum_{n=1}^{N} P_n(t) \cos\left(\frac{n\pi x}{x_{\max}}\right), \tag{2.64}$$

with:

$$F_n(t) = \frac{1}{x_{\max}} \int_{-x_{\max}}^{x_{\max}} f(x,t) \cos\left(\frac{n\pi x}{x_{\max}}\right) dx, \tag{2.65}$$

$$P_n(t) = \frac{1}{x_{\max}} \int_{-x_{\max}}^{x_{\max}} p(x,t) \cos\left(\frac{n\pi x}{x_{\max}}\right) dx. \tag{2.66}$$

From discretising (2.57) we have:

$$\begin{aligned} F_n(J) =& \frac{12}{35}\left(-\frac{(\delta t)^2 n\pi}{x_{\max}} P_n(J) + \frac{26}{3}F_n(J-\delta t) - \frac{19}{2}F_n(J-2\delta t)\right. \\ &\left. + \frac{14}{3}F_n(J-3\delta t) - \frac{11}{12}F_n(J-4\delta t)\right) \Big/ \left(1 + \sigma(\delta t)^2\left(\frac{n\pi}{x_{\max}}\right)^3\right). \end{aligned} \tag{2.67}$$

We use this equation to take an initial guess of the updated position of the free-surface Fourier coefficients then we calculated the free surface position using these coefficients and substitute this function into (2.62) to update the pressure. We then iterate until we reach convergence as in the previous

method. We take enough terms that the coefficients were very small for the higher order terms in the series. However, this time due to convergence being harder to achieve, we judge convergence of the solution to have occurred when the relative error is less 10^{-3}, and this happens in fewer than 40 iterations, enough terms are taken in the Fourier series to obtain good convergence: $N = 128$ terms were used for the computations. More terms would yield more accurate results for a much longer run time. Due to the predicted symmetry of the problem only Cosine terms were used in the series to reduce the computation time, upon introducing Sine terms the results were the same, this was verified by looking at the coefficients for the Sine term which were found to be of order 10^{-3}. For considering obliqueness and surface tension Sine terms would have to be considered too. Smaller time steps and grid sizes were tested and results did not change, for less computational time we used $\delta t = 10^{-3}$ and $\delta x = 0.016$. Increasing the boundaries of numerical range of x, had in insignificant influence on the results, so we used $x_{\max} = 32$ in all of the results.

The time, $t = 0$ corresponds to touchdown time in a vacuum. Figure 2.2(a) shows the free-surface and pressure for a droplet at instants before impact onto an impermeable horizontal plate with zero surface tension, and the droplet having zero horizontal motion. Touchdown is approached which does leave a trapped pocket of gas, which can be seen on the free surface plot. In a vacuum touchdown would occur at $t = 0$, however, due to air-cushioning the time to touchdown has been delayed to a non-dimensional time of approximately $t = 7$. This approximation of the touchdown time is obtained from Figure 2.2(b), which shows an almost steady rate of closure of the gap between the free-surface and the impermeable substrate. The results I obtained have good agreement with previous work done on these impacts. Hicks and Purvis (2010) were solving for the full three-dimensional case, however, from the two-dimensional plots in this study we can draw

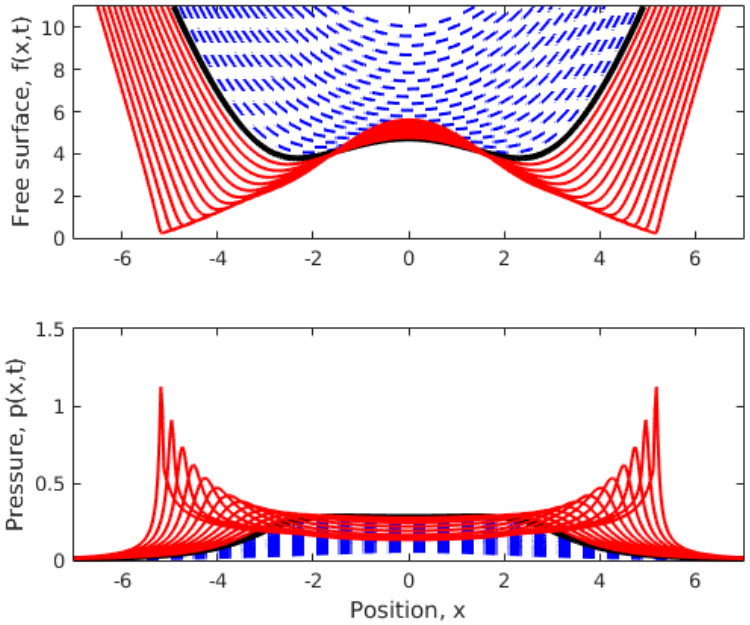

(a) Free-surface and pressures profiles

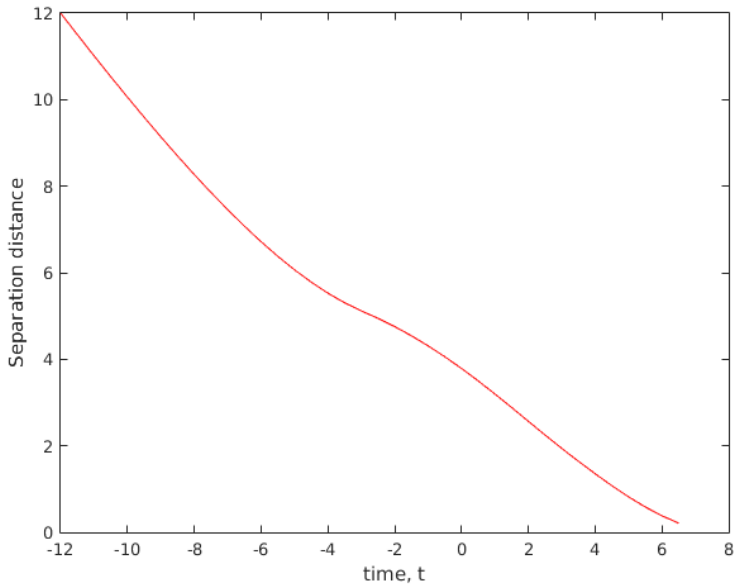

(b) Separation distance of the droplet to the flat plate

Figure 2.2: Blue lines correspond to times before $t = 0$, the black line corresponds to $t = 0$ and the red lines correspond to times after $t = 0$.

direct comparisons. The initial free-surface shape differs by a factor of 2 so accounting for this the bubble radii are both ~ 5.2 and ran until around $t = 6$. The results in this thesis were ran slightly longer which meant we could get closer to touchdown which will give rise to higher pressure peaks in these last time steps. We can compare the pressure in the centre of the droplet to be ~ 0.3 in both this thesis and Hicks and Purvis (2010). These sets of results agree well.

Impacts with surface tension

Figure 2.3 shows the changes in time of the free-surface and the pressure distribution for a very small value of σ. The profiles and the separation-distance plot are very similar to that of the case with zero surface tension. However, with surface tension the droplet doesn't seem to reach touchdown for all values of $\sigma > 0$. Increasing the surface tension yields profiles that differ from the case with zero surface tension. We can see that the pressure peaks are much smaller as well as the free-surface being more reluctant to touchdown. Comparing the separation distance plots, they are very similar to approximately $t = 0$ where for higher surface tension the free-surface spreads more horizontally which rapidly decreases the gradient on the separation distance plot.

Changing the surface tension changed the heights and widths of the trapped bubble of air. When increasing the surface tension, the volume of the trapped gas pocket (which is calculated by integrating the free-surface between the two minima) decreases. The volume for $\sigma = 0.05$ is almost half of that for $\sigma = 0.001$. Comparing the pocket radius (the distance between the centre of the droplet and the lowest point of the free-surface) we find this too decreases as σ increases. The results obtained here can be compared with Purvis and Smith (2004b) where surface tension was also considered. The results have good agreement. There is a factor of 2 different in the

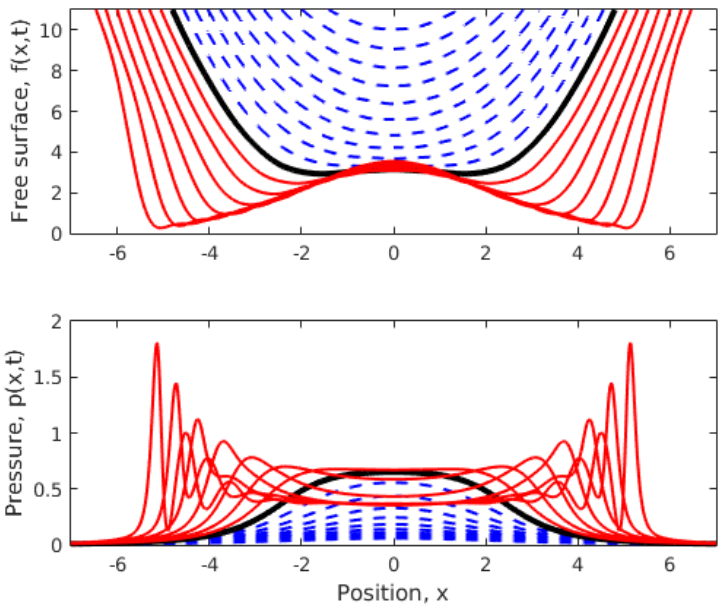

(a) Free-surface and pressures profiles for $\sigma = 0.001$

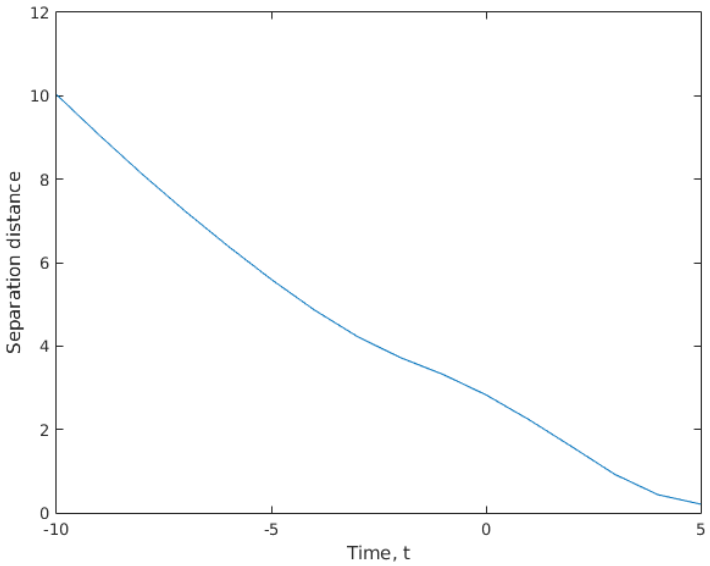

(b) Separation distance for $\sigma = 0.001$

Figure 2.3: The evolution of the droplet free-surface, gas film pressure distribution and separation distance for $\sigma = 0.001$.

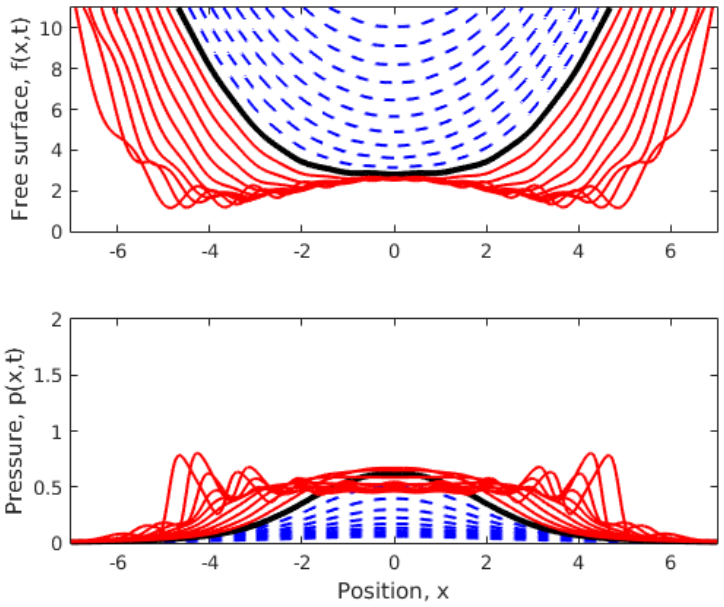

(a) Free-surface and pressures profiles for $\sigma = 0.5$

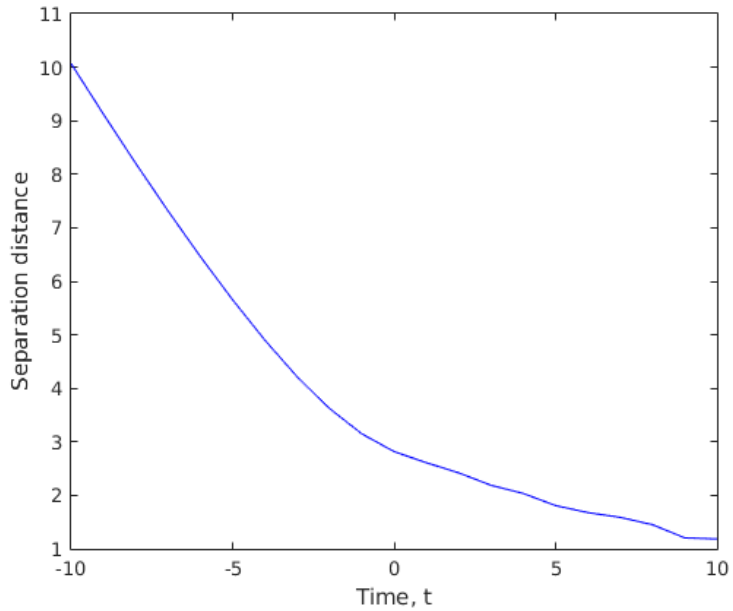

(b) Separation distance for $\sigma = 0.5$

Figure 2.4: The evolution of the droplet free-surface, gas film pressure distribution and separation distance for $\sigma = 0.5$.

initial free-surface shapes, with this taken into account we have comparable bubble radii of ~ 5 and run until approximately $t = 8$. Both sets of results exhibit waves on the freesurface, these are caused by the presence of surface tension and contribute to the delay of touchdown.

Impacts with obliqueness

We are now considering only oblique impacts (so $\sigma = 0$). Figures 2.5-2.7 shows the free-surface and pressure profiles for various values of c, the plate velocity. For small c the profiles are similar to that of when $c = 0$, but with the profile skewed in the direction of travel of the plate. Upon increasing c the free-surface profiles go from having two minima to only one, we change from having two local minima to one when c increases through the critical value $c_{crit} = 1.36$, to 3 significant digits, from the numerical results. Touchdown is achieved for all values of c, only positive values of c were considered, because negative values would simply produce a mirror image. Comparing the profiles for increasing values of c in Figure 2.8 we see that the pressure peak at the position of touchdown increases dramatically and the time to touchdown decreases as c increases. The separation distances reinforces this conclusion which results in curves becoming steeper as c increases. We can compare this situation to a slider bearing problem. The air close to the substrate is moving horizontally which in turn is moving the minimum of the free surface horizontally also which is being forced into the low pressure region, the droplet is still falling at a constant velocity this together allows for an acceleration into touchdown. There are no trapped bubbles of air for these cases, because there is only one touchdown position. The results shown here have good agreement to Hicks and Purvis (2010) where oblique impacts were covered, although this paper was about solving for the three-dimensional case, a cross-sectional result for oblique impacts was given and can be compared to the results we have shown here. Hicks and

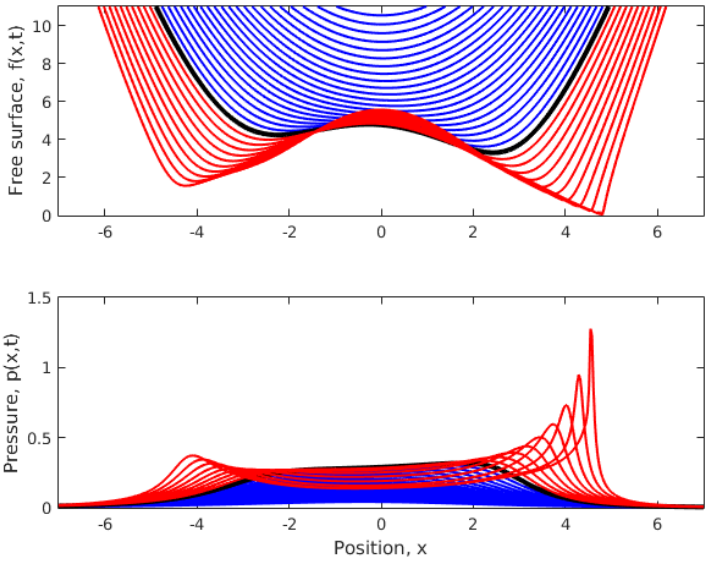

(a) Free-surface and pressures profiles for $c = 0.2$

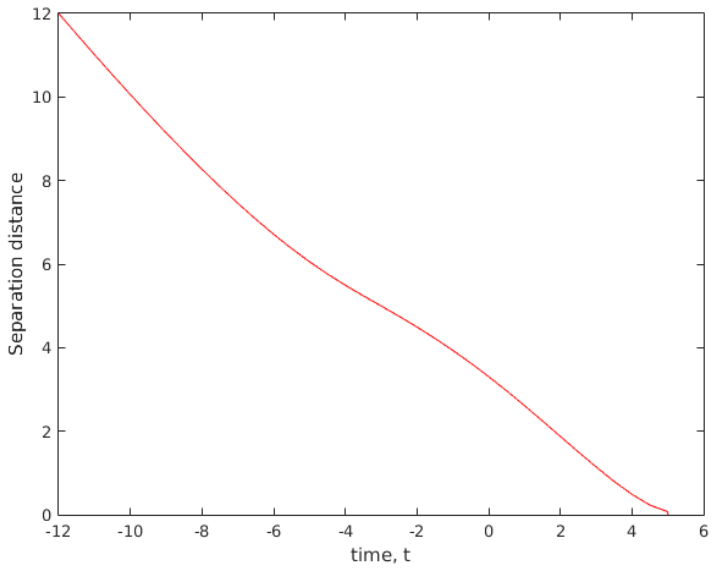

(b) Separation distance for $c = 0.2$

Figure 2.5: The evolution of the droplet free-surfaces, gas film pressures and separation distance for $c = 0.2$.

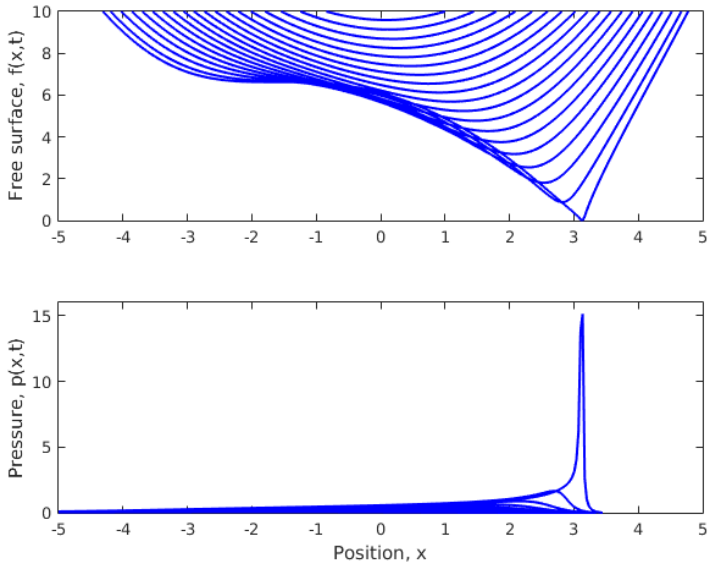

(a) Free-surface and pressures profiles for $c = 1.36$

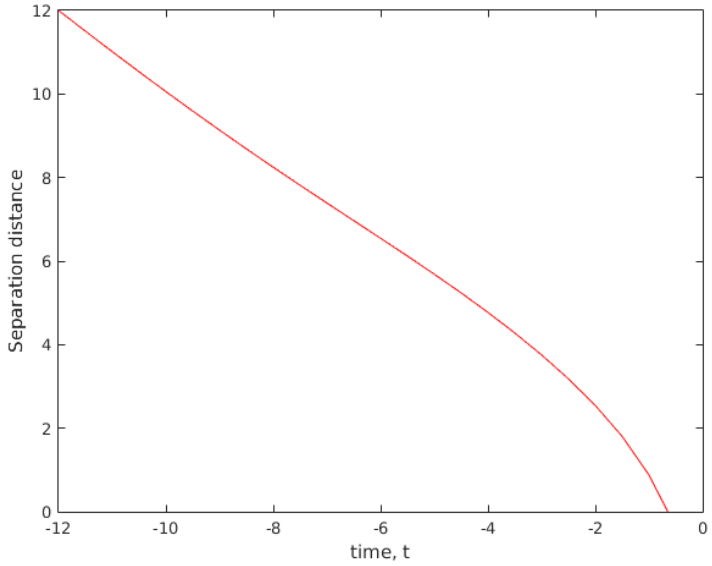

(b) Separation distance for $c = 1.36$

Figure 2.6: The evolution of the droplet free-surfaces, gas film pressures and separation distance for $c = 1.36$.

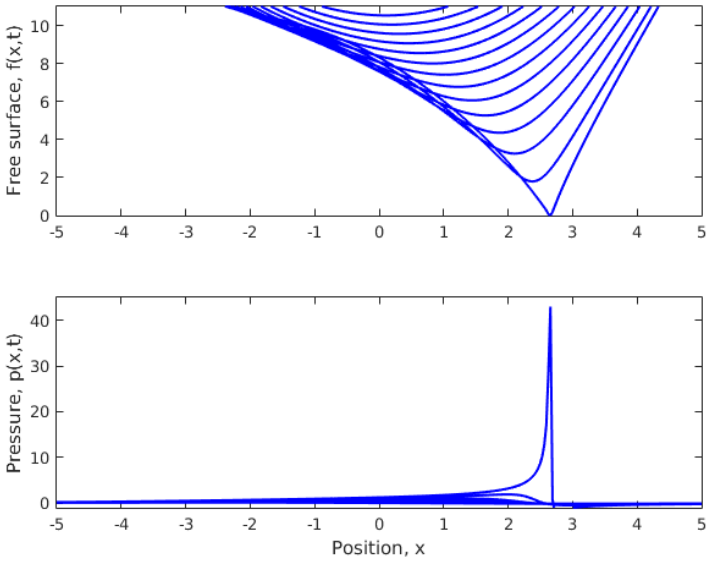

(a) Free-surface and pressures profiles for $c = 5$

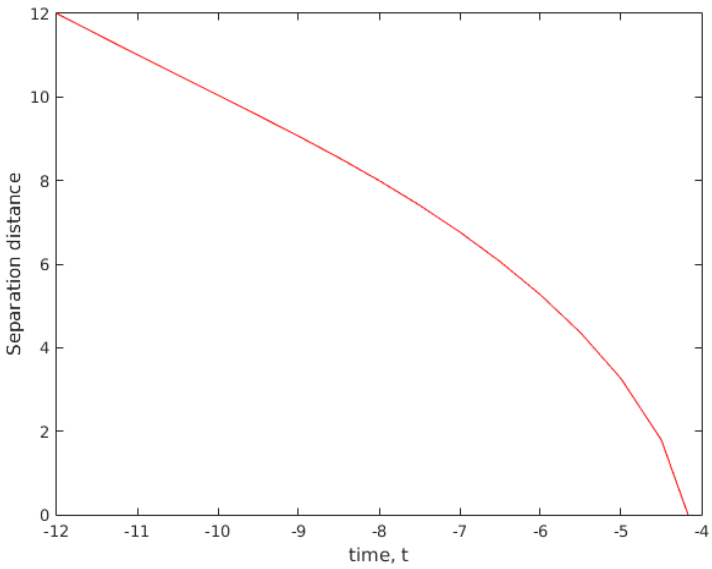

(b) Separation distance for $c = 5$

Figure 2.7: The evolution of the droplet free-surfaces, gas film pressures and separation distance for $c = 5$.

Purvis (2010) also shows there is a transition between having two minima on the free surface to only one with a large pressure peak at the location of the lowest point of the free surface. The difference between the sets of results is the direction of the moving substrate being in opposite directions.

As c increases the touchdown times are monotonically decreasing, running the numerics with $c = 50$ shows the touchdown time is still decreasing, there must be a limit on the time however, as all the numerics begin at $t = -12$. However, as c increases the touchdown position doesn't change as much as the touchdown time, from Figure 2.8(b), the touchdown position, and the position of the pressure peak, remain almost constant after $c = 5$ and only vary slightly. We conclude that the touchdown position remains constant, but the time to touchdown decreases when c is very large.

2.5 Conclusions

In this chapter we have derived and solved equations corresponding to a droplet impacting an impermeable substrate incorporating the addition of obliqueness and surface tension. Obliqueness had the effect of increasing acceleration into touchdown allowing for faster touchdown times, whereas the addition of surface tension had the opposite effect. This chapter is an important first step towards the material in the next chapter that includes shallow water layers.

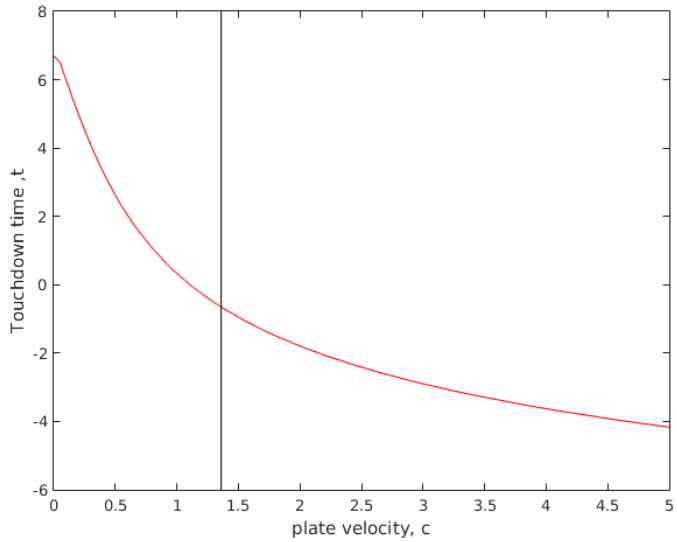

(a) Touchdown times as a function of c

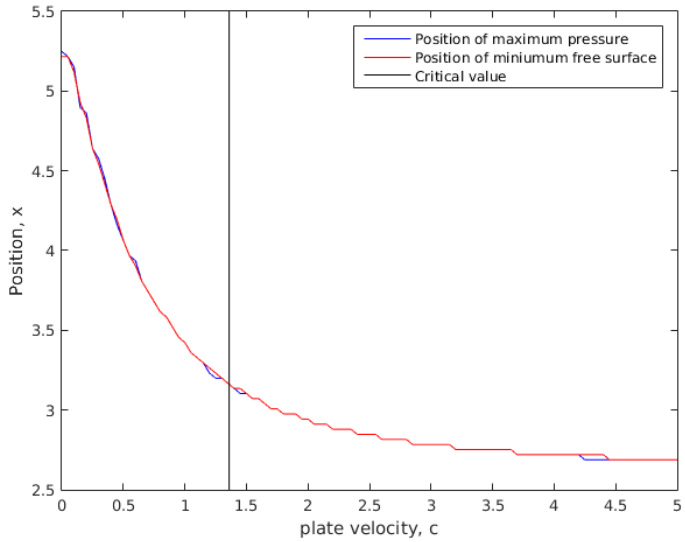

(b) Positions of the pressure peaks and the minimum free surface at touchdown as functions of c

Figure 2.8: The touchdown time, the position of the pressure peak and the free-surface minimum, plotted as c varies (increments of c being 0.1.) The vertical line marks the critical value of c.

3

Cushioning of a shallow water layer impact onto an impermeable substrate

3.1 Introduction

In this chapter we consider the problem of a shallow-water layer covering a rigid body impacting with an impermeable base. This work follows closely that done in Korobkin et al. (2008), however, here we are just considering the case with a single water layer which is covering the surface of a rigid body. We will consider obliqueness which is a new addition to this model.

3.2 Non-dimensionalisation

Consider a rigid circular body falling towards a rigid horizontal plate. This body has radius, R, is falling with velocity U (vertically downwards) and $\epsilon \ll 1$ which is the scale for the spatial coordinates as used in the previous chapter. There is a thin water layer coating the rigid body which has dimensional depth $h^* = \alpha h$ with $\alpha = O(1)$ and $h \ll 1$. If we have $h \gg \epsilon$ then we will have the previous case covered in Chapter 2. If we have $h \ll \epsilon$, for a very thin film to leading order it is a standard squeeze film problem, with the water layer having no effect to leading order. Therefore we are going to consider the case where h and ϵ are comparable.

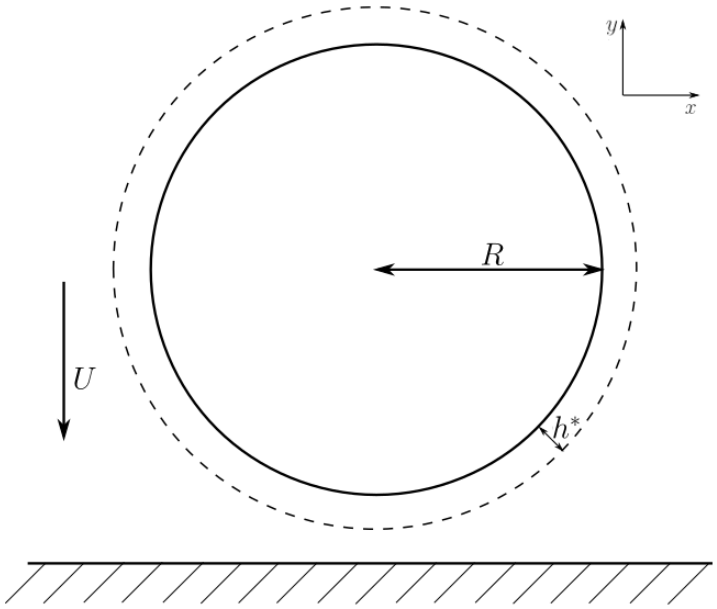

Figure 3.1: Diagram showing the scales used in the derivation for the coupled equations

The scales for the water layer follow from the same reasoning as in Section 2.2, but with an alteration for the time scale changing to the time for the droplet to fall through the non-dimensional thickness of the air layer (ϵ^2) with approach velocity being $O(1)$ as it has been scaled out in Section 2.1.1. Scales for the air layer follow similar reasoning to Section 2.3, with the differences being the thickness of the air layer and hence the scaling for the y coordinate and the horizontal velocity component now have dependence on the non-dimensional thickness of the water layer. As the thickness in the water layer and the air layer are comparable close to impact, we begin having already scaled out U and R:

$$(u_w^*, v_w^*, p_w^*, x^*, y^*, t^*) = \left(u_w, v_w, \mathcal{P}_w p_w, \epsilon x, \epsilon y, \epsilon^2 t\right), \tag{3.1}$$

$$(u_a^*, v_a^*, p_a^*, x^*, y^*, t^*) = \left(\epsilon^{-1} u_a, v_a, \mathcal{P}_a p_a, \epsilon x, \epsilon^2 y, \epsilon^2 t\right), \tag{3.2}$$

where $\mathcal{P}_w$ and $\mathcal{P}_a$ are unknown dimensionless constants.

3.3 Equation modelling shallow water flow

We start from equation (2.7) applying scales in (3.1), we obtain for the water flow:

$$\epsilon^{-2}\mathbf{u}_{w_t} + \epsilon^{-1}\left(\mathbf{u}_w \cdot \nabla\right)\mathbf{u}_w = -\mathcal{P}_w\epsilon^{-1}\nabla p_w + Re^{-1}\epsilon^{-2}\nabla^2\mathbf{u}_w, \tag{3.3}$$

$$\left(\nabla \cdot \mathbf{u}_w\right) = 0, \tag{3.4}$$

where $Re = \frac{\rho_w UR}{\mu_w}$ is the water Reynolds number as defined in Section 2.1.1. Rearranging (3.3) and (3.4) we obtain:

$$\mathbf{u}_{w_t} + \epsilon\left(\mathbf{u}_w \cdot \nabla\right)\mathbf{u}_w = -\epsilon\mathcal{P}_w\nabla p_w + Re^{-1}\nabla^2\mathbf{u}_w, \tag{3.5}$$

$$\nabla \cdot \mathbf{u}_w = 0. \tag{3.6}$$

Using our assumption that h and ϵ are comparable close to impact, in order to keep pressure at leading order we must have balance between the pressure term and $\mathbf{u}_{w_t}$. This requires us to define the pressure scale $\mathcal{P}_w = \epsilon^{-1}$. Taking the leading order terms (neglecting the viscous forcing terms by imposing the same condition on the water Reynolds number as in Section 2.2), (3.6) remains unchanged and (3.5) becomes:

$$\mathbf{u}_{w_t} = -\nabla p_w, \tag{3.7}$$

which is valid in the upper half plane, and we obtain the shallow water equations. We have the usual conditions on the free-surface for this flow, namely the kinematic condition, (2.22), and the normal stress condition, (2.24). The kinematic condition is:

$$v_w^* = F_{t^*}^* + u_w^* F_{x^*}^* \qquad \text{on} \qquad y^* = F^*, \tag{3.8}$$

where $y^* = F^*$ is the free surface of the shallow water layer. We need to apply another scale for the shallow water layer. We now re-scale the y^* coordinate now as $y^* = \epsilon\bar{y}(= \epsilon^2 y)$ to account for a shallow water layer and the disparate length scale. Applying this to the vertical component of (3.7)

simply becomes $p_{w_{\bar{y}}} = 0$, hence $p_w = p_w(x,t)$. Integrating the continuity equation (2.13) with respect to y^* across the shallow water layer (applying the kinematic boundary condition and a no-slip condition on the wall of the body), noting that u_w^* is independent of y^*, we obtain:

$$[v_w^*]_S^{F^*} = \alpha u^*_{w_{x^*}}, \tag{3.9}$$

where α is the average depth of the water layer and $y = S$ is the surface of the solid body, at which we have a no-slip condition. Substituting in the kinematic condition (3.8) and rearranging we have:

$$F^*_{t^*} - U = \alpha u^*_{w_{x^*}} - u^*_w F^*_{x^*}. \tag{3.10}$$

Applying the scales (3.1) we obtain:

$$\frac{1}{\epsilon} F_t - U = \frac{1}{\epsilon} \alpha u_{w_x} - \frac{\epsilon}{\epsilon} u_w F_x. \tag{3.11}$$

If we are close to impact then $h = O(\epsilon)$. At leading order, we have:

$$F_t = \alpha u_{w_x}. \tag{3.12}$$

We differentiate (3.12) with respect to t and substitute the horizontal component of (3.7) to obtain:

$$F_{tt} = -\alpha p_{w_{xx}}. \tag{3.13}$$

This differs to (2.27) for the deep-water droplet; this is a local relationship between the free-surface and the pressure, the other case gives a global relationship between them.

3.4 Equations for the air

Components of equation (2.8) for the air are scaled using (3.2). This derivation proceeds in a similar way as for deep water in Section 2.3 but with different scales. After substitution into equations (2.8) and (2.9) we obtain:

$$\frac{1}{\epsilon^3}u_{a_t} + \frac{1}{\epsilon^2}\left(u_a u_{a_x} + v_a u_{a_y}\right) = -\frac{\mathcal{P}_a \rho_w}{\rho_a \epsilon} p_{a_x} + \frac{\nu_a}{\nu_w \epsilon^3 Re}\left(u_{a_{xx}} + \frac{1}{\epsilon^2}u_{a_{yy}}\right), \tag{3.14}$$

$$\frac{1}{\epsilon^2}v_{a_t} + \frac{1}{\epsilon^2}\left(u_a v_{a_x} + v_a v_{a_y}\right) = -\frac{\mathcal{P}_a \rho_w}{\rho_a \epsilon^2} p_{a_y} + \frac{\nu_a}{\nu_w \epsilon^2 Re}\left(v_{a_{xx}} + \frac{1}{\epsilon^2}v_{a_{yy}}\right), \tag{3.15}$$

$$\frac{1}{\epsilon^2}u_{a_x} + \frac{1}{\epsilon^2}v_{a_y} = 0. \tag{3.16}$$

After rearrangement we have:

$$\begin{aligned}\frac{\epsilon^2 \nu_w Re}{\nu_a}u_{a_t} + &\frac{\epsilon^2 \nu_w Re}{\nu_a}\left(u_a u_{a_x} + v_a u_{a_y}\right) \\ &= -\frac{\mathcal{P}_a \epsilon^4 \nu_w Re \rho_w}{\rho_a \nu_a} p_{a_x} + \left(\epsilon^2 u_{a_{xx}} + u_{a_{yy}}\right), \end{aligned} \tag{3.17}$$

$$\begin{aligned}\frac{\rho_a}{\rho_w}v_{a_t} + &\frac{\rho_a}{\rho_w}\left(u_a v_{a_x} + v_a v_{a_y}\right) \\ &= -\mathcal{P}_a p_{a_y} + \frac{\nu_a \rho_a}{\rho_w \nu_w Re}\left(v_{a_{xx}} + \frac{1}{\epsilon^2}u_{v_{yy}}\right), \end{aligned} \tag{3.18}$$

$$u_{a_x} + v_{a_y} = 0. \tag{3.19}$$

From equation (3.17) in order to include the pressure gradient at leading order we must have $\frac{\mathcal{P}_a \epsilon^4 \nu_w Re \rho_w}{\rho_a \nu_a} = 1$, so that using the definition for ϵ (equation (2.35), we must have $\mathcal{P}_a = O(\epsilon^{-1})$. We need the pressures of the air and water to match, so we have:

$$\mathcal{P}_w = \mathcal{P}_a = \frac{U^2 \rho_w}{\epsilon}. \tag{3.20}$$

We now take the leading order of equations (3.17)-(3.19), and we have:

$$0 = -p_{a_x} + u_{a_{yy}}, \tag{3.21}$$

$$-p_{a_y} = 0, \tag{3.22}$$

$$u_{a_x} + v_{a_y} = 0. \tag{3.23}$$

These are the same lubrication equations derived in Section 2.3 with the same conditions, so the derivation to obtain the relation between the pressure and free-surface is exactly the same. In summary, the coupled equations

for the impact for shallow water are, from (2.51) and (3.13):

$$F_t = \frac{1}{12}\left(p_{a_x}F^3\right)_x, \tag{3.24}$$

$$F_{tt} = -\alpha p_{w_{xx}}. \tag{3.25}$$

The parameter α can be removed by altering the scalings. This makes the coefficient in (3.25), unity. We do this with:

$$x = \alpha^{\frac{1}{4}}\bar{x},$$
$$t = \alpha^{\frac{1}{2}}\bar{t},$$
$$F = \alpha^{\frac{1}{2}}\bar{F},$$
$$p = \alpha^{-1}\bar{p},$$

where barred quantities are non-dimensional. The simplified non-dimensional problem is then parameter-free (after dropping the bars):

$$F_t = \frac{1}{12}\left(p_x F^3\right)_x, \tag{3.26}$$

$$F_{tt} = -p_{xx}, \tag{3.27}$$

with incident free-surface shape of:

$$F(x,t) \to \frac{x^2}{2} - t \qquad \text{as } t \to -\infty \text{ and as } x \to \pm\infty, \tag{3.28}$$

and $p(x,t) \to 0$ as $x \to \pm\infty$.

3.4.1 Additions to the model

The additions to this model are identical to the previous chapter, and are derived in the same way as the deep-water case, see Section 2.3.1 for the derivation. So for oblique impacts we will have (3.26) replaced with:

$$F_t = \frac{1}{12}\left(P_{a_x}F^3\right)_x - cF_x. \tag{3.29}$$

We obtain this equation by the same method as in Section 2.2.3, our boundary condition is that the substrate is no longer stationary and instead moves with a constant horizontal velocity. Here c is the horizontal velocity of the plate similarly to the previous case $c^* = O(\epsilon^{-1})$.

We can also give the equations for the addition of surface tension. We substitute (2.23) into (3.25) so we have:

$$F_{tt} = -\alpha \left(p_{a_{xx}} + \sigma F_{xxxx} \right). \tag{3.30}$$

3.5 Computational results and discussion

The method for solving these coupled equations numerically is exactly the same as the method used in Chapter 2, with, however, (3.27) being discretized as follows:

$$\begin{aligned} F(I,J) =& \frac{12}{35}\left(\frac{26}{3}F(I,J-\delta t) - \frac{19}{2}F(I,J-2\delta t) + \frac{14}{3}F(I,J-3\delta t) \right. \\ & - \frac{11}{12}F(I,J-4\delta t) + \frac{(\delta t)^2}{(\delta x)^2}\left(-\frac{1}{12}P(I-2\delta x,J) \right. \\ & \left. \left. + \frac{4}{3}P(I-\delta x,J) - \frac{5}{2}P(I,J) + \frac{4}{3}P(I+\delta x,J) - \frac{1}{12}P(I+2\delta x,J) \right) \right). \end{aligned} \tag{3.31}$$

The grid sizes and time steps used are $\delta x = 0.016$ and $\delta t = 10^{-3}$ respectively. In the same way we use the pressure from the previous time step to update the free-surface (3.31) and then we use this to update pressure using (2.62). In this case we do not have a Hilbert transform in the governing equation so everything can be solved by discretisation. Typically this method used fewer iterations per time step, compared to solving with the Hilbert Transform, to achieve convergence, which is when we have a relative error less than 10^{-4} after substituting the updated free surface and pressure into (2.62).

Figure 3.2(a) shows free-surface and pressure evolutions for a shallow-water layer impacting an impermeable plate with zero surface tension and

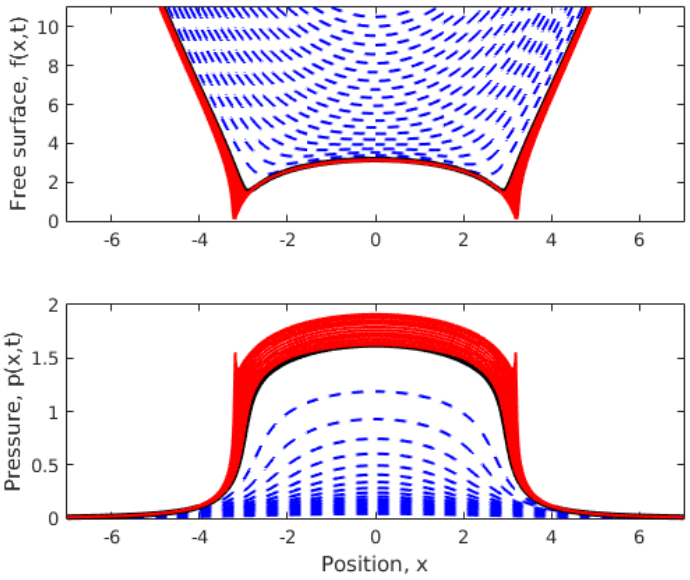

(a) Free-surface and pressures profiles with $\Delta t = 0.5$ before $t = 0$ and $\Delta t = 0.25$ after $t = 0$.

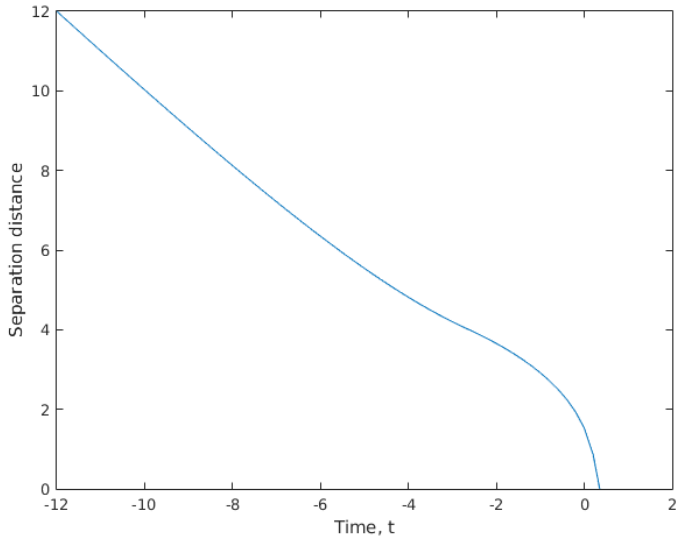

(b) Separation distance from the droplet interface to the flat plate.

Figure 3.2: Free-surface and pressure profiles for shallow-water layer impact with a horizontal impermeable plate and the separation distance as a function of time.

having zero horizontal velocity. Touchdown does occur and, similar to the deep water case, we have a trapped pocket of air. Touchdown is delayed due to air cushioning however, it is not delayed as much as for deep water, with touchdown here being approximately $t = 0.3$. Figure 3.2(b) shows the separation distance to the plate, which shows a high gradient towards the end of the motion showing the touchdown happens rapidly when the droplet is close to the plate, we have a rapid acceleration into touchdown. In contrast to the deep water case, we can see a higher mean in the pressure distribution within the air pocket with only small cusps forming close to the touchdown position. These peaks are lower than for deep water. The cusp behaviour seen in the pressure happens over a very small time period and only begins to form over the last of the time steps before touchdown. These results can be compared with Korobkin et al. (2008), we have good agreement between the two sets of results, the cusp behaviour in the pressure also matches well.

3.5.1 Shallow water with oblique impacts

This is a topic which has not been studied before in this detail. We obtained some interesting differences between studying both types of oblique droplet impacts. Figures 3.3-3.5 shows the free-surface and pressure profiles for various values of c, the plate velocity. For small c the profiles are similar to that of when $c = 0$. Increasing c we go from two free-surface minima to one minimum with the critical value for shallow water being $c \approx 0.68$ which is close to half what we found in the previous chapter. Touchdown is achieved for all non-zero values of c. Looking at the separation distance plots, we can see that the larger the value of c, the quicker touchdown happens and the steeper the curve. Similar to deep water, we lose the presence of a trapped pocket of air, due to there being only one touchdown position. The cusps in the pressure do not appear to happen when obliqueness is included. We have accelerated touchdown due to the squeeze film becoming a slide bearing

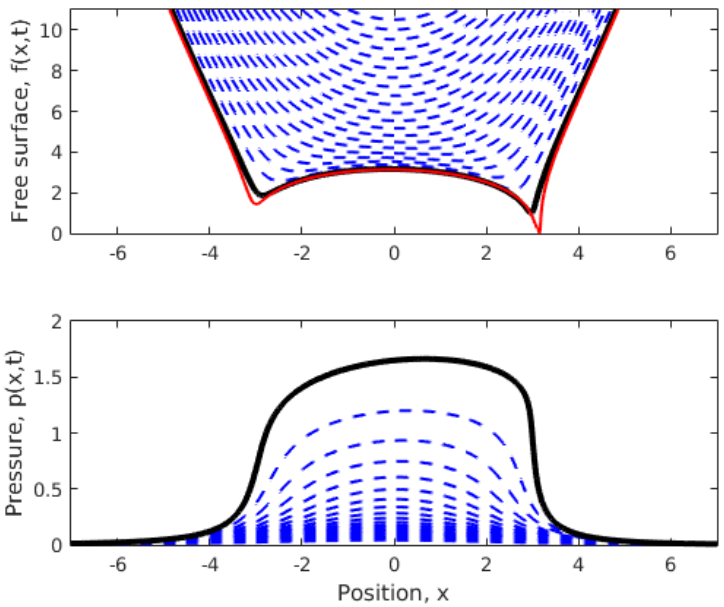

(a) Free-surface and pressures profiles for $c = 0.1$

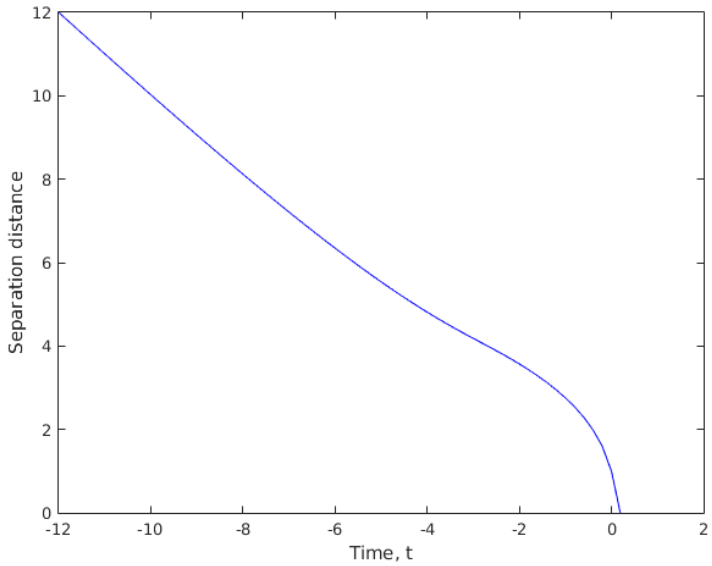

(b) Separation distance for $c = 0.1$

Figure 3.3: The evolution of the droplet free-surfaces, gas film pressures and separation distance for $c = 0.1$.

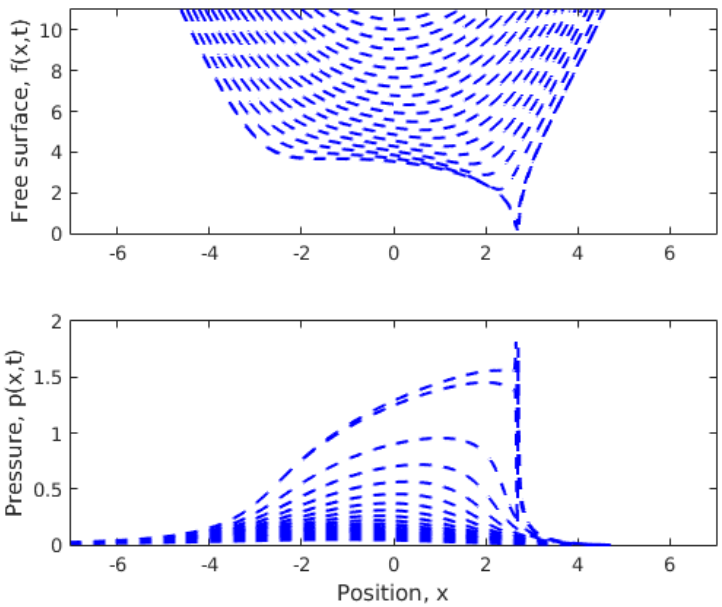

(a) Free-surface and pressures profiles for $c = 0.68$

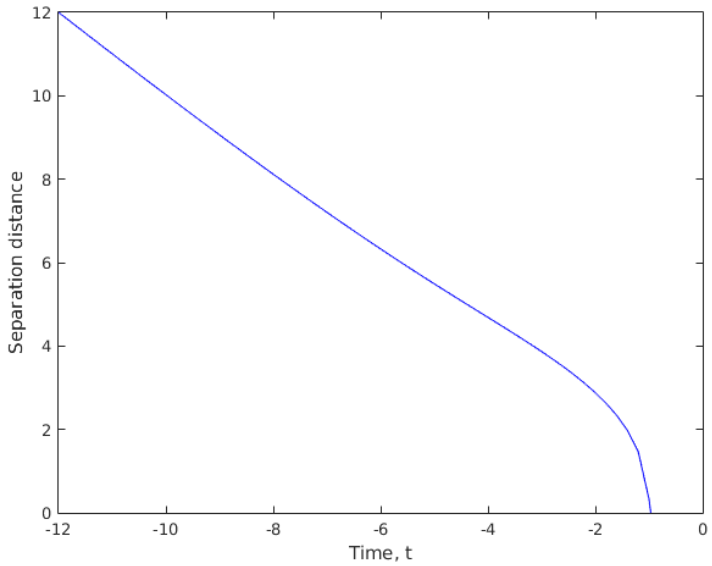

(b) Separation distance for $c = 0.68$

Figure 3.4: The evolution of the droplet free-surfaces, gas film pressures and separation distance for $c = 0.68$.

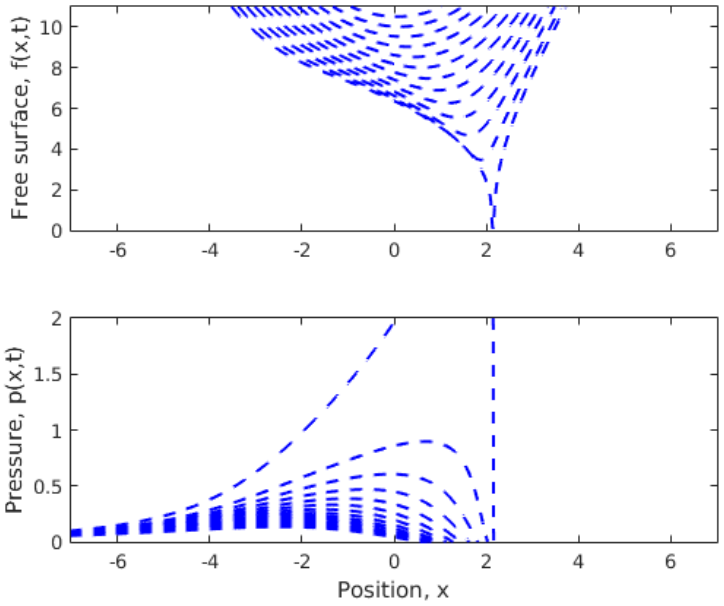

(a) Free-surface and pressures profiles for $c = 5$

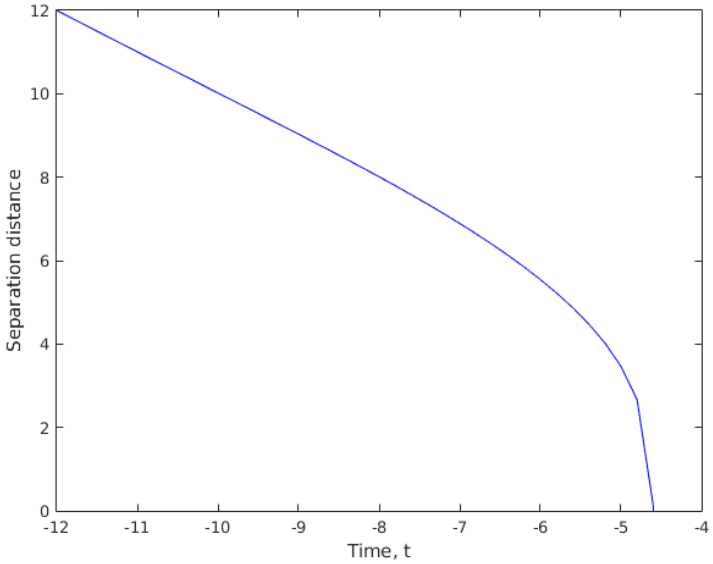

(b) Separation distance for $c = 5$

Figure 3.5: The evolution of the droplet free-surfaces, gas film pressures and separation distance for $c = 5$.

problem. We now get a high pressure on one side of the air layer which will accelerate that side into touchdown much faster than the other side. This acceleration into touchdown doesn't provide the time for the cusps to form which only appear to form moments before touchdown in the pressure.

As c increases the touchdown time monotonically decreases (just like for the deep water case). However, as c increases the touchdown position does not change as much as the touchdown time, from Figure 3.6(b), the touchdown position (and position of the pressure peak) remains close to being constant for $c > 5$ and only slightly increases. We conclude that the touchdown position remains close to constant, but the time to touchdown decreases as c is made very large.

3.6 Conclusions

In this chapter we have derived and solved the situation of a shallow-water layer covering a solid body impacting with an impermeable substrate. A system of equations was derived including a new addition of a term corresponding to obliqueness. For small and increasing values of c, the minimum point of the free surface changes its behaviour during approach to impact. As c increase the free surface is accelerated downwards by the air flow. With the obliqueness included, the cusp behaviour in the pressure very close to touchdown is not observed in our results.

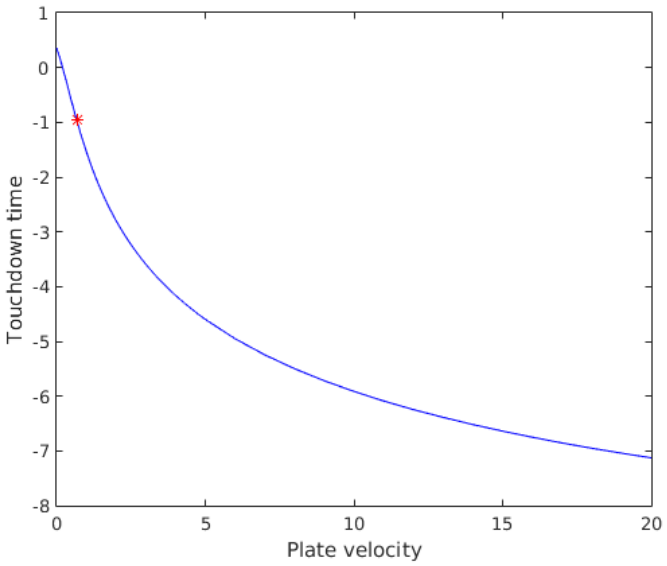

(a) Touchdown times as a function of c, the star indicates the value for c for which we go from two minima to one.

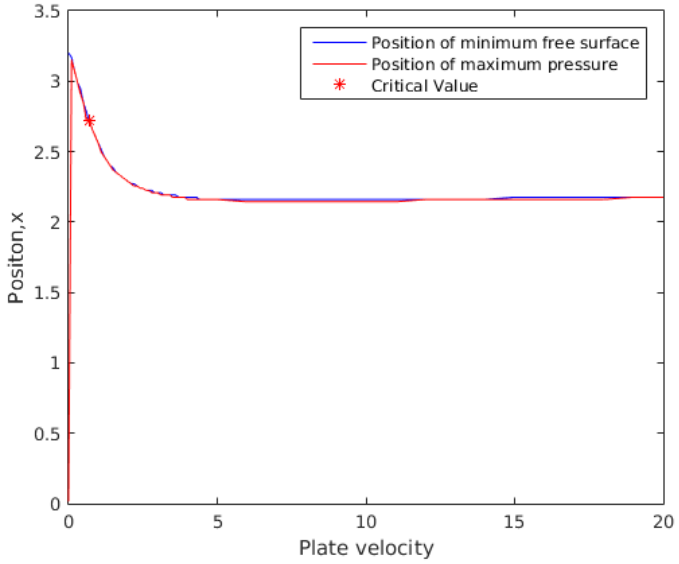

(b) Positions of pressure peak and free-surface minimum at touchdown: c-dependence

Figure 3.6: The touchdown times and the position of the pressure peaks and the minimum free-surface plotted as the plate velocity c varies (increments of c being 0.1.) The star marks the critical value of $c = 0.68$.

4

Shallow water layer impact onto a shallow porous substrate

4.1 Introduction

In comparison to impacts onto impermeable substrates, impacts onto porous substrates haven't been considered very much. Hicks and Purvis (2015) have considered a deep water impact onto textured surfaces and shallow layers of porous media. Deeper layers of porous media have not been considered. There are important applications to understanding the mechanism of an impact with porous media such as hazardous materials in porous media, a problem posed in Parker and Nally (2012). To extend the problem considered in the previous chapter we will derive a new system to describe the impact of a shallow-water layer onto a porous substrate, the substrate allowing air to flow into and out of it. Examples for this situation can be ice particles with thin layers of water coating it or dry paint with a thin layer of wet paint coating it impacting such surfaces such as paper, wood, concrete and tarmac. We will first non-dimenionalise the governing equations with suitable scales considering a thin porous layer. We will use the Darcy equations to model the velocities in the substrate to couple the flow within the substrate with the air and water equations to close the problem. This will then be solved numerically. Since we are considering a shallow water layer impacting onto a porous substrate, the analysis would be very similar

to consider a porous solid impacting a water layer, the differences would be in the boundary and far field conditions.

4.2 Derivation of coupled equations

Consider a rigid circular body falling towards a thin layer of porous media. This body has radius, R, is falling with velocity U (vertically downwards) and $\epsilon \ll 1$ which is the scale for the spatial coordinates as used in the previous chapter. There is a thin water layer coating the rigid body which has dimensional depth $h^* = \alpha h$ with $\alpha = O(1)$, with the same justifications as the previous chapter we are considering the case when h is comparable to ϵ. The porous layer has constant isotropic porosity K and depth H. With the addition of porosity to this model we expect that we will have air driven into the substrate which will give us overall lower air pressures since the air can be displaced into the substrate rather than just to the sides. The lower pressures should also reduce the delay before touchdown.

The scalings for the air and water layers are the same as in Chapter 3, however, due to changes at $y = 0$ we no longer have an impermeable substrate. We will need to model the porous substrate to find what effects it has on the air layer. The air layer will describe what happens to the deformation of the droplet. For the water and air layers we have:

$$(u_w^*, v_w^*, p_w^*, x^*, y^*, t^*) = \left(u_w, v_w, \epsilon^{-1} p_w, \epsilon x, \epsilon y, \epsilon^2 t\right), \tag{4.1}$$

$$(u_a^*, v_a^*, p_a^*, x^*, y^*, t^*) = \left(\epsilon^{-1} u_a, v_a, \epsilon^{-1} p_a, \epsilon x, \epsilon^2 y, \epsilon^2 t\right). \tag{4.2}$$

We assumed the porous medium to be isotropic and that the flow is Darcy flow. From De Wiest (1969) we have the Darcy velocity components in the horizontal and vertical directions in the medium given by (here we

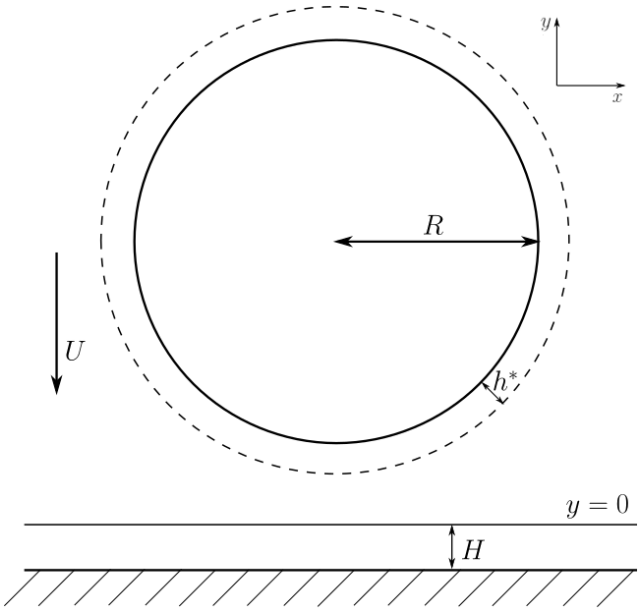

Figure 4.1: Diagram showing the scales used in the derivation for the coupled equations

will use s to indicate substrate variables):

$$u_s^* = -\frac{K}{\mu_a}\frac{\partial p^*}{\partial x^*}, \tag{4.3}$$

$$v_s^* = -\frac{K}{\mu_a}\frac{\partial p^*}{\partial y^*}, \tag{4.4}$$

where K is the dimensional permeability of the medium. We also have boundary conditions at the interface between the medium and the air layer above it (at $y = 0$ in our problem), from Beavers and Joseph (1967) we have:

$$\frac{K^{\frac{1}{2}}}{\gamma}\frac{\partial u_a^*}{\partial y^*} = u_a^* - \delta u_s^*, \tag{4.5}$$

where γ is the Beavers-Joseph coefficient which depends on the medium's pore size and material properties. The parameter $\delta = 1$ corresponds to slip, and $\delta = 0$ corresponds to no slip on the substrate-air interface. Saffman (1971) concluded that $u_s^* = O(K)$, so for small K this term is negligible and you can assume a no-slip condition, here we are considering $K = O(1)$ so

we will proceed with the full condition. We have from Beavers and Joseph (1967) that:

$$v_a = v_s \qquad \text{on } y = 0. \tag{4.6}$$

We also require a balance of the normal component of stress on the surface of the substrate:

$$p_s^*(x^*, 0, t^*) = p_a^*(x^*, t^*). \tag{4.7}$$

We also have the conservation of mass equation for the substrate given by:

$$\frac{\partial u_s}{\partial x} + \frac{\partial v_s}{\partial y} = 0. \tag{4.8}$$

We are going to consider a thin porous layer here, where we have disparate length scales (having a smaller y scale gives us a thin porous layer). If we have comparable x and y scales we will have the intermediate case where we will have to solve Laplace's equation in the substrate to get the condition on $y = 0$. Finally if we have a much larger y scale we will have the deep porous layer case where the influence of the bottom of the substrate on the flow is negligible. We will require the following scalings for the air flow within the thin porous substrate:

$$\begin{aligned}(u_s^*, v_s^*, p_s^*,\ & x^*, y^*, t^*, H^*) \\ &= \left(\epsilon^{-1}U u_s, U v_s, \epsilon^{-1}U^2\rho_w p_s, \epsilon R x, \epsilon^2 R y, \epsilon^2 \frac{R}{U} t, \epsilon^2 R H\right),\end{aligned} \tag{4.9}$$

where H is the substrate height (the substrate occupies the region: $-H \leq y \leq 0$).

The equation for the water layer is derived in exactly the same way as in Section 3.3 and so we adopt equation (3.27). The equation modelling the gas flow in the air layer follows a different derivation to that in Section 3.4, however, the start of the derivation is the same. To avoid repetition we will

use equations (3.21)-(3.23) in this derivation. So we have:

$$0 = -p_{a_x} + u_{a_{yy}}, \tag{4.10}$$

$$-p_{a_y} = 0, \tag{4.11}$$

$$u_{a_x} + v_{a_y} = 0. \tag{4.12}$$

To begin the derivation of the influence of the porous layer in the solution we substitute the scales in (4.9) into the conservation of mass equation (4.8), and we obtain:

$$\epsilon^{-2}\frac{\partial u_s}{\partial x} + \epsilon^{-2}\frac{\partial v_s}{\partial y} = 0, \tag{4.13}$$

$$\frac{\partial u_s}{\partial x} + \frac{\partial v_s}{\partial y} = 0. \tag{4.14}$$

Upon substitution of the scalings into equations (4.3) and (4.4) we have the Darcy velocity components now as:

$$u_s = -\frac{\rho_w U K}{\epsilon R \mu_a}\frac{\partial p_s}{\partial x}, \tag{4.15}$$

$$v_s = -\frac{\rho_w U K}{\epsilon^3 R \mu_a}\frac{\partial p_s}{\partial y}. \tag{4.16}$$

It is worth noting that the limit of $K \to 0$ is an impermeable substrate, and we exactly recover the problem covered in Chapter 3.

We define the effective permeability, k, to remove the scales from the Darcy velocity components:

$$k = \frac{\rho_w U K}{\epsilon R \mu_a}, \tag{4.17}$$

for a water layer of radius $1 - 10$mm with impact speed of $1 - 10\text{ms}^{-1}$ and actual substrate permeability of $K = 5\mu\text{m}^2$ we have $k \approx 0.4 - 198$, with our focus on values of $k \sim 1$, thus we have Darcy velocities now as:

$$u_s = -k\frac{\partial p_s}{\partial x}, \tag{4.18}$$

$$v_s = -\frac{k}{\epsilon^2}\frac{\partial p_s}{\partial y}. \tag{4.19}$$

At the interface between the air layer and the porous media, the scaled Beavers-Joseph condition (from equation (4.5)) after rearrangement gives:

$$\frac{k^{\frac{1}{2}}}{\gamma}\frac{\partial u_a}{\partial y} = u_a - \delta u_s, \tag{4.20}$$

From substitution of (4.18) and (4.19) into (4.14) we find a PDE for $p_s(x, y, t)$:

$$\frac{\partial^2 p_s}{\partial x^2} + \frac{1}{\epsilon^2}\frac{\partial^2 p_s}{\partial y^2} = 0, \tag{4.21}$$

which is valid in the substrate. At the bottom of the porous layer $v_s = 0$, therefore $\frac{dp_s}{dy} = 0$ is a boundary condition.

Motivated by the disparate scales in (4.21), and the following approach of Knox et al. (2015), we solve for the pressure in the substrate by expanding the pressure in the form as follows:

$$p_s(x, y, t) = p_a(x, t) + \epsilon^2 P_s(x, y, t). \tag{4.22}$$

The form of (4.22) is to ensure that the leading order pressure term matches the air layer, we want this so the normal stresses balance (equation (4.7)) and we have a small correction term. Substituting (4.22) into (4.21) we obtain:

$$\frac{\partial^2 p_a}{\partial x^2} + \epsilon^2\frac{\partial^2 P_s}{\partial x^2} + \frac{\partial^2 P_s}{\partial y^2} = 0, \tag{4.23}$$

at leading order we have:

$$\frac{\partial^2 p_a}{\partial x^2} + \frac{\partial^2 P_s}{\partial y^2} = 0. \tag{4.24}$$

Upon integrating (4.24) with respect to y, and noting that at $y = -H$ (the impermeable lower boundary of the porous layer) we have a zero-penetration condition. So from (4.19):

$$\frac{\partial P_s}{\partial y} = -\frac{v_s}{k} = 0 \qquad \text{on } y = -H, \tag{4.25}$$

thus (4.24) becomes:

$$\frac{\partial P_s}{\partial y} = -(y + H)\frac{\partial^2 p_a}{\partial x^2}. \tag{4.26}$$

Using this we can re-write the Darcy velocity components at the top of the porous layer in terms of the air layer pressure, p_a, so at leading order we have:

$$u_s(x,0,t) = -k\frac{\partial p_a}{\partial x}, \tag{4.27}$$

$$v_s(x,0,t) = kH\frac{\partial^2 p_a}{\partial x^2}, \tag{4.28}$$

which are valid at $y = 0$. To couple the flows in the air layer and the substrate, we proceed in a similar way to Section 3.4. We integrate:

$$0 = -p_{a_x} + u_{a_{yy}}, \tag{4.29}$$

in the air layer with respect to y twice and apply condition (4.20) and the kinematic condition on the free surface of the droplet (2.42), we have:

$$u_a = \frac{(y-F)\left(\left(\gamma F + k^{\frac{1}{2}}\right)y + k^{\frac{1}{2}}F + 2k\gamma\delta\right)}{2\left(\gamma F + k^{\frac{1}{2}}\right)}\frac{\partial p_a}{\partial x}. \tag{4.30}$$

Using (3.23) we can find an expression for v_a and applying the condition for the vertical velocity on the free surface ($y = F$), (2.44), we have that:

$$F_t = \frac{1}{12}\frac{\partial}{\partial x}\left(\frac{\gamma F^4 + 4k^{\frac{1}{2}}F^3 + 6k\gamma\delta F^2}{\gamma F + k^{\frac{1}{2}}}\frac{\partial p_a}{\partial x}\right) + kh\frac{\partial^2 p_a}{\partial x^2}. \tag{4.31}$$

To summarise, the coupled equations for shallow water impact with a porous substrate of thickness H and effective permeability k are

$$F_t = \frac{1}{12}\frac{\partial}{\partial x}\left(\frac{\gamma F^4 + 4k^{\frac{1}{2}}F^3 + 6k\gamma\delta F^2}{\gamma F + k^{\frac{1}{2}}}\frac{\partial p_a}{\partial x}\right) + kh\frac{\partial^2 p_a}{\partial x^2}, \tag{4.32}$$

$$F_{tt} = -p_{a_{xx}}. \tag{4.33}$$

These coupled equations are valid for $(x,t) \in \mathbb{R}^2$.

4.3 Computational results

The numerical method used to solve the coupled equations is the same as that used in Chapters 2 and 3, with however, (4.32) being discretized as

follows, let:

$$A(I+\delta x, J) = (F(I,J) + F(I+\delta x, J)) \times \left(\gamma\left(F^3(I,J) + F^3(I+\delta x, J)\right) + 4k^{\frac{1}{2}}\left(F^2(I,J) + F^2(I+\delta x, j)\right) + 6k\gamma\delta\left(F(I,J) + F(I+\delta x, J)\right)\right) / \left(\gamma(F(I,J) + F(I+\delta x, J)) + 2k^{\frac{1}{2}}\right) + 24kh, \tag{4.34}$$

$$B(I-\delta x, J) = (F(I,J) + F(I-\delta x, J)) \times \left(\gamma\left(F^3(I,J) + F^3(I-\delta x, J)\right) + 4k^{\frac{1}{2}}\left(F^2(I,J) + F^2(I-\delta x, j)\right) + 6k\gamma\delta\left(F(I,J) + F(I-\delta x, J)\right)\right) / \left(\gamma(F(I,J) + F(I-\delta x, J)) + 2k^{\frac{1}{2}}\right) + 24kh. \tag{4.35}$$

So we have:

$$\begin{aligned} &\frac{1}{12}F(I,J-2\delta t) - \frac{2}{3}F(I,J-\delta t) + \frac{2}{3}F(I,J+\delta t) - \frac{1}{12}F(I,J+2\delta t) \\ &= \frac{\delta t}{12(\delta x)^2}\left[\{P(I-\delta x,J)B(I-\delta x,J)\}\right. \\ &- \{P(I,J)\left(B(I-\delta x,J) + A(I+\delta x,J)\right)\} \\ &\left. + \{P(I+\delta x,J)A(I+\delta x,J)\}\right]. \end{aligned} \tag{4.36}$$

The grid size and time step are the same as those used before, $\delta x = 0.016$ and $\delta t = 10^{-3}$, after running accuracy checks these values are still appropriate. With the addition of porosity we have a more complicated equation to discretise but since it only depends on spatial pressure derivatives this just adds extra terms to the existing non-zero terms in the tridiagonal matrix for pressure. The algorithm is the same as in Chapters 2 and 3. We use (3.31) to estimate the free surface position in the new time step then we use (4.36) to update the pressure. We then iterate this process until we have convergence, to achieve convergence, which is when we have an error less than 10^{-4} after substituting the updated free surface and pressure into (4.36).

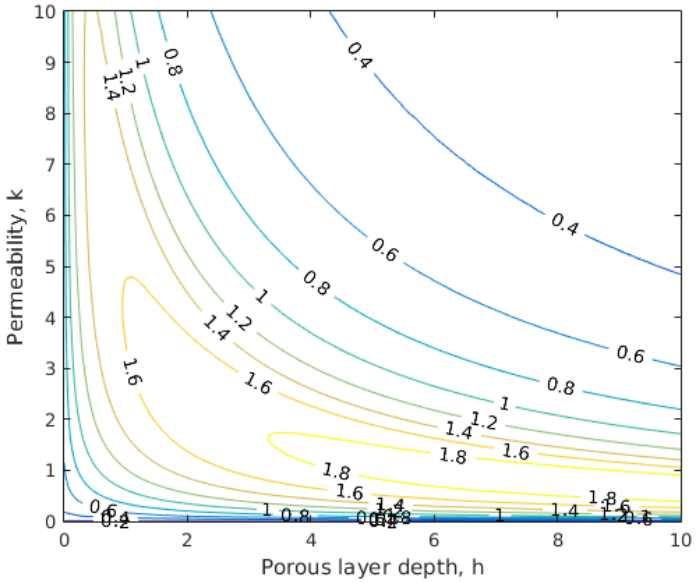

(a) Contours of the touchdown time as a function of k and h

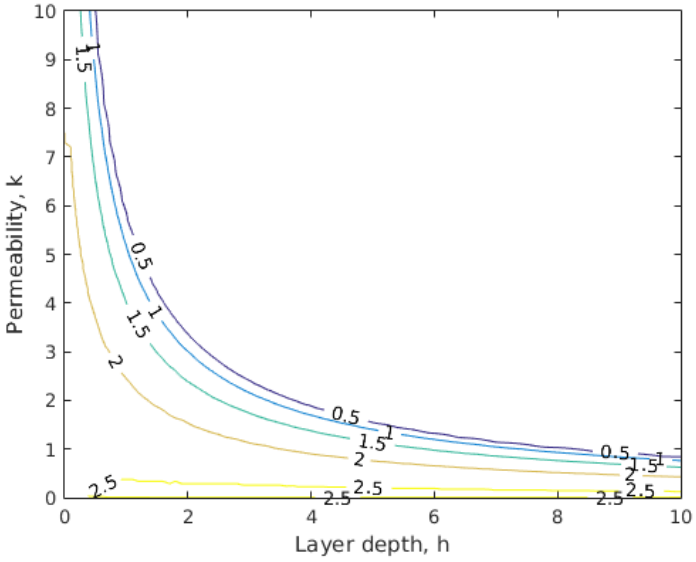

(b) Contours of bubble radius as a function of k and h

Figure 4.2: The touchdown time and the bubble radius plotted as the permeability and layer depth vary (increments 0.1.) Both figures use a time step of 0.002.

Figure 4.2 shows how the touchdown times and bubble radii vary as k and H vary. One immediate observation made from Figure 4.2(a) is that initially as k and H increase the touchdown time occurs later. This result comes as a surprise. Comparing with previous similar work in Hicks and Purvis (2015) shows that for the deep-water case the touchdown time monotonically decreases as k and H increase. For large k and H the touchdown time behaves as expected and decreases monotonically. From Figure 4.2(a) we can see a region for $k \approx 1$ and $H > 4$ where the touchdown time is the most delayed. Close to $k = 0$ we have a contour with touchdown time of 0.2, which matches the results found in Section 3.5 for touchdown time with an impermeable wall. Figure 4.2(b) shows the bubble radius as a function of k and H. The trend in the varying radii can be seen from Figure 4.2(b), for large k and H the radius decreases monotonically. This too can be compared to Hicks and Purvis (2015) who showed that the bubble radius monotonically decreased to zero as k and H increase. For large k and H the results obtained in the present study match with the results of Hicks and Purvis (2015) found for the deep-water case.

Figure 4.3 shows results from varying the permeability k while keeping h constant. It is clear from the free-surface plots that the bubble radius decreases to zero as k increases, for $k = 0.25$ the radius is approximately 2.7: for $k = 2$ the radius is approximately 1.2 and for $k = 4$ there is almost no bubble formed. The touchdown time increases when k is increased from $k = 0.25$ to $k = 2$ then decreases between $k = 2$ and $k = 4$, this is also seen in the contour plot in Figure 4.2(a). The pressures decrease dramatically as k increases with the lower pressures the cushioning effect from the air is much lower for larger k so there is less deformation of the droplet and a smaller bubble formed. However, the phenomena concerning the increase in touchdown time needs to be investigated further, and its physical cause discovered.

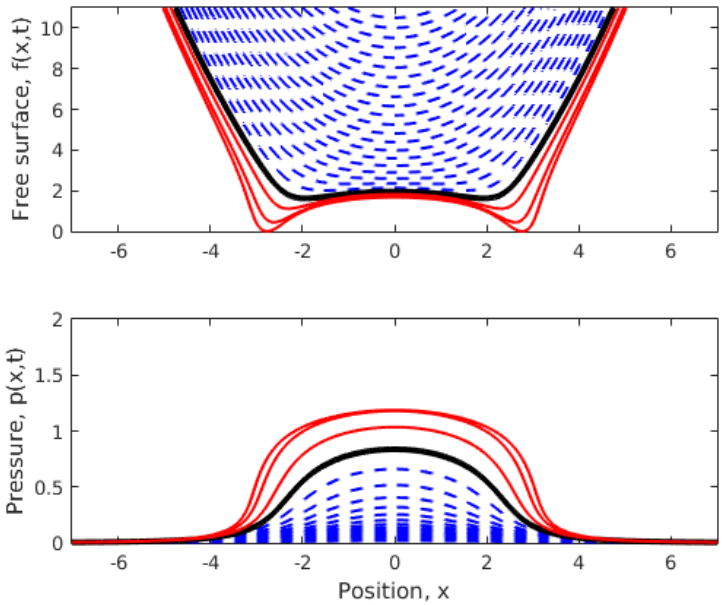

(a) Free-surface and pressures profiles for $k = 0.25$ and $h = 4$, touchdown time is approximately 1.33

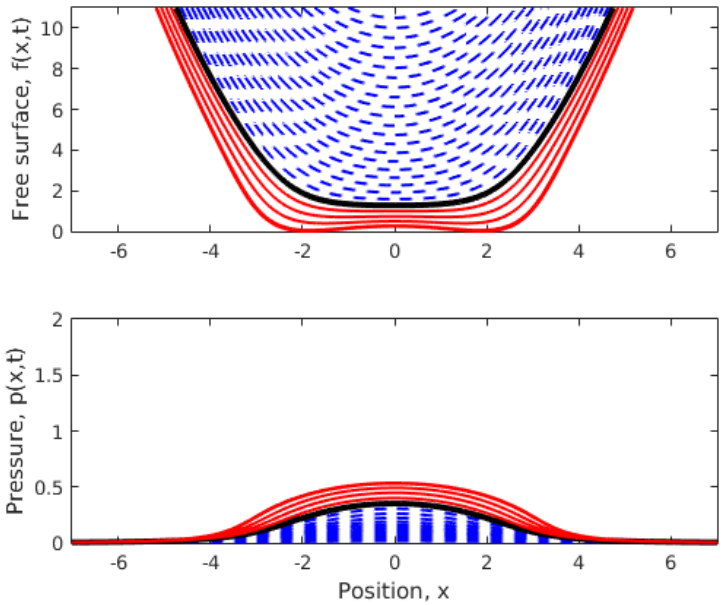

(b) Free-surface and pressures profiles for $k = 2$ and $h = 4$, touchdown time is approximately 1.47

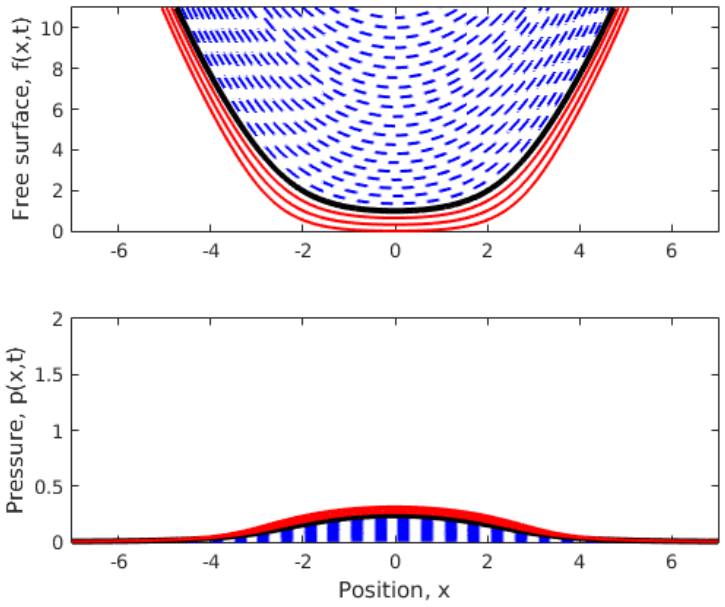

(c) Free-surface and pressures profiles for $k = 4$ and $h = 4$, touchdown time is approximately 0.90

Figure 4.3: Free-surface and pressure profiles for selected values of h with k fixed.

4.4 Discussion of results

The contour plot shown in Figure 4.2(a) shows some unexpected behaviour with the touchdown time for varying k and h. To begin to understand what is happening in this region we will fix h and vary k.

Figure 4.4 shows the separation distance as a function of time for the values of k and h already considered in Figure 4.3. As we can see, for zero permeability (which is identical to having an impermeable base) we have a rapid downwards acceleration of the droplet close to touchdown. Increasing k a small amount we can still see this acceleration close to touchdown, however, the acceleration is smaller. For larger k we have behaviour as we would expect which is the droplet falling at a near constant velocity, as with

high permeability the air can simply flow into the medium, out of the way of the incoming droplet, without much resistance. For large k the results are as one would expect and are less interesting than for small k. Comparing these findings to deep-water impacts with a porous medium as seen in Hicks and Purvis (2015), the touchdown time does not have this interesting behaviour with regions of delayed impact, as seen in the shallow-water case of Figure 4.2(a). With a shallow-water layer we will have less possible deformation of the freesurface so the deceleration will be more uniform across the entire freesurface than with the deep-water case where the droplet can deform more and develop more pronounced minimum points.

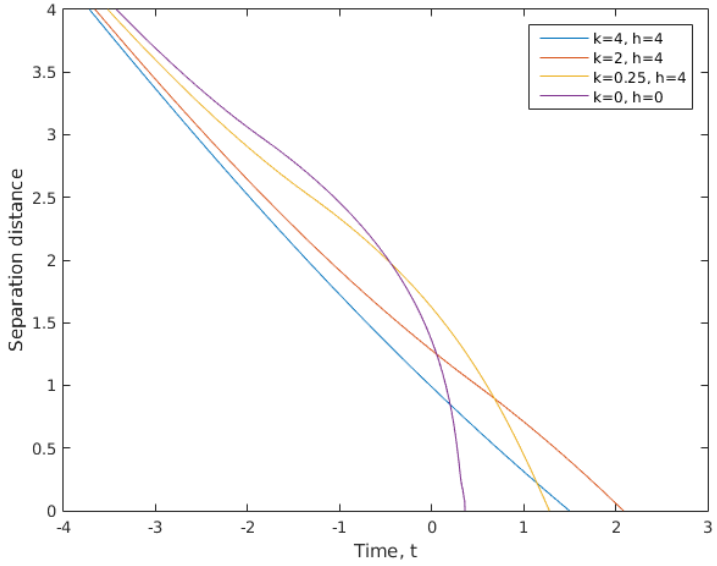

Figure 4.4: Separation distance plots for various values of k and fixing $h = 4$

From the coupled equations we have that the acceleration of the free surface, $F_{tt} = -p_{xx}$, as the rapid acceleration close to touchdown occurs for small values of k and not large values we return to the plots shown in Figure 4.3 and plot the spatial derivatives of the pressure as well to better see this acceleration close to touchdown.

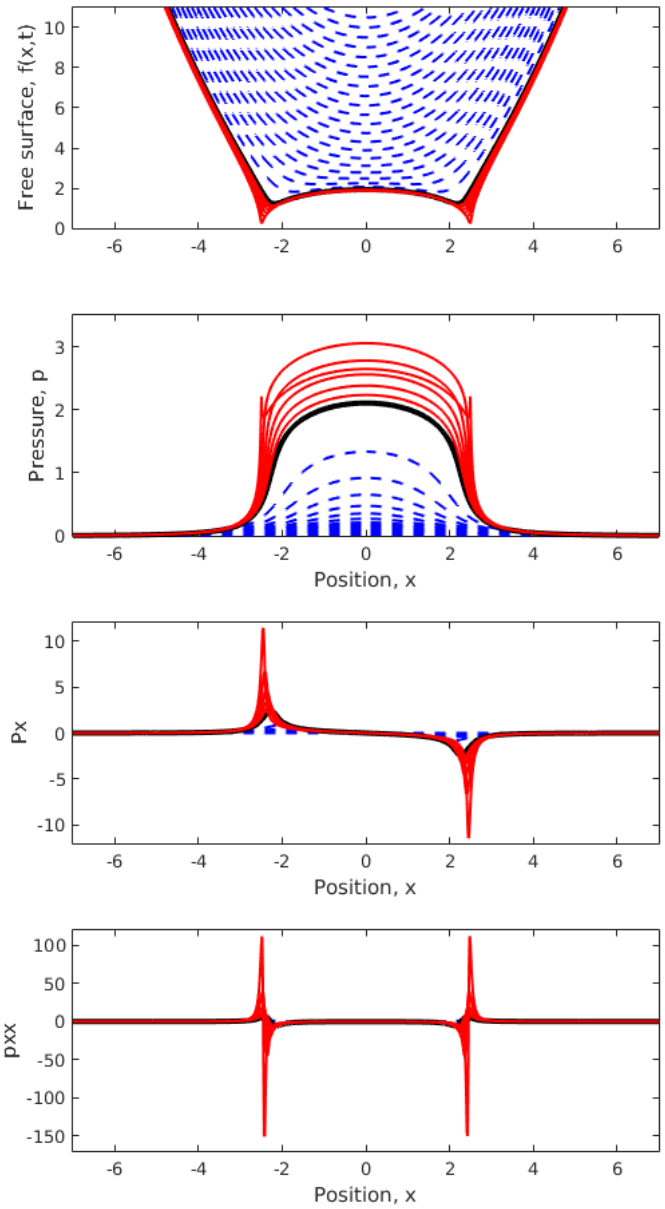

(a) Free surface, pressure and pressure derivative profiles for $k = 0$ and $h = 4$

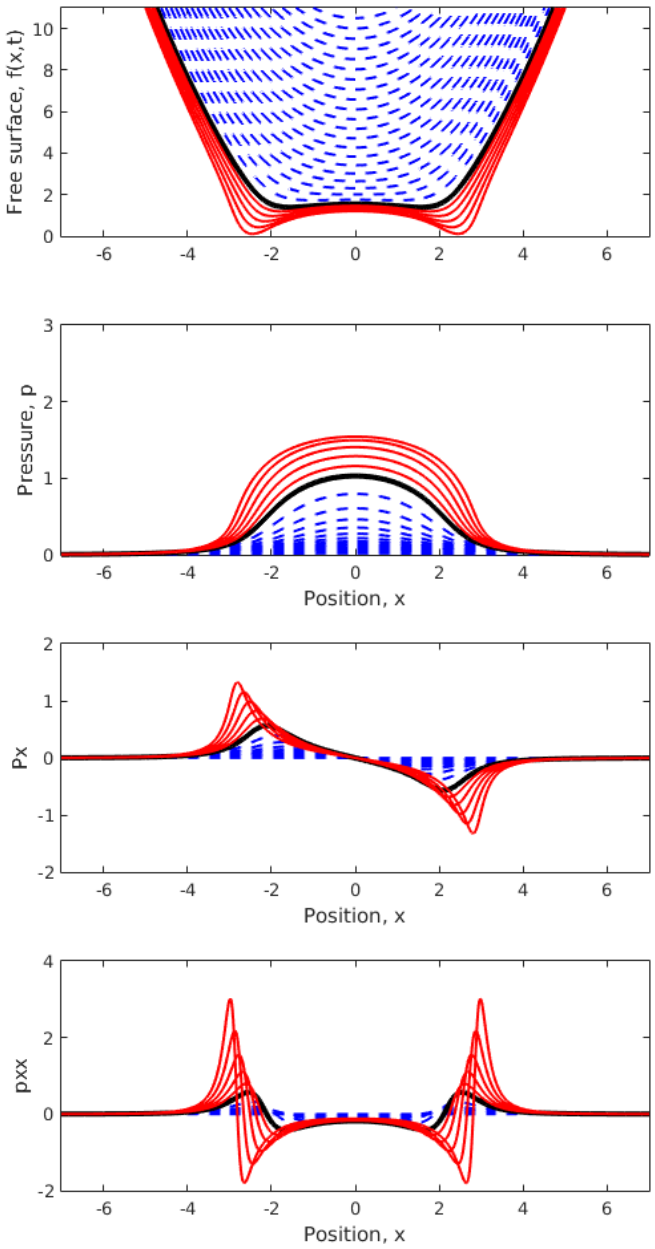

(b) Free surface, pressure and pressure derivative profiles for $k = 0.25$ and $h = 4$

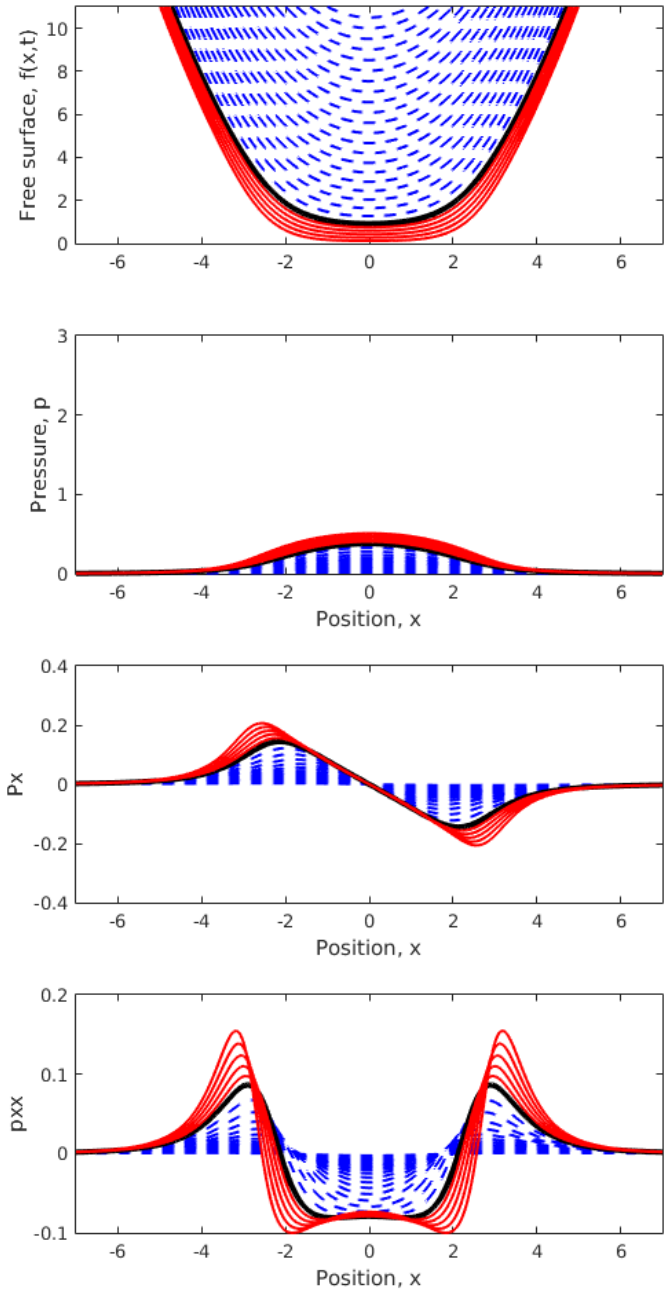

(c) Free surface, pressure and pressure derivative profiles for $k = 2$ and $h = 4$

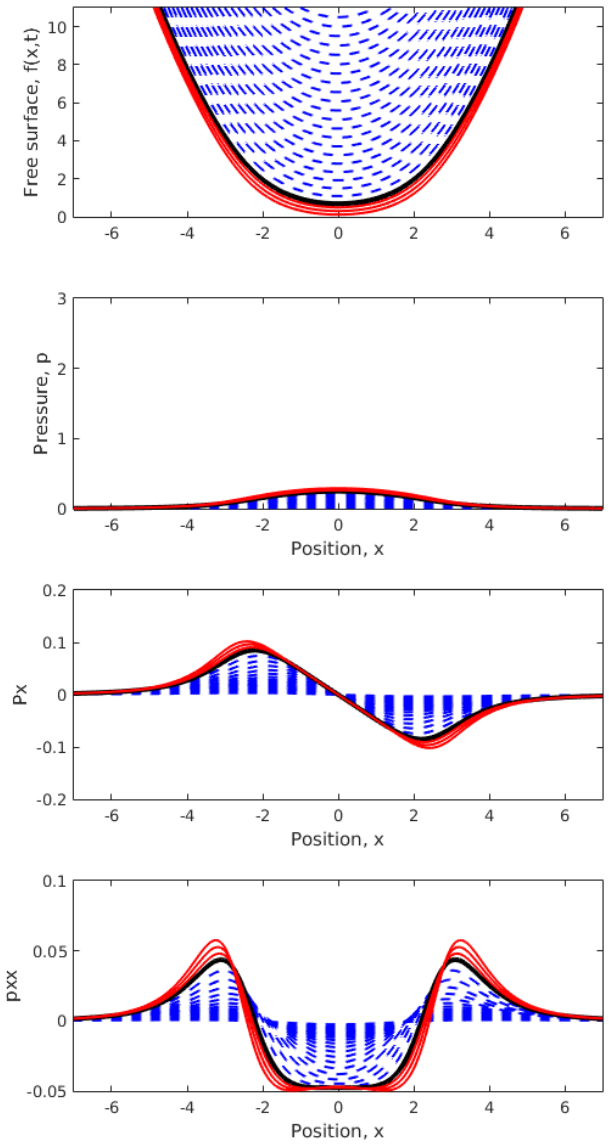

(d) Free surface, pressure and pressure derivative profiles for $k = 4$ and $h = 4$

Figure 4.5: Free surface, pressure and pressure derivative profiles for various values of k with h fixed.

Figure 4.5 shows the distributions for the spatial derivatives p_x and p_{xx} and free-surface of shallow-water layer with various values of k (with h fixed). For the cases where we have two distinct minima, for $k = 0$ and $k = 0.25$, we will consider only the right touchdown position (positive x value) as the plots we are concerned with are all symmetrical about the y-axis. For $k = 0$ and $k = 0.25$ we observe that the minimum free-surface position is slightly to the left of the minimum position on the p_{xx} plot. This means that the acceleration of the free-surface is positive and hence is accelerating upwards, or decelerating in the direction the free-surface is falling. Slightly to the right of this position we can see that p_{xx} is positive now which means this part of the free-surface is accelerating downwards and will pass the current minimum and become the new minimum. This explains the behaviour that the minimum position on the free-surface appears to move away from the centre as time progresses. The accelerations for $k = 0$ are much larger in magnitude than for $k = 0.25$, which can be seen in Figures 4.5(a) and (b). However, the accelerations become very small as k increases to become an $O(1)$ quantity and for large k are negligible, so the droplet's velocity remains close to being constant.

Another result obtained from the derivation of the governing coupled equations is the vertical air velocity on the substrate-air interface, which is directly proportional to p_{xx} (equation 4.24). Looking at Figure 4.5 in more global view, for small k we have that air is entering the substrate under the centre of the droplet with more air entering close to the touchdown positions and leaving the substrate outside where the trapped pocket of air is. For larger k where we observe some similar behaviour, the air enters the substrate under the centre of the droplet and escapes towards the sides of the droplet. As the minimum of this droplet is the centre we have more air entering the substrate here than for small k. As we only have one minimum on the free-surface for large k this can help to explain the locations of the

peaks and troughs of the p_{xx} plot as this is related to the air velocity on the substrate-air interface.

Figure 4.6 shows how the touchdown times vary with k when h is fixed. An unexpected observation is for each value of h used here, the k value corresponding to the most delayed touchdown time is approximately half of the critical value of k for the same h. However, this will be looked into more precisely with a finer grid size and more values of k and h considered.

An alternative approach to understand the mechanisms at work is to consider this problem in a different way. Close to touchdown we will use the numerical results already presented to fix the shape of the free-surface and approximate it as a polynomial and substitute this back into equation (4.32) and solve for the pressure distribution. This will approximate the problem into a squeeze-film flow.

For large k we observe from the numerical result there is not very much change in the free-surface shape so we will approximate the free-surface as:

$$F(x,t) = \frac{x^2}{2} - t, \tag{4.37}$$

as we assumed this is the shape of the undisturbed droplet when we release it. As we have fixed the shape of the free-surface we now have a solid body falling towards a porous medium so one of the coupled model equations is no longer relevant. However, we still have a relation:

$$F_t = \frac{1}{12}\frac{\partial}{\partial x}\left(\frac{\gamma F^4 + 4k^{\frac{1}{2}}F^3 + 6k\gamma\delta F^2}{\gamma F + k^{\frac{1}{2}}}\frac{\partial p_a}{\partial x}\right) + kh\frac{\partial^2 p_a}{\partial x^2}, \tag{4.38}$$

to satisfy. We proceed by substituting in our approximation for F, and we integrate with respect to x (we will take $\gamma = \delta = 1$,) so we have:

$$-x + c(t) = p_x\left(\frac{1}{12}\frac{\left(\frac{x^2}{2} - t\right)^4 + 4k^{\frac{1}{2}}\left(\frac{x^2}{2} - t\right)^3 + 6k\left(\frac{x^2}{2} - t\right)^2}{\left(\frac{x^2}{2} - t\right) + k^{\frac{1}{2}}} + kh\right). \tag{4.39}$$

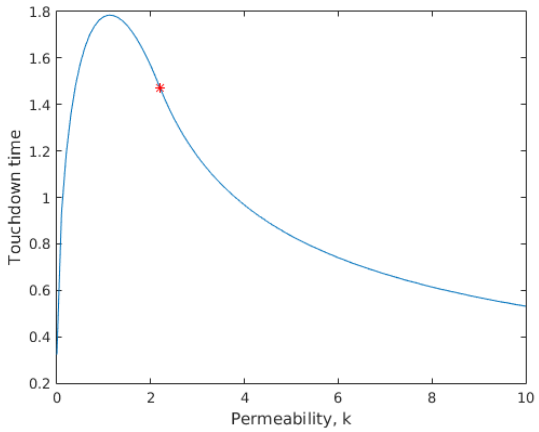

(a) Touchdown times for $h = 3.5$ as a function of k

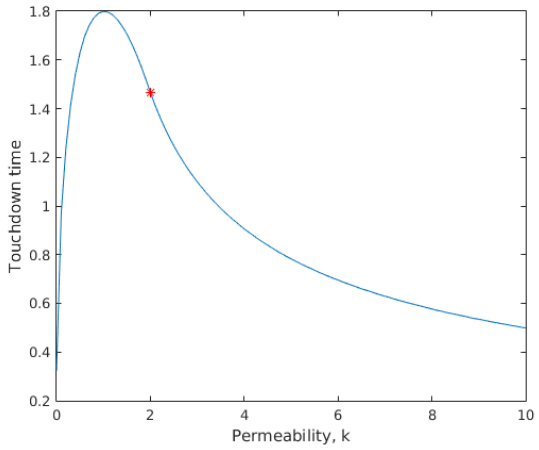

(b) Touchdown times for $h = 4$ as a function of k

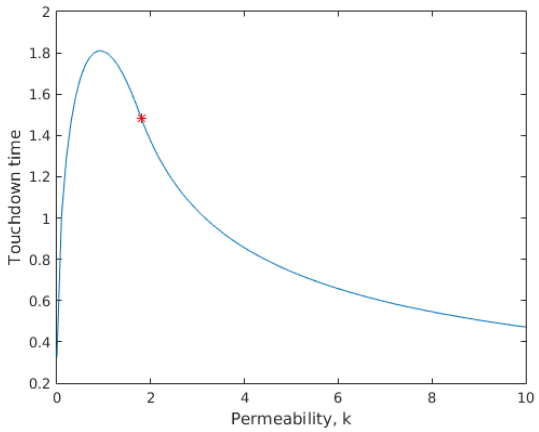

(c) Touchdown times for $h = 4.5$ as a function of k

Figure 4.6: Touchdown times as a function of k for various values of fixed h. The red star indicates the critical value of k where we only have one minimum point at touchdown.

Upon rearranging for $p_x(x,t)$ we have:

$$p_x(x,t) = \frac{-x}{\left(\frac{1}{12}\frac{\left(\frac{x^2}{2}-t\right)^4+4k^{\frac{1}{2}}\left(\frac{x^2}{2}-t\right)^3+6k\left(\frac{x^2}{2}-t\right)^2}{\left(\frac{x^2}{2}-t\right)+k^{\frac{1}{2}}}+kh\right)}, \tag{4.40}$$

note we have taken $c(t) = 0$ as from the numerical results we can see that $p_x(0,t) = 0$.

Using (4.40) we can plot functions $p(x,t)$, $p_x(x,t)$ and $p_{xx}(x,t)$ and compare with the previous findings.

Figure 4.7 has some strong similarities to the other numerical findings shown in Figure 4.5(d). Fixing the free-surface with an approximate shape in the form of a polynomial was only taking into account the shape of the free surface close to touchdown. So comparisons can only be made with the last time steps plotted in Figure 4.5(d). The amplitudes of the curves in Figure 4.7 are slightly larger than in Figure 4.5, this is because we have a solid body falling towards the substrate, so there can be no deformation of the free-surface, unlike for the case with a layer of water. The locations of the peaks and troughs for p_x and p_{xx} are close to the positions of these in the numerical results and have very similar amplitudes. There is good agreement in the shape between these two sets of plots.

For small k we approximate the free-surface shape close to touchdown as a quartic polynomial:

$$F(x,t) = 0.03014x^4 - 0.3472x^2 + 1 - t, \tag{4.41}$$

the coefficients are obtained by approximating the touchdown positions as $x = \pm 2.4$ and $F(0,t) = 1$. Repeating the same method as for large k we can also plot the functions $p(x,t)$, $p_x(x,t)$ and $p_{xx}(x,t)$.

Figure 4.8 shows the results for the pressure pressure distribution when fixing the free-surface close to touchdown for small k as given in equation (4.41). We can compare these results to the last time steps in Figure 4.5(b). We have good agreement between the shapes of the two sets of results.

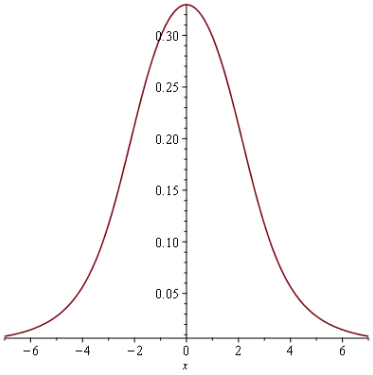

(a) Pressure distribution calculated from fixing the free surface for large k.

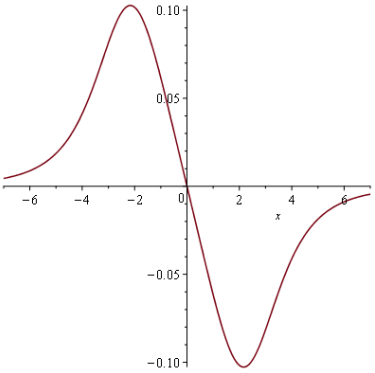

(b) First spatial derivative of the pressure distribution from fixing the free surface for large k.

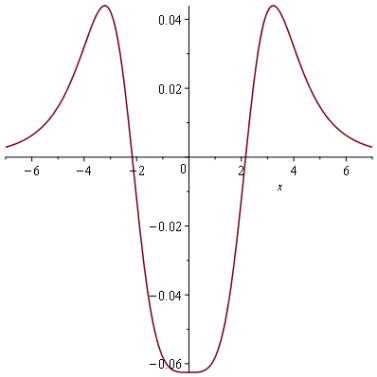

(c) Second spatial derivative of the pressure distribution from fixing the free surface for large k.

Figure 4.7: Plots for the pressure distribution and spatial derivatives from fixing the free-surface and solving for the pressure for large k, here $k = 4$ and $h = 4$ were used.

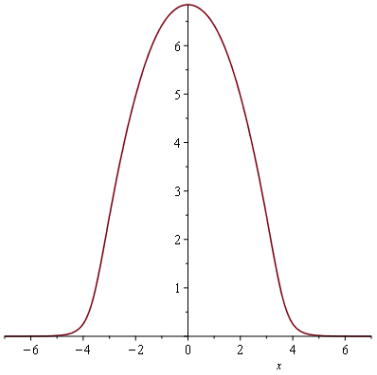

(a) Pressure distribution calculated from fixing the free surface with small k.

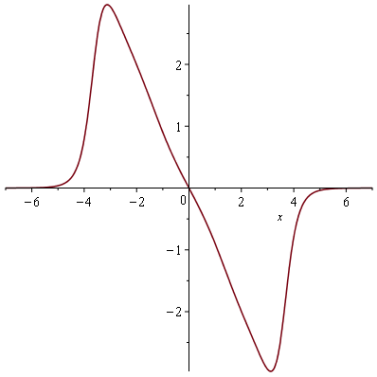

(b) First spatial derivative of the pressure distribution from fixing the free surface with small k.

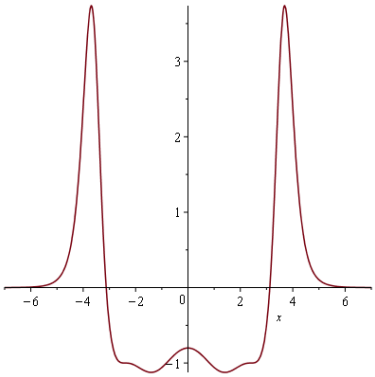

(c) Second spatial derivative of the pressure distribution from fixing the free surface with small k.

Figure 4.8: Plots for the pressure distribution and spatial derivatives from fixing the free-surface and solving for the pressure for a small k, here $k = 0.25$ was used with $h = 0$.

The amplitudes of the plots, particularly the pressure distribution, are considerably higher. This is due to the fact that we have modelled a solid non-deformable surface falling towards the substrate. The peaks in the p_x and p_{xx} plots are in slightly different locations, compared with the peaks in Figure 4.8, being further away from the centre of the droplet. There is still good agreement between the shapes of two sets of plots, with a lower porosity we would expect increased deformation of the free-surface in response to the higher pressures compared with the higher porosity case where we have lower air pressures. We can conclude that the pressure distribution shape depends on the shape of the incoming surface.

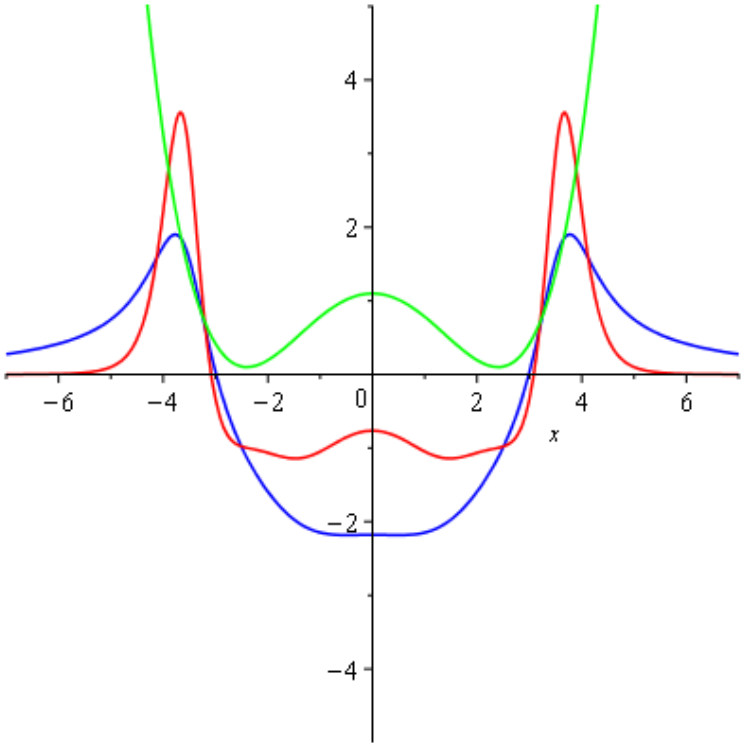

Figure 4.9: Plot to compare free-surface accelerations for deep water (blue) and shallow water (red) droplet impacts to free-surface shape (green).

Figure 4.9 shows a comparison between the accelerations of the free surface for the deep- and shallow-water cases alongside the approximated

free surface shape for a small value of the permeability. The acceleration for the deep-water case was approximated by substitution of the approximated free surface shape into (4.32) to obtain p_x then this was further substituted into (2.53) to obtain an approximation for the acceleration of the free surface. Similarities between the two cases are the locations for the peaks of the acceleration. However the interesting difference comes from the magnitude of this peak, it is approximately twice are large for the shallow-water layer impact meaning the acceleration into touchdown is much larger for this case. The deceleration for deep-water droplet under the formed bubble is approximately twice as large. The greater deceleration of the deep-water droplet and the larger acceleration of the shallow-water layer both support the previous numerical findings that the shallow-water layers touchdown much faster than the water droplets for small permeability.

4.5 Conclusions

In this chapter derivation of a model for a shallow-water layer impact onto a thin porous surface was given. There were similarities between the two derivations which were largely the lubrication equation for the air-flow. The difference lies in the relationship between the pressure and the second time-derivative of the free-surface, with the deep-water case having a global relationship, and the shallow-water case having a local relationship. This difference can be seen in the computational results. The deep-water case had the maximum pressure under the lowest point on the free-surface. But the shallow-water case had small cusps under the lowest points of the free-surface. The maximum pressure occurred under the centre of the droplet.

The coupled equations for shallow-water layer impacts onto porous substrate were also derived. Similarities in the equations are the local relationship between the second time-derivative of the free-surface position and the pressure distribution. The difference in the coupled equations lies in

the coupled air flow in the porous medium and air layer. The main result shown was the touchdown times for varying permeability and porous layer depth. These differ from the results for deep-water droplet impact onto a porous medium. They show that the touchdown time initially increases and later decreases. Plots for selected values of permeability and layer depth supported this finding. The radii of the bubbles were investigated and their dependence on varying permeability and layer depth were as expected. The radii monotonically decrease to zero, with the other plots given also supporting this.

5

Impact with thicker porous layers

5.1 Introduction

In this chapter we extend the model covered in the previous chapter and look at different depths of porous media. This new model will incorporate porous layer depths where the horizontal and vertical length scales are comparable and also an infinite depth layer. A system which couples the air and water equations and the air flow in the substrate will be derived and solved numerically.

5.2 Derivation of governing equations

In the previous chapter a shallow porous layer was considered, the depth of the porous layer was an order of magnitude smaller than the width. However, for the intermediate depth porous layer the length scales are comparable, and with this we do not need to assume the velocities in the substrate are disparate. With this change we can write the scalings for the water, air and the substrate as:

$$(u_w^*, v_w^*, p_w^*, x^*, y^*, t^*) = \left(u_w, v_w, \epsilon^{-1} p_w, \epsilon x, \epsilon y, \epsilon^2 t\right), \tag{5.1}$$

$$(u_a^*, v_a^*, p_a^*, x^*, y^*, t^*) = \left(\epsilon^{-1} u_a, v_a, \epsilon^{-1} p_a, \epsilon x, \epsilon^2 y, \epsilon^2 t\right), \tag{5.2}$$

$$(u_s^*, v_s^*, p_s^*, x^*, y^*, t^*, H^*) = \left(u_s, v_s, \epsilon^{-1} p_s, \epsilon x, \epsilon y, \epsilon^2 t, \epsilon^2 H\right). \tag{5.3}$$

The derivation for the equation for the liquid is the same as in Section 3.3, so again we adopt equation (3.27). The derivation for the air layer is almost unchanged, however, we will have a slightly different boundary condition from the Beavers-Joseph condition in equation (4.5): the horizontal velocity scale is now the same size as the vertical velocity scale. Upon applying the scales, the air-substrate boundary condition becomes:

$$\frac{k^{\frac{1}{2}}}{\gamma}\frac{\partial u_a}{\partial y} = u_a, \tag{5.4}$$

the δ term disappears as it is now small compared to the dominant terms in (5.4), thus we have:

$$u_a = \frac{(F-y)\left(\left(\gamma F + k^{\frac{1}{2}}\right)y + k^{\frac{1}{2}}F\right)}{2\left(\gamma F + k^{\frac{1}{2}}\right)}\frac{\partial p_a}{\partial x} \qquad \text{for } 0 < y < F(x,t). \tag{5.5}$$

From the conservation of mass equation and by substituting in the Darcy velocities (4.3) and (4.4) we can see that the substrate pressure has to satisfy Laplace's equation with the boundary conditions: the pressure and vertical air velocities have to be continuous on the air-substrate interface and zero normal velocity component on the impermeable base of the medium, thus we have:

$$\nabla^2 p_s(x,y,t) = 0, \tag{5.6}$$

$$p_s(x,0,t) = p_a(x,t), \tag{5.7}$$

$$v_s(x,0,t) = v_a(x,0,t), \tag{5.8}$$

$$v_s(x,-H,t) = 0. \tag{5.9}$$

Proceeding from equation (5.5) in the same way as before, however, we note the vertical air velocity on the surface of the substrate is $v_s(x,0,t) = V(x,t)$, so we have the equation from the air layer:

$$F_t = \frac{1}{12}\frac{\partial}{\partial x}\left(\frac{\gamma F^4 + 4k^{\frac{1}{2}}F^3}{\gamma F + k^{\frac{1}{2}}}\frac{\partial p_a}{\partial x}\right) + V. \tag{5.10}$$

This is coupled to equation (3.27), however, we now have a dependence on the vertical air velocity on the surface of the substrate, in order to calculate this we must first solve for the substrate pressure using (5.6)-(5.9), which yields a more complicated coupled system of equations compared with the previous cases. In summary, the coupled system for a shallow-water layer impact onto an intermediate depth porous layer with porosity k and depth H is:

$$F_t = \frac{1}{12}\frac{\partial}{\partial x}\left(\frac{\gamma F^4 + 4k^{\frac{1}{2}}F^3}{\gamma F + k^{\frac{1}{2}}}\frac{\partial p_a}{\partial x}\right) + V, \tag{5.11}$$

$$F_{tt} = -p_{a_{xx}}, \tag{5.12}$$

$$\nabla^2 p_s(x, y, t) = 0, \tag{5.13}$$

$$p_s(x, 0, t) = p_a(x, t), \tag{5.14}$$

$$\frac{dp_s}{dy} = 0 \qquad \text{on } y = -H, \tag{5.15}$$

$$p_s \to 0 \qquad \text{as } |x| \to \infty. \tag{5.16}$$

5.3 Solving in the substrate

We use an image system to solve Laplace's equation in the substrate. We are solving it in a rectangular region of depth H, with zero normal component of velocity on the base ($v_s = 0$) of the substrate and air pressure equal on the air-substrate interface. We reflect this system in the base of the substrate and use Cauchy's integral formula to solve. Let $\hat{z} = x + iy$ and we introduce a complex analytic function $w(\hat{z}, t)$ given by:

$$w(\hat{z}, t) = kp_{s_x}(\hat{z}, t) + iv_s(\hat{z}, t), \tag{5.17}$$

as kp_{s_x} add v_s satisfy the Cauchy Riemann equations. By Cauchy's integral formula with the contour defined as the perimeter of this rectangular area we have:

$$w(\hat{z}, t) = \frac{1}{2\pi i}\oint_\Gamma \frac{w(\hat{z}, t)}{z - \hat{z}}dz, \tag{5.18}$$

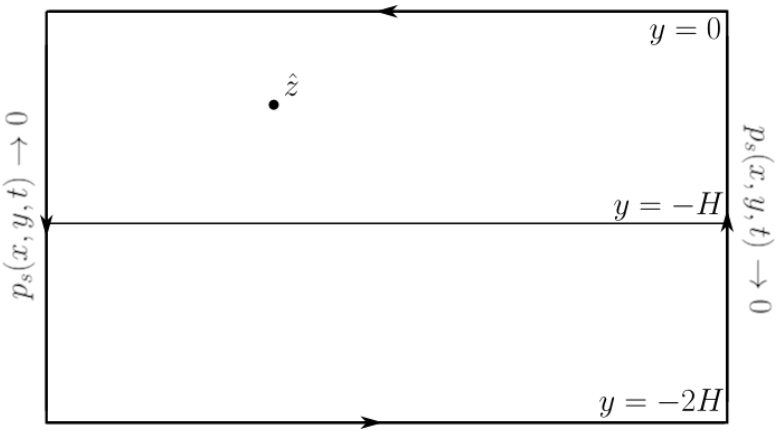

(a) The field point, $\hat{z}$, is not on the contour

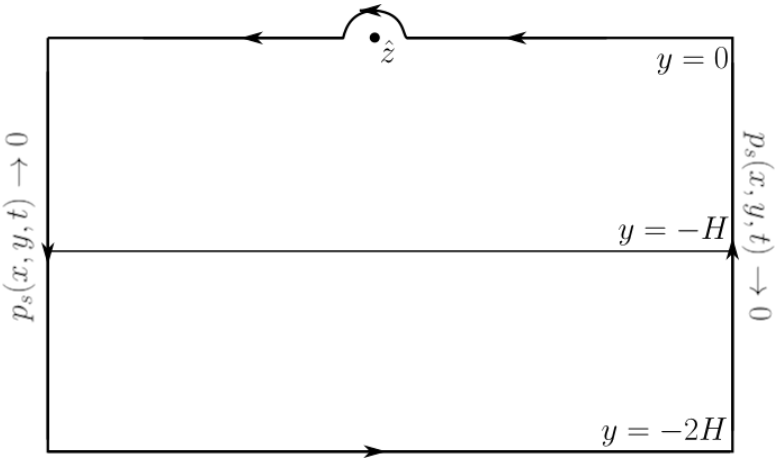

(b) The field point, $\hat{z}$, is on the contour on the real axis at $\hat{z} = x$

Figure 5.1: Diagrams showing the contour of integration, Γ, around the porous layer and its reflection in $y = -H$ depending on where our point lies.

This is assuming the integrals at $x = \pm\infty$ give zero contribution, as we extend infinitely in the horizontal direction the integrand tends to zero. Here we have different forms of this contour integral depending on whether our point $\hat{z}$ lies on the contour or not. If our point does not lie on the contour we have:

$$w(\hat{z}, t) = \frac{1}{2\pi i}\left(\int_{\infty}^{-\infty} \frac{w}{x - \hat{z}} dx + \int_{-\infty}^{\infty} \frac{w}{x - 2Hi - \hat{z}} dx\right). \tag{5.19}$$

If $\hat{z} = x$ then we have to deform the contour around this point. In (5.18) the factor $\frac{1}{2}$ changes to 1, accommodating the contribution from the semicircular indentation described above in figure 5.1, we have a principal value integral from taking the limit of the radius of this indentation to zero. For more in depth detail please see Carrier, Krook and Pearson (2005).

We take $Im(\hat{z}) = 0$ as we are interested in the solution on $y = 0$, this also means we can substitute the substrate pressure with the air pressure since this is one of the conditions we imposed at the air-substrate interface. So we have:

$$kp_{s_x} + iv = \frac{1}{i\pi}\left(P.V.\int_{\infty}^{-\infty}\frac{kp_{a_x} + iv}{x - \hat{x}}dx + \int_{-\infty}^{\infty}\frac{kp_{a_x} - iv}{x - 2Hi - \hat{x}}dx\right) \tag{5.20}$$

$$= \frac{1}{i\pi}\left(P.V.\int_{\infty}^{-\infty}\frac{kp_{a_x} + iv}{x - \hat{x}}dx + \int_{-\infty}^{\infty}\frac{(kp_{a_x} - iv)(x - \hat{x} + 2Hi)}{(x - \hat{x})^2 + 4H^2}dx\right). \tag{5.21}$$

Here we choose to take the imaginary part to obtain an expression for the air velocity on the surface of the substrate as a function of pressure. An equivalent expression comes from taking the real part, leaving an expression for the unknown pressure, but this is of less use in the solution. So we have the following integral equation for $v(x, t)$:

$$v = \frac{1}{\pi}\left(P.V.\int_{\infty}^{-\infty}\frac{-kp_{a_x}}{x - \hat{x}}dx + \int_{-\infty}^{\infty}\frac{-kp_{a_x}(x - \hat{x}) - 2Hv}{(x - \hat{x})^2 + 4H^2}dx\right). \tag{5.22}$$

The first integral in (5.22) is simply a Hilbert transform.

5.3.1 Air velocity components

We have an explicit form for the horizontal component of the air velocity (4.30) taking $\gamma = 1$ and $\delta = 0$. From (5.4) we have the only term with δ dependence is far smaller so we ignore it here. We have $\gamma = 1$ to allow slip on the substrate-air interface, we have:

$$u_a = \frac{(y - F)\left(\left(F + k^{\frac{1}{2}}\right)y + k^{\frac{1}{2}}F\right)}{2\left(F + k^{\frac{1}{2}}\right)}\frac{\partial p_a}{\partial x}, \tag{5.23}$$

for the horizontal velocity component we have to use the conservation of mass equation. We so have:

$$v_a = \int_0^y \frac{\partial u_a}{\partial x} dy, \tag{5.24}$$

and after substituting in the horizontal velocity component we have:

$$\begin{aligned} v_a =& 2F_x(2F + k^{\frac{1}{2}})^{-2}(\frac{1}{2}F^2y^2 - \frac{1}{3}Fy^3 - \frac{1}{3}k^{\frac{1}{2}}y^3 + F^2k^{\frac{1}{2}}y)p_x \\ &- (2F + k^{\frac{1}{2}})^{-1}(FF_xy^2 - \frac{1}{3}F_xy^3 - \frac{1}{3}k^{\frac{1}{2}}y^3 + 2FF_xk^{\frac{1}{2}}y)p_x \\ &- (2F + k^{\frac{1}{2}})^{-1}(\frac{1}{2}F^2y^2 - \frac{1}{3}Fy^3 - \frac{1}{3}k^{\frac{1}{2}}y^3 + F^2k^{\frac{1}{2}}y)p_{xx}. \end{aligned} \tag{5.25}$$

5.4 Numerical results

The typical method involving discretisation for solving this system of equations that has been used for most previous cases works poorly here. The computer run time using the same grid sizes is considerably longer here (over 24 hours per set of parameters) and was not practical to produce all results. A Fast Fourier Transform (FFT) method for solving this system was used which has run times comparable to previous systems.

The discrete Fourier expansions of the functions p_a, F and v_s are given by:

$$p_a(x,t) = \sum_{n=1}^{N} P_n(t) e^{\frac{in\pi x}{L}}, \tag{5.26}$$

$$F(x,t) = \frac{x^2}{2} - t + \sum_{n=1}^{N} F_n(t) e^{\frac{in\pi x}{L}}, \tag{5.27}$$

$$v_s(x,t) = \sum_{n=1}^{N} V_n(t) e^{\frac{in\pi x}{L}}. \tag{5.28}$$

From (5.22) we have that:

$$\begin{aligned} v_s(x,0,t) = \frac{1}{\pi}\Bigg(P.V. \int_{-\infty}^{\infty} \frac{k\frac{\partial p_a(\zeta,t)}{\partial \zeta}}{\zeta - x} \mathrm{d}\zeta - \int_{-\infty}^{\infty} \frac{k(\zeta - x)\frac{\partial p_a(\zeta,t)}{\partial \zeta}}{(\zeta - x)^2 + 4H^2} \mathrm{d}\zeta \\ - \int_{-\infty}^{\infty} \frac{2Hv_s(\zeta,t)}{(\zeta - x)^2 + 4H^2} \mathrm{d}\zeta \Bigg), \end{aligned} \tag{5.29}$$

with the help of Gradshteyn and Ryzhik (2000) we substitute in the Fourier expansions (5.26)-(5.28) and can explicitly write down V_n in terms of P_n:

$$V_n = -\frac{k|n|\pi}{L}P_n + \frac{k|n|\pi}{L}e^{\frac{-2H|n|\pi}{L}}P_n - e^{\frac{-2H|n|\pi}{L}}V_n \tag{5.30}$$

$$\left(1 + e^{\frac{-2H|n|\pi}{L}}\right)V_n = \left(-\frac{k|n|\pi}{L} + \frac{k|n|\pi}{L}e^{\frac{-2H|n|\pi}{L}}\right)P_n. \tag{5.31}$$

We used $N = 2001$ terms of the series, with the Fourier transform of the functions taken, the coefficients for the pressure, free surface and air-substrate vertical velocity component could be expressed in terms of each other. At each time step we calculate the series of P_n from the functions from the previous time step then use the relation (5.12) to update F_n:

$$F_{ntt} = -\frac{n^2\pi^2}{L^2}P_n, \tag{5.32}$$

we discretise F_{ntt} to have an expression for the coefficients of the current-time step free surface. We use these to update V_n, to which we use the relationship described in (5.11) to update the pressure and check the error. We iterate this process until we have convergence, a relative error less than $(< 10^{-4})$.

Figure 5.2 shows the impermeable case run with this alternative code to solve the system. The major difference between using this method and the discretisation method is resolving the cusps formed in the spatial distribution of pressure, moments before touchdown. Running the Fourier transform code with a large number of outputs just before touchdown does show these cusps forming. Figures 5.3 - 5.5 show various profiles exploring some of the parameter space. One interesting observation comes from looking at the touchdown times across each of the situations compared to the impermeable case. In all cases we have a more delayed touchdown with a porous layer present. We would expect a less delayed touchdown due to the air able to enter the layer giving lower air pressures and deforming the droplet less. Changing H has less influence on touchdown time compared to changing k

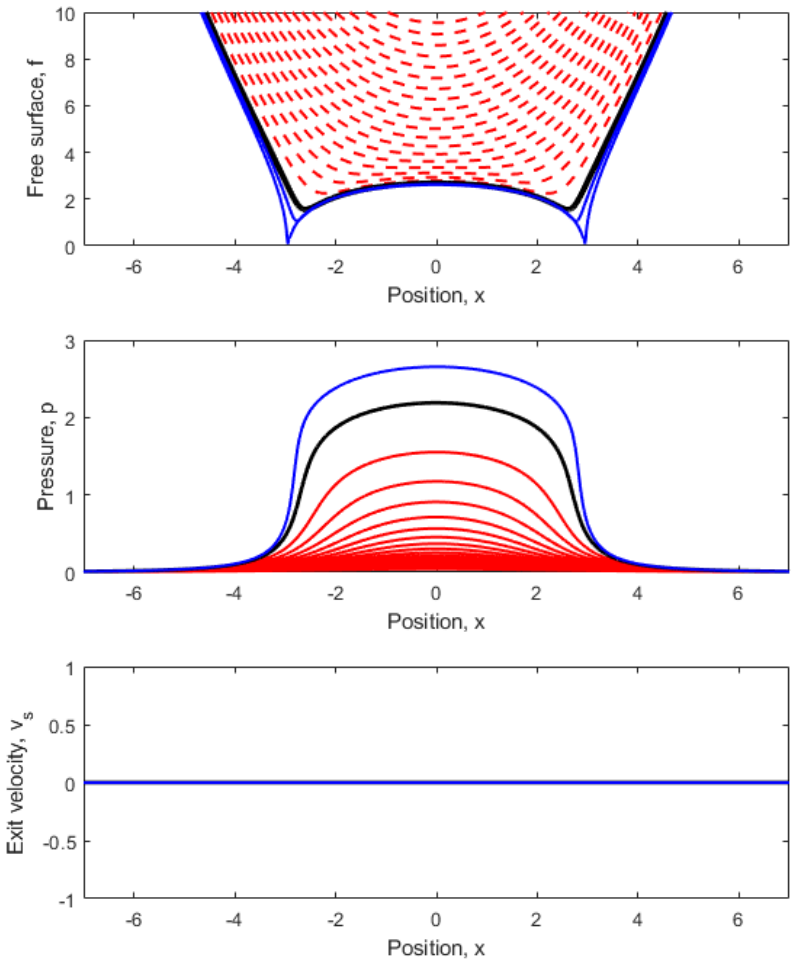

Figure 5.2: Fast Fourier transform method ran on an impermeable substrate

with $k = 1$ the touchdown time was close to $t = 1.2$ with $k = 0.1$ touchdown time was close to $t = 0.7$ and with $k = 0$ touchdown was around $t = 0.37$ ($t = 0$ represents touchdown time in a vacuum).

This change in touchdown time was investigated further. Figure 5.6 shows a comparison between the separation distances of some cases as a function of time. As discussed in Chapter 3 we have a rapid acceleration into touchdown for the impermeable case. This acceleration is deceased

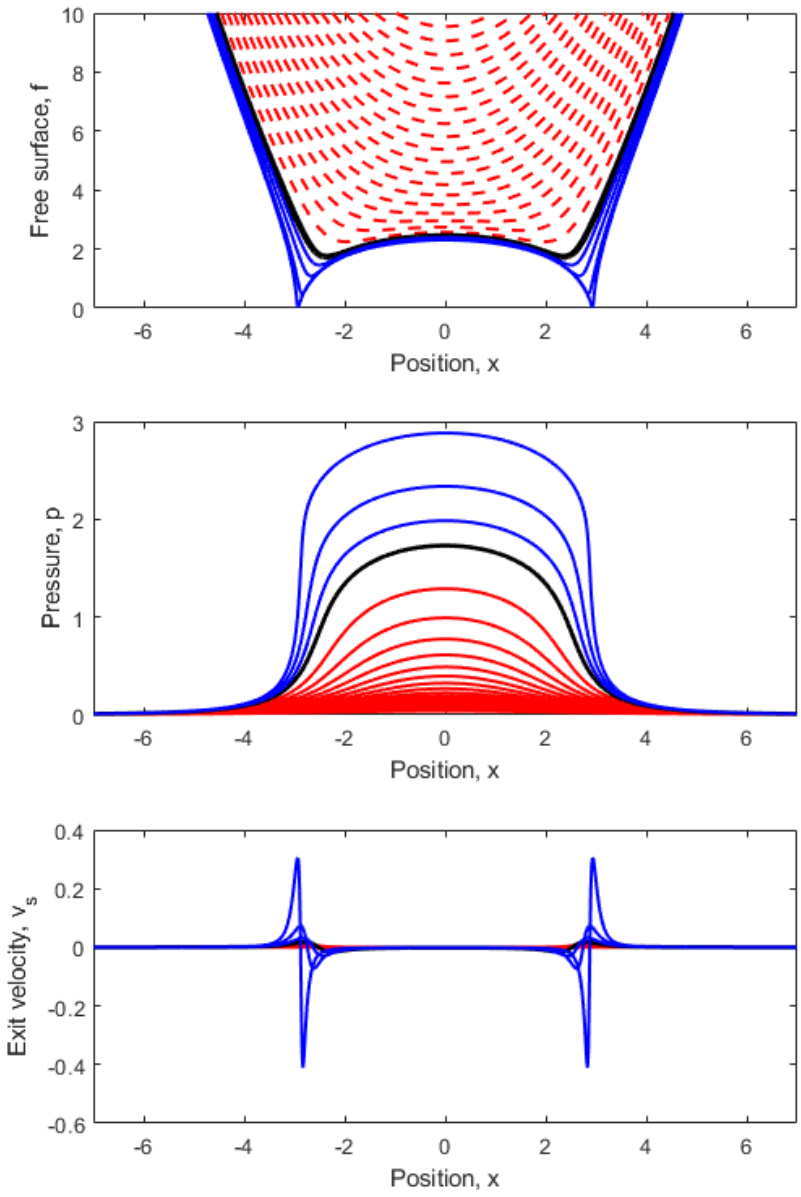

Figure 5.3: Free surface, pressure and substrate exit velocity profiles for $k = 0.1$ and $H = 0.1$, touchdown time is at $t = 0.7$

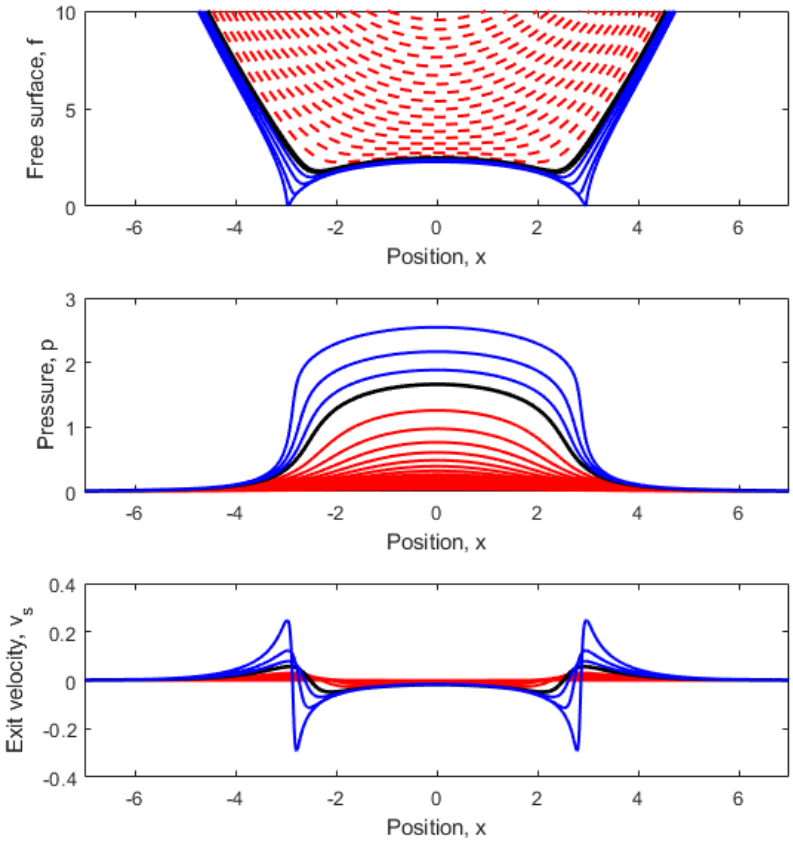

Figure 5.4: Free surface, pressure and substrate exit velocity profiles for $k = 0.1$ and $H = 1$, touchdown time is at $t = 0.7$

with the introduction of this porous layer the higher the porosity the less this acceleration is and so touchdown time is delayed compared with the impermeable case. To try and understand why this acceleration is reduced we look at the air velocity components.

Figure 5.7 shows the air velocity component profiles taken at a constant $y = 0.1$. We can immediately see that most of the air flow in and out of the substrate happens around the touchdown position with near zero flow away from this position. We can see this large vertical jet of air which is very

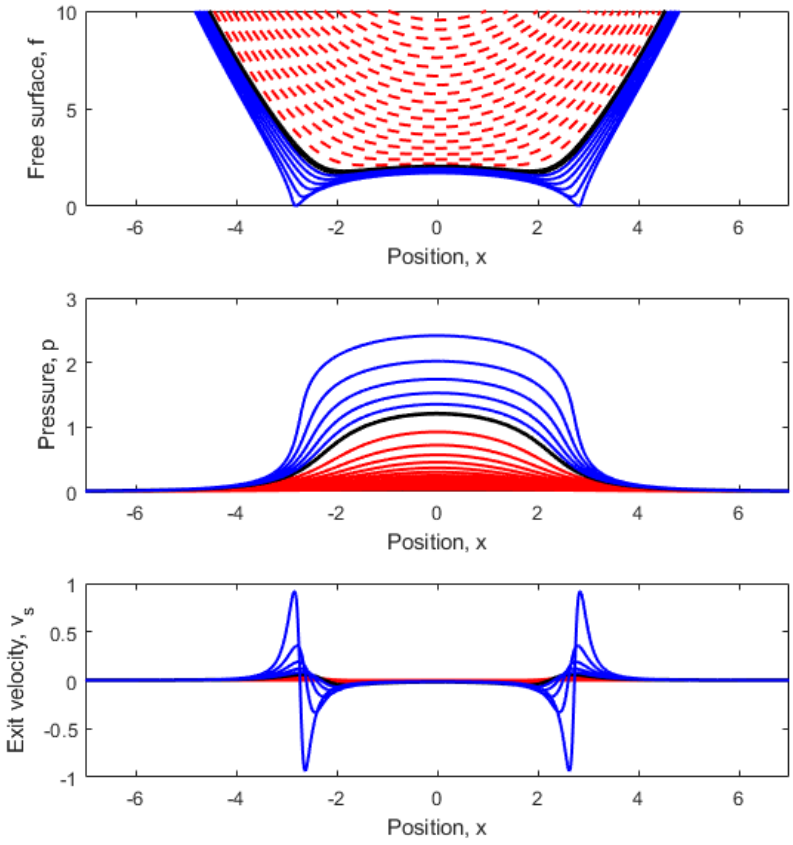

Figure 5.5: Free surface, pressure and substrate exit velocity profiles for $k = 1$ and $H = 0.1$, touchdown time is at $t = 1.2$

slightly on the outside of the bubble of air formed between the two minima of the free surface. One potential mechanism for this delayed touchdown is that due to this very large air current the free-surface cannot as easily go down as there is the large pressure in the bubble formed on the inside and this large jet on the outside of the bubble. With both of these effects it would take longer for the droplet to touchdown.

Comparing this to a higher porosity we have figure 5.8. Here we have $k = 1$, with the higher porosity we have lower pressures, lower vertical and

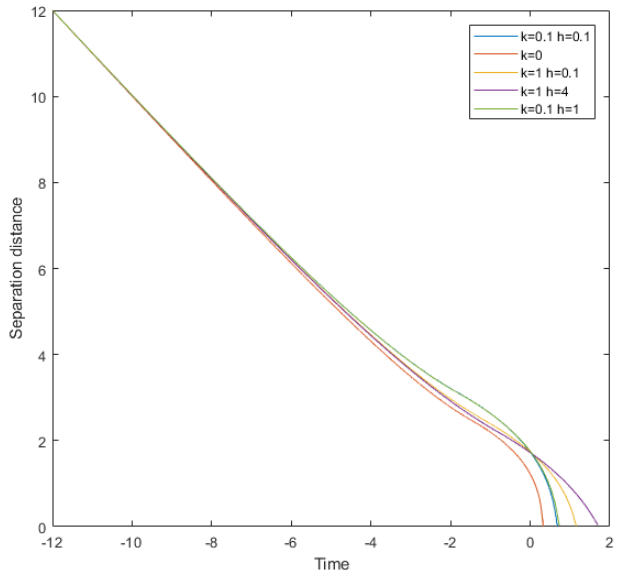

(a) Separation distances as a function of time

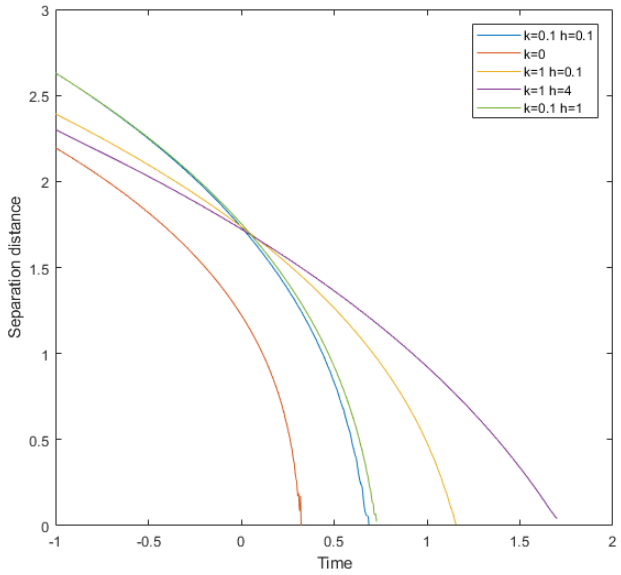

(b) Closer comparison of separation distances near touchdown

Figure 5.6: The separation distances show the acceleration of the droplet into touchdown.

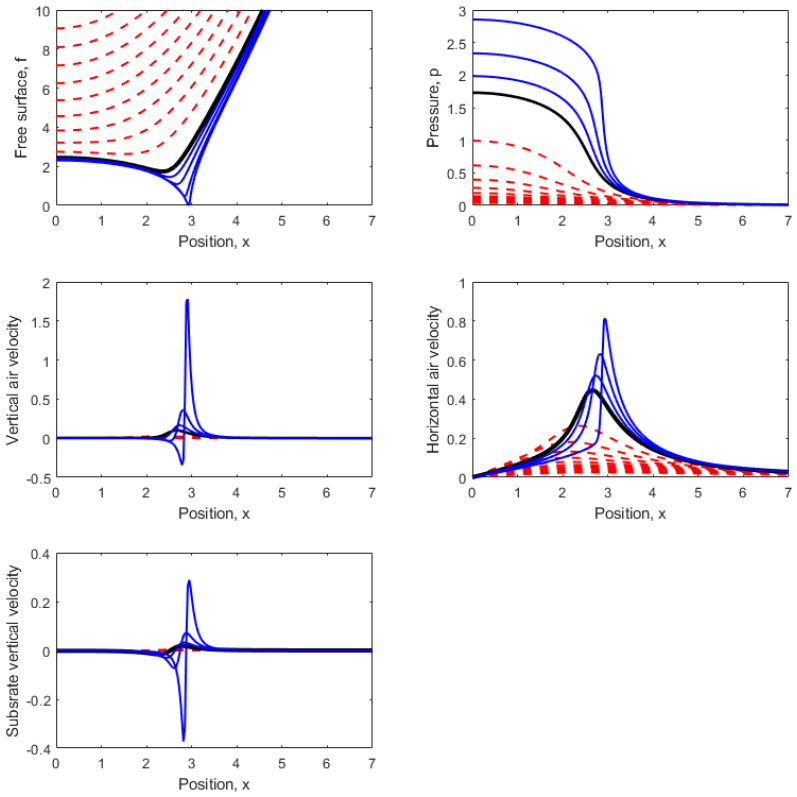

Figure 5.7: Profiles showing free surface shape, pressure, both air velocity components and substrate air velocity at a fixed elevation of $y = 0.1$ for $k = 0.1$ and $H = 0.1$.

horizontal air velocities. However, we have higher vertical velocities at the surface of the substrate. This larger velocity just under the minima of the free surface explains the delay in touchdown time. With $k = 1$ we had a touchdown time of $t = 0.7$ with $k = 1$ we have touchdown time of 1.2. The larger vertical velocity at the surface of the substrate will reduce the acceleration into touchdown the minima has which will delay touchdown.

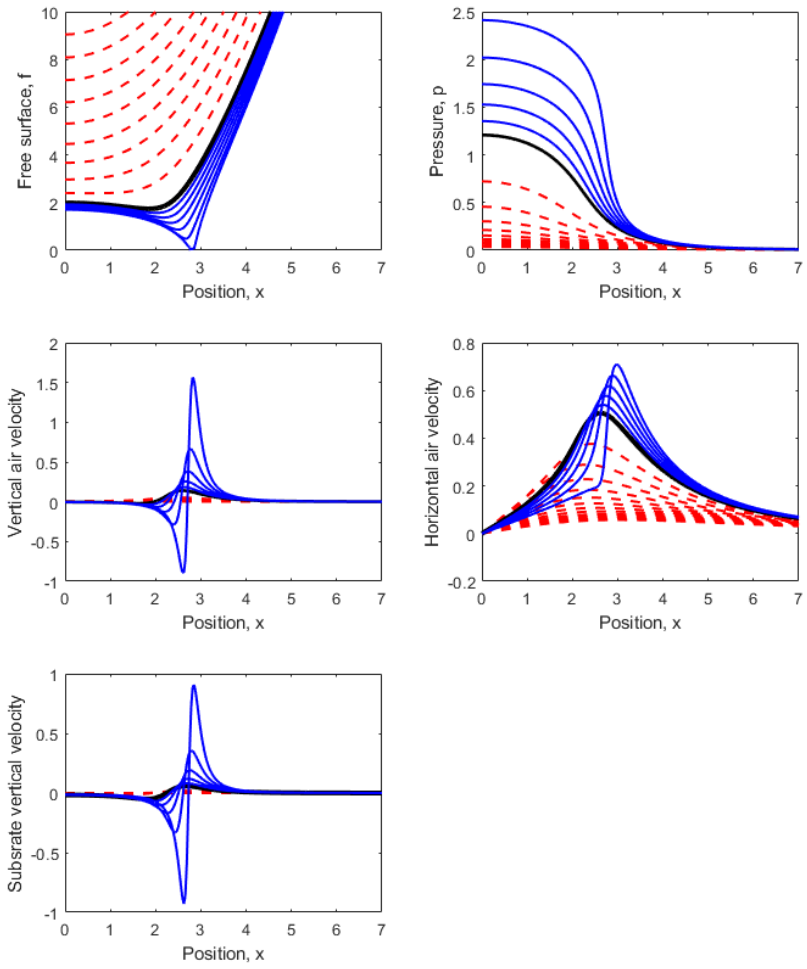

Figure 5.8: Profiles showing free surface shape, pressure, both air velocity components and substrate air velocity at a fixed elevation of $y = 0.1$ for $k = 1$ and $H = 0.1$.

5.5 Infinitely deep porous layer

To investigate the infinitely deep case we can take the limit of $H \to \infty$ in (5.22) to obtain the effect of the substrate on the air. The second integral

tends to zero leaving just the Hilbert transform:

$$v = \frac{k}{\pi} P.V. \int_{-\infty}^{\infty} \frac{p_{a_x}}{x - \hat{x}} dx. \tag{5.33}$$

With this simpler relation we have an explicit relation between the vertical air velocity on the substrate-air interface and the air pressure so we do not have to solve anything in the substrate. The system we have is:

$$F_t = \frac{1}{12} \frac{\partial}{\partial x} \left(\frac{\gamma F^4 + 4k^{\frac{1}{2}} F^3}{\gamma F + k^{\frac{1}{2}}} \frac{\partial p_a}{\partial x} \right) + \frac{k}{\pi} P.V. \int_{-\infty}^{\infty} \frac{p_{a_x}}{x - \hat{x}} dx, \tag{5.34}$$

$$F_{tt} = -p_{a_{xx}}. \tag{5.35}$$

The numerical method used to solve the coupled equations is the same as that used in Chapters 2, 3 and 4, with however, (5.34) being discretized as follows, let:

$$\begin{aligned}
&A(I + \delta x, J) = (F(I, J) + F(I + \delta x, J)) \\
&\times \frac{\gamma \left(F^3(I, J) + F^3(I + \delta x, J) \right) + 4k^{\frac{1}{2}} \left(F^2(I, J) + F^2(I + \delta x, j) \right)}{\gamma (F(I, J) + F(I + \delta x, J)) + 2k^{\frac{1}{2}}}, \\
&B(I - \delta x, J) = (F(I, J) + F(I - \delta x, J)) \\
&\times \frac{\gamma \left(F^3(I, J) + F^3(I - \delta x, J) \right) + 4k^{\frac{1}{2}} \left(F^2(I, J) + F^2(I - \delta x, j) \right)}{\gamma (F(I, J) + F(I - \delta x, J)) + 2k^{\frac{1}{2}}},
\end{aligned}$$

So we have:

$$\begin{aligned}
&\frac{1}{12} F(I, J - 2\delta t) - \frac{2}{3} F(I, J - \delta t) + \frac{2}{3} F(I, J + \delta t) - \frac{1}{12} F(I, J + 2\delta t) \\
&+ k\delta t \mathcal{H} \left(\frac{1}{12} P(I - 2\delta x, J) - \frac{2}{3} P(I - \delta x, J) + \frac{2}{3} P(I + \delta x, J) \right. \\
&\left. - \frac{1}{12} P(I + 2\delta x, J) \right) \\
&= \frac{\delta t}{12(\delta x)^2} \left[\{P(I - \delta x, J) B(I - \delta x, J)\} \right. \\
&- \{P(I, J) \left(B(I - \delta x, J) + A(I + \delta x, J) \right)\} \\
&\left. + \{P(I + \delta x, J) A(I + \delta x, J)\} \right].
\end{aligned} \tag{5.36}$$

This system is solved using the discretisation method described in the previous chapters. We use (3.31) to guess the updated free surface position then use (5.36) to update the pressure. We continue to iterate until we reach convergence in the lubrication equation. There was some numerical difficulty exploring the parameter space for some values of k the code suffered breakdowns before getting as close to touchdown as in the previous cases, the iteration procedure became unstable for the FFT method. Figure 5.9 shows the profiles with an infinite depth layer. We have a lot of similarities between finite depth and infinite depth profiles. Almost all flow into the substrate happens around the touchdown position. The delay in touchdown time is much less than with the finite depth porous layer, here we have the touchdown time around $t = 0.44$. This is likely due to the vertical air jets being less significant and the pressure under the droplet is overall lower allowing for a faster touchdown.

5.6 Conclusions

In this chapter new models for the impact of a shallow water layer onto both a thicker and infinite depth porous layers were given. For the intermediate depth layers we observed that changing the porosity had more effect on the flow than changing the depth of the layer. Surprisingly, we found that there are circumstances in which increasing the porosity can actually further delay the time until touchdown is achieved as the air leaving the substrate interacts with the minima of the incoming free surface. With an infinite depth layer we had faster touchdown for the same value of k. The squeezing of the air layer during the descent of the drop forced air into the substrate. It also displaced some of the substrate air, and exit as narrow vertical jets, one either side of the central bubble.

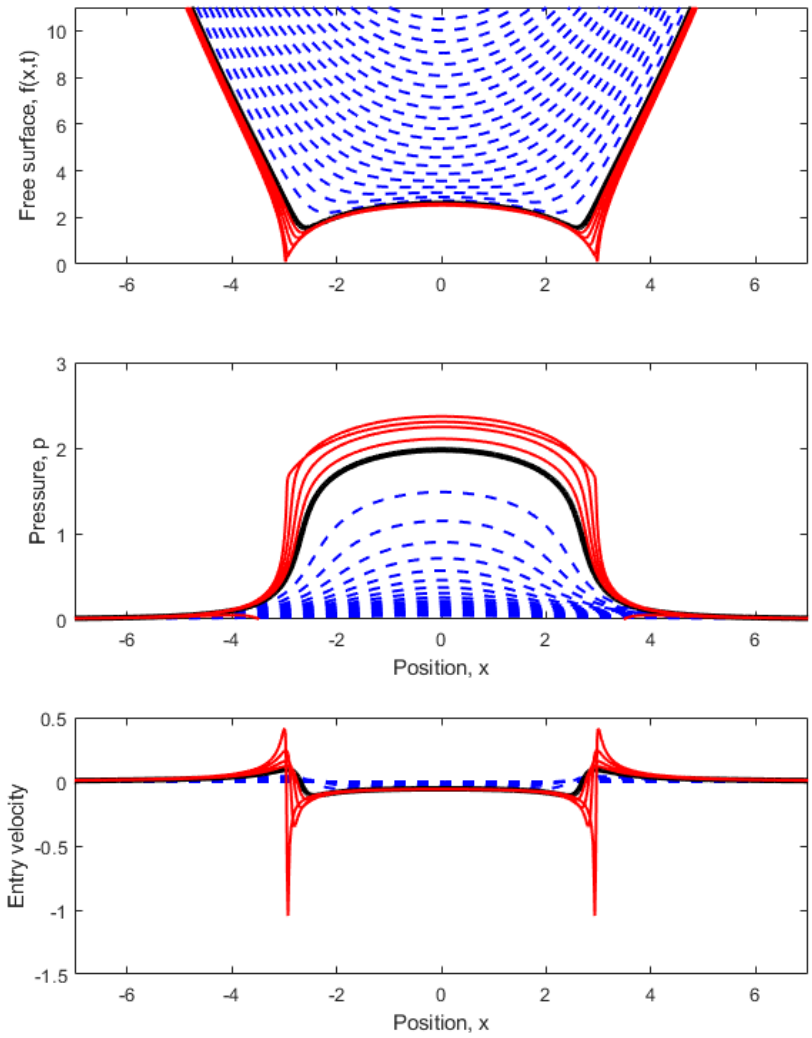

Figure 5.9: Infinite depth profiles for $k = 0.1$ with touchdown time at $t = 0.44$.

6

Post-impact dynamics of an impact with an impermeable substrate

6.1 Literature review

The pre-impact model in the previous work in this thesis breaks down upon contact with the substrate due to obtaining pressures which are tending to infinity as the gap between the droplet and the substrate tends to zero. We need an alternative model for describing the dynamics of post-impact.

Impacts between solids and liquids have been studied a great deal. Early on the dynamics of an alighting seaplane were studied by Von Karman (1929) whose study assumed deep water for the impact of the floats onto the water surface. There was no account of the increased elevation of the waterline due to the water displaced by the descending body. Wagner (1932) had a modified system to that of Von Karman, which accounted for the displaced fluid. Here displaced fluid was accounted for in the description of the edges of the wetted region. Matching the solution in the liquid domain with the expanding size of the plate's wetted region was crucial to solving this problem. At the edges of the wetted region the position of the free surface is matched to the turnover point on the body. This is known as the Wagner condition, and closes the set of model equations. The theory contains some difficulties, owing to a singularity in the predicted pressure at the air-water-body contact point.

Further progress with water-entry problems was made by Wilson (1989) and Howison et al. (1991). These studies looked at impacts of solid bodies into liquids with small deadrise angles, i.e. the tangent of the approaching body's surface is at a small angle to the horizontal undisturbed liquid free-surface. This assumption allowed the problem to be simplified by looking at small times after impact allowing explicit solutions to be calculated. In these papers the models for impact were derived and then solved numerically, to produce plots for the free surface deformations.

Many studies have been reported for droplet impacts with liquid surfaces such as Purvis and Smith (2005), Howison et al. (2005), Hicks and Purvis (2011) and Purvis and Smith (2004a). The evolution of the droplet's free surface is explored analytically for small times with jetting regions forming and peaks in the pressure close to the boundaries of the contact region.

Further analysis into the work of Wagner has been reported in Oliver (2002) and Oliver (2007). Oliver (2002) considers further solid-liquid impacts. Specifically they treat a body hitting a water layer, however, this is equivalent to looking at a droplet impacting the solid by changing the frame of reference. Oliver formally derived the Wagner condition by carefully asymptotically matching the solution in the various regions in the problem (outer, inner and jetting regions). Oliver (2007) extended Wagner theory further by looking at second-order corrections to help resolve the jetting regions.

Some experimental works look closely at jet formation during impacts. Hao et al. (2019) and Zhao et al. (2020) show different examples of jet formation in the early times of an impact, looking at how to suppress a splash. Bartolo et al. (2005) present detailed experimental results for impacts onto both impermeable and more complicated substrates. Using photography, images for the progression of the spreading, jet formation and rebounding are captured at very small time intervals. A study more relevant to perme-

able substrates is Marston et al. (2010): glass beads were used to simulate a permeable powder. Some of the liquid from the droplet impacting this surface was allowed to enter the matrix of voids between spherical glass beads, simulating flow in a porous medium. The impact with these surfaces was found to be comparable to an impact with an hydrophobic surface.

Moore (2014) goes into great detail about various models of droplet impacts, primarily using asymptotic methods for formulating and solving the systems. They have a focus on Wagner theory in the early chapters of his thesis before making additions to this classic model before moving away from this theory. They extend Wagner theory with an oblique impact and formulates and solves this problem numerically. Also they consider the impact problem with air cushioning present and the leading order solution is found. Lastly they look at a systematic way to derive models for the splash jets by taking advantage of small parameters in his model.

Looking more into droplet impacts onto complex substrates we have Negus et al. (2020) who investigate droplet impact onto a plate which is supported by a spring, and thus allowed to move and oscillate. The problem is formulated analytically by looking at the outer and inner regions and matching them together by coupling the droplet impact with a deceleration affect from the spring. Direct numerical simulations are used to verify the results found analytically. Henman et al. (2021) considered droplet impacts onto deformable surfaces such as viscoelastic solids and flexible substrates. The flow in the air layer was coupled to the deformation of the free surfaces of the droplet and the deformation of the substrate. These surfaces results in lower pressures compared to an impact with an impermeable case and more consistent sizes of entrapped bubbles. Impacts onto rough surfaces have been considered in Elliott and Smith (2015). A supercooled droplet impacts a rough surface, which allows ice to form and spread as the droplet is spreading along the surface. Roughness is defined by a smooth peak on

an otherwise flat surface. Different behaviour of the spreading of ice was observed for different values of roughness.

Pegg, Purvis and Korobkin (2018) considered a droplet impact onto an elastic plate. Analytical methods were used to formulate the problem with a different boundary condition to this thesis on the contact region of the droplet with the substrate which was solved numerically.

European study group with industry report, Parker and Nally (2012) covered a similar problem of considering the post-impact dynamics of a droplet impacting a permeable substrate. A simple approximation for the fluid entering the substrate was used here. Diffusion of the liquid was considered for it to spread through the substrate at long times and evaporation was looked into as a means of the volume of fluid to exit the substrate.

In this chapter we will derive the governing equations for the post-impact behaviour for a droplet impacting an impermeable substrate. This is an important step before we extend this model in the following chapter to model impacts more complex substrates.

6.2 Formulation of governing equations

The rest of this chapter is about impact on an impermeable plate, and it contains a mathematical technique which is extended to a porous medium, treated in Chapter 7. We now consider a droplet impact with a flat plate in two dimensions. The starred variables are physical variables and have S.I. units, and we rescale them below. We choose for simplicity a stationary spherical droplet, with radius R, and an approaching flat plate approaching at velocity V, the plate at $y^* = 0$ at the time of initial impact, $t^* = 0$. After impact starts at $t^* = 0$, Wagner Theory is used to describe the impact behaviour. We have the y^* axis increasing vertically into the fluid with $x^* = 0$ being a line of symmetry for the problem. The liquid free-surface is given by $y^* = \eta^*(x^*, t^*)$, we are only interested in the impact region, the

lower half of the droplet. The free surface deforms from the start of impact onwards in time. We will have an interface between the wetted and dry regions of the substrate. We define the point as the turnover point. These points should be symmetric for a plate which only has a vertical velocity component and a symmetric drop. The turnover points on the plate at $x^* = \pm d(t)$ on $y^* = t^*V$ (this form due to the plate moving vertically) in which $d(t)$ grows from $d = 0$ at $t^* = 0$, as time progresses. We expect if the drop is initially stationary then the disturbance of the free surface tends to zero as we pass into the far field.

We are working with an inviscid case due to a high Reynolds number so we can formulate a problem in terms of the velocity potential of the flow, $\phi^*(x^*, y^*, t^*)$. In the derivation below, we keep the substrate boundary condition general to allow easy extension into more complex substrate behaviour (for example porosity). Let $v^*(x^*, y^*, t^*, k^*, p_l^*, p_s^*)$ encapsulate this general behaviour taking into account the substrate, where k^* is the permeability of the substrate and where p_l^* and p_s^* correspond to pressures in the liquid and substrate respectively.

Figure 6.1 shows the basic scales in the problem and the different local regions. First we have the outer problem which considers the shape of the free-surface. At a more local view we have the jet-root region where the free-surface turns over and forms the base of the jet. This leads into the smallest region, the jet region, here we have a very thin jet along the surface of the substrate. Our governing equations are:

$$\nabla^2\phi^*(x^*, y^*, t^*) = 0 \qquad \text{in fluid domain } y^* > \eta^*, \tag{6.1}$$

$$\frac{D}{Dt}(y^* - \eta^*) = 0 \qquad \text{the kinematic condition on } y^* = \eta^*(x^*, t^*), \tag{6.2}$$

$$p^*(x^*, y^*, t^*) = 0 \qquad \text{from zero stress on the free-surface on } y^* = \eta^*, \tag{6.3}$$

$$\frac{\partial\phi^*}{\partial y^*} = v^* \qquad \text{on the plate, } y^* = 0 \text{ and } |x^*| < d(t^*). \tag{6.4}$$

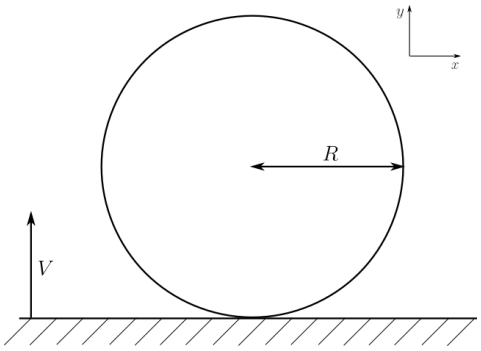

(a) Diagram showing the basic scales in our problem

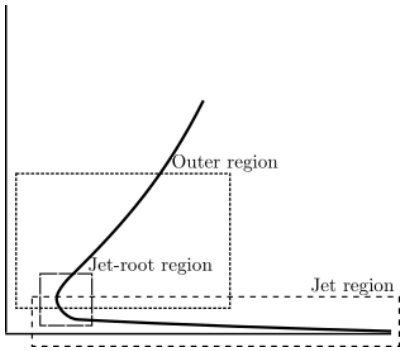

(b) Diagram showing the multiple regions of the problem

Figure 6.1: Diagrams showing the initial situation and the different regions of our problem.

We have an undisturbed circular droplet shape given by:

$$x^{*2} + (y^* - R)^2 = R^2, \tag{6.5}$$

$$y^* = \pm\sqrt{R^2 - x^{*2}} + R = \eta^*(x^*, 0). \tag{6.6}$$

We non-dimensionalise by scaling spatial coordinates with R, taking our velocity scale to be V, this will give an appropriate time scale of $\frac{R}{V}$. The free-surface shape is scaled the same as our spatial coordinates, ρV^2 will give an appropriate pressure scale (where ρ is the constant density of the fluid) and we scale velocity potential as RV. Thus we have:

$$[x^*, y^*, t^*, \phi^*, \eta^*, p^*, V^*] = \left[R\bar{x}, R\bar{y}, \frac{R}{V}\bar{t}, RV\bar{\phi}, R\bar{\eta}, \rho V^2\bar{p}, V\bar{v}\right]. \tag{6.7}$$

Hence our problem becomes:

$$\nabla^2\bar{\phi}(\bar{x},\bar{y},\bar{t}) = 0 \qquad \text{in fluid domain } \bar{y} > \bar{\eta}, \tag{6.8}$$

$$\frac{D}{Dt}(\bar{y}-\bar{\eta}) = 0 \qquad \text{on } \bar{y} = \bar{\eta}(\bar{x},\bar{t}), \tag{6.9}$$

$$\frac{\partial\bar{\phi}}{\partial\bar{y}} = \bar{v} \qquad \text{on plate, } \bar{y} = 0 \text{ and } |\bar{x}| < d(\bar{t}). \tag{6.10}$$

Let us assume we are looking at small times. Let ϵ be a small parameter and we consider times of order ϵ^2. With a plate rising into the droplet the displacement of the turnover points are proportional to $\sqrt{\bar{t}} = O(\epsilon)$ (see Wagner (1932) for more details about this), therefore the horizontal length scale should be $O(\epsilon)$, by the continuity equation the vertical scale will be the same as this. Let us also assume the velocity of the plate is $O(1)$, since we are looking at a small local region we expect the plate velocity to be a lower order of this parameter. From this velocity scale we can use the definition of the velocity potential to say that $\phi = O(\epsilon)$.

As we are only considering a local region close to the plate we use the negative branch of the square root in equation (6.6) and thus after applying the local length scalings we have for the undisturbed free surface position:

$$\epsilon y = -\sqrt{1-\epsilon^2x^2} + 1 \tag{6.11}$$

$$= 1 - (1 - \frac{\epsilon^2}{2}x^2) + O(\epsilon^4) \tag{6.12}$$

$$y = 0 + \epsilon\left(\frac{x^2}{2}\right) + O(\epsilon^3), \tag{6.13}$$

so all conditions applied on the free-surface at leading order can be applied on $y = 0$. We can also conclude that the scale of the free-surface position is $O(\epsilon^2)$.

We have Bernoulli's equation in the fluid domain in physical variables:

$$\frac{p_l^*(x^*,y^*,t^*)}{\rho} + {\phi^*}_{t^*} + \frac{1}{2}\left({\phi^*_{x^*}}^2 + {\phi^*}_{y^*}{}^2\right) = 0, \tag{6.14}$$

and thus to have pressure balance another term in this equation we must

have $\bar{p} = O(\epsilon^{-1})$, so we have

$$p_l(x, y, t) = -\phi_t + O(\epsilon). \tag{6.15}$$

In conclusion we have the local scales as:

$$[\bar{x}, \bar{y}, \bar{t}, \bar{\phi}, \bar{\eta}, \bar{p}] = \left[\epsilon x, \epsilon y, \epsilon^2 t, \epsilon\phi, \epsilon^2\eta, \epsilon^{-1}p\right]. \tag{6.16}$$

Expanding the total derivative in equation (6.2) using (6.7) we have the kinematic condition:

$$\bar{\phi}_{\bar{y}} = \bar{\eta}_{\bar{t}} + \bar{\phi}_{\bar{x}}\bar{\eta}_{\bar{x}}, \tag{6.17}$$

applying the scales in our local region (6.16) we have:

$$\phi_y = \eta_t + \epsilon\phi_x\eta_x, \tag{6.18}$$

which to leading order becomes simply:

$$\phi_y = \eta_t \qquad \text{on } y = 0. \tag{6.19}$$

This is valid on the free-surface, the region outside the wetted area in contact with the plate i.e. $|x| > d(t)$ and $y = 0$.

In the wetted region we have a zero penetration condition:

$$\phi_y = 1, \tag{6.20}$$

valid on $y = 0$ and $|x| < d(t)$. In the far field as $|x| \to \infty$ we expect the droplet to be undisturbed so we have:

$$\eta(x, t) \to \frac{x^2}{2} \qquad \text{as } |x| \to \infty. \tag{6.21}$$

From (6.18) the horizontal velocity component is negligible compared to vertical velocity component on the free surface, we expect to have zero horizontal velocity component on the free-surface of the droplet.

For convenience we define a function $h(x, t)$ which is the perturbation from the initial shape of the droplet, so we have the position of the free surface described in the expression:

$$\eta(x, t) = \frac{x^2}{2} - h(x, t). \tag{6.22}$$

This gives desirable behaviour for $h(x,t)$ as we will have decay as $|x| \to \infty$ which provides mathematical convenience when we come to solve integral equations further on by having $h(x,t) > 0$ and that $h \to 0$ as $|x| \to \infty$.

From Wagner theory, to determine the turnover points we need an equation matching the free-surface position to the position of the plate at the turnover points $x = \pm d(t)$. We have:

$$\eta(d(t),t) - t = \frac{d(t)^2}{2} - h(d(t),t) - t = 0, \tag{6.23}$$

where $y = \eta(d(t),t)$ is our free-surface position and $y = t$ is the position of the plate.

In summary, in our inner region we have the mixed boundary value problem:

$$\nabla^2\phi(x,y,t) = 0 \qquad \text{in droplet } y > 0, \tag{6.24}$$

$$\frac{\partial\phi(x,0,t)}{\partial y} = 1 \qquad \text{on } |x| < d, \tag{6.25}$$

$$\phi(x,0,t) = 0 \qquad \text{on } |x| > d, \tag{6.26}$$

$$\frac{\partial\phi(x,0,t)}{\partial y} = \frac{\partial\eta(x,t)}{\partial t} \qquad \text{on } |x| > d, \tag{6.27}$$

$$\eta(x,t) \to \frac{x^2}{2} \qquad \text{as } |x| \to \infty, \tag{6.28}$$

$$\phi \to 0 \qquad \text{as } y \to \infty, \tag{6.29}$$

$$p(x,0,t) = 0 \qquad \text{on } |x| > d, \tag{6.30}$$

$$\frac{d(t)^2}{2} - h(d(t),t) - t = 0, \tag{6.31}$$

$\phi(x,y,t)$, $\eta(x,t)$ and $d(t)$ are all unknown functions with $\bar{v}$ changing depending on the substrate.

6.3 Solution using complex variable theory

To begin to solve the system (6.24) - (6.31) we can use complex variable theory. The mixed boundary value problem we have for $\phi(x,y,t)$ is harmonic

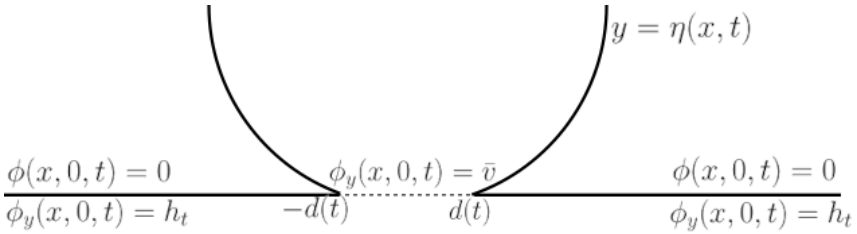

Figure 6.2: Summary of governing equations and regions where the conditions apply, here $\bar{v} = 0$, this is non-zero for a permeable substrate.

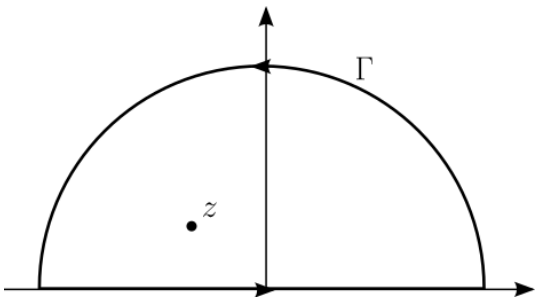

(a) Contour without singularity on the contour

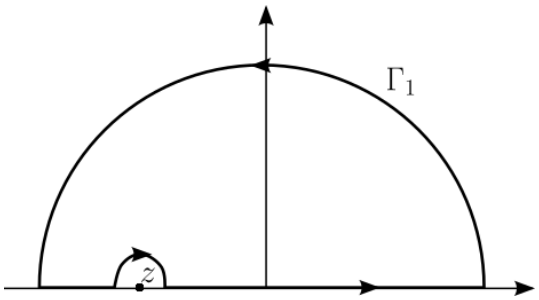

(b) Adjusted contour to account for the singularity on $y = 0$

Figure 6.3: Shapes of the contours in the complex z-plane used for the integration.

and together with the stream function $\psi(x, y, t)$ this pair of functions satisfy the Cauchy-Riemann equations, see Acheson (1990). Let $z = x + iy$, we define a characteristic function:

$$\Delta(z) = \sqrt{z^2 - d^2},$$

which has a useful property of switching between real and imaginary values as we pass from the free surface into the wetted region and back onto the free surface on the other side. We define a complex valued analytic function:

$$w(z,t) = \Delta(z)(\phi(x,y,t) + i\psi(x,y,t)), \tag{6.32}$$

Substituting into Cauchy's integral formula, we have:

$$\phi_x - i\phi_y = \frac{1}{2i\pi\Delta(z)} \oint_\Gamma \frac{\Delta(\gamma)(\phi_\alpha(\alpha,\beta,t) - i\phi_\beta(\alpha,\beta,t))}{\gamma - z} d\gamma, \tag{6.33}$$

with $\gamma = \alpha + i\beta$ and z is inside the simple closed contour Γ which forms a D in the upper half plane, see Figure 6.3(a). In the far field $|\Delta(z)|$ behaves as $|z|$ and $|\phi + i\psi|$ behaves as $\frac{1}{|z^2|}$ or smaller. Therefore, the integrand has modulus $\frac{1}{|z^2|}$, and behaves like $\frac{1}{R}$ in magnitude. It therefore tends to zero as $R \to \infty$. When we integrate around this contour we have a singularity at $\gamma = z$ on the contour on the $y = 0$ axis. To proceed with this we define a new contour Γ_1 which has a semi-circular contour around this singularity, see Figure 6.3(b), this is only necessary if z lies on the the axis. By Jordan's Lemma the contribution of the integral from the large semi-circle is zero thus leaving just a line integral. The factor of $\frac{1}{2}$ is lost due to the contribution from small semi-circle around the singularity.

For $y = 0$ and $\beta = 0$ we have from taking the real part of (6.33) and $|x| < d$:

$$\begin{aligned}\phi_x = \frac{1}{\pi\sqrt{d(t)^2 - x^2}} \Bigg[&\int_d^\infty \frac{\sqrt{\alpha^2 - d(t)^2}\phi_\alpha}{\alpha - x} d\alpha \\ &+ P.V. \int_{-d}^{d} \frac{\sqrt{d(t)^2 - \alpha^2}\phi_\beta}{\alpha - x} d\alpha \\ &+ \int_{-\infty}^{-d} \frac{\sqrt{\alpha^2 - d(t)^2}\phi_\alpha}{\alpha - x} d\alpha \Bigg].\end{aligned} \tag{6.34}$$

However, we have information for the derivatives of ϕ from (6.25)-(6.27) in these regions so we have:

$$\phi_x = \frac{1}{\pi\sqrt{d(t)^2 - x^2}} P.V. \int_{-d}^{d} \bar{v} \frac{\sqrt{d(t)^2 - \alpha^2}}{\alpha - x} d\alpha \qquad \text{for } |x| < d(t). \tag{6.35}$$

For $|x| > d$ we have:

$$\phi_x = \frac{-1}{\pi\sqrt{x^2 - d(t)^2}}\left[P.V.\int_{-\infty}^{-d}\frac{\sqrt{\alpha^2 - d(t)^2}\phi_\beta}{\alpha - x}d\alpha - \int_{-d}^{d}\frac{\sqrt{d(t)^2 - \alpha^2}\phi_\alpha}{\alpha - x}d\alpha + P.V.\int_{-\infty}^{-d}\frac{\sqrt{\alpha^2 - d(t)^2}\phi_\beta}{\alpha - x}d\alpha\right]. \tag{6.36}$$

Similarly from taking the imaginary parts of (6.33), for $|x| > d$ we have:

$$-\phi_y = \frac{1}{\pi\sqrt{x^2 - d(t)^2}}\left[P.V.\int_{d}^{\infty}\frac{\sqrt{\alpha^2 - d(t)^2}\phi_\alpha}{\alpha - x}d\alpha + \int_{-d}^{d}\frac{\sqrt{d(t)^2 - \alpha^2}\bar{v}}{\alpha - x}d\alpha + P.V.\int_{-\infty}^{-d}\frac{\sqrt{\alpha^2 - d(t)^2}\phi_\alpha}{\alpha - x}d\alpha\right], \tag{6.37}$$

in which $\phi_\alpha = 0$ for $|\alpha| > d$ and (6.2) prescribes ϕ_β. So we have:

$$-\phi_y = -\eta_t = h_t = \frac{1}{\pi\sqrt{x^2 - d(t)^2}}\int_{-d}^{d}\frac{V\sqrt{d(t)^2 - \alpha^2}}{\alpha - x}d\alpha. \tag{6.38}$$

Taking the imaginary parts of (6.33), for $|x| < d$ we also have:

$$\phi_y = \frac{-1}{\pi\sqrt{d(t)^2 - x^2}}\left[\int_{d}^{\infty}\frac{\sqrt{\alpha^2 - d(t)^2}\phi_\beta}{\alpha - x}d\alpha - P.V.\int_{-d}^{d}\frac{\sqrt{d(t)^2 - \alpha^2}\phi_\alpha}{\alpha - x}d\alpha + \int_{-\infty}^{-d}\frac{\sqrt{\alpha^2 - d(t)^2}\phi_\beta}{\alpha - x}d\alpha\right] \quad \text{for } |x| < d(t). \tag{6.39}$$

6.3.1 Velocity field in the droplet

To calculate our solution anywhere in the inner region of our droplet we go back to the formulation of the governing equations. We define the characteristic function:

$$\Delta(z) = \sqrt{z^2 - d^2}.$$

We have the same complex-valued analytic function:

$$w(z,t) = \Delta(z)(\phi(x,y,t) + i\psi(x,y,t)). \tag{6.40}$$

Substituting into Cauchy's integral formula we have:

$$\phi_x - i\phi_y = \frac{1}{2i\pi\Delta(z)} \oint_\Gamma \frac{\Delta(\gamma)(\phi_\alpha(\alpha,\beta,t) - i\phi_\beta(\alpha,\beta,t))}{\gamma - z} d\gamma,$$

with $\gamma = \alpha + i\beta$, with $y > 0$ the singularity falls strictly inside of the contour. We define our contour Γ as a half circle in the upper half plane and the real axis. Since we have a stationary droplet the contribution from this arc tends to zero in the limit of the radius R of the semicircle tending to infinity thus for any (x, y) we have:

$$\phi_x - i\phi_y = \frac{1}{2i\pi\Delta(z)} \int_{-\infty}^{\infty} \frac{\Delta(\gamma)(\phi_\alpha(\alpha,0,t) - i\phi_\beta(\alpha,0,t))}{\gamma - z} d\gamma. \tag{6.41}$$

This equation allows us to calculate the velocity at any point in the domain once $\phi(x, t, 0)$ is known.

6.4 Analytic solution for an impermeable base

In order to solve for the free-surface shape equation (6.38) has to be solved. Firstly we consider the impermeable case with $\bar{v} = 1$. To solve this equation we first make a substitution for α and x in order to help remove integrable singularities. Let $\alpha = d\sin(\theta)$ and $x = d \cdot a$ with $-\pi/2 < \theta < \pi/2$ and $a > 1$. So we have:

$$\int_{-d}^{d} \frac{\sqrt{d(t)^2 - \alpha^2}}{\alpha - x} d\alpha = \int_{-\frac{\pi}{2}}^{\frac{\pi}{2}} \frac{d\cos(\theta)}{d\sin(\theta) - d \cdot a} d\cos(\theta) d\theta \tag{6.42}$$

$$= d \int_{-\frac{\pi}{2}}^{\frac{\pi}{2}} \frac{\cos^2(\theta)}{\sin(\theta) - a} d\theta \tag{6.43}$$

$$= \frac{d}{2} \int_{-\pi}^{\pi} \frac{\cos^2(\theta)}{\sin(\theta) - a} d\theta. \tag{6.44}$$

To remove the trigonometric functions we define a complex variable $z = e^{i\theta}$ so that $dz = ie^{i\theta}d\theta$ and $d\theta = \frac{dz}{iz}$, this also changes our domain we are

integrating over to a contour which is the unit circle. Let:

$$I = \int_{-\pi}^{\pi} \frac{\cos^2(\theta)}{\sin(\theta) - a} d\theta. \tag{6.45}$$

Thus we have:

$$\begin{aligned} I &= \int_c \frac{\left(\frac{z+z^{-1}}{2}\right)^2}{\left(\frac{z-z^{-1}}{2i}\right) - a} \frac{dz}{iz} \\ &= \frac{1}{4} \int_c \frac{\left(z + z^{-1}\right)^2}{\frac{z^2}{2} - \frac{1}{2} + aiz} dz, \end{aligned} \tag{6.46}$$

where c is the unit circle at centre 0. The denominator has roots at $z_\pm = ai \pm \sqrt{1-a^2}$. Since $a > 1$, z_- lies inside the circle and z_+ lies outside, and the integrand has a double pole at $z = 0$. Thus by using Cauchy's Residue Theorem we simply need to calculate the residues these poles. The pole at $z = z_+$ has residue:

$$\begin{aligned} R_1 &= \lim_{z \to z_-} \left((z - z_-) \frac{\left(z + z^{-1}\right)^2}{\frac{z^2}{2} - \frac{1}{2} + aiz} \right) \\ R_1 &= 2(z_- - z_+) = -4\sqrt{1-a^2}. \end{aligned} \tag{6.47}$$

For the pole at the origin we need to express the integrand as a Laurent series about $z = 0$ to find the coefficient of z^{-1}, we have:

$$\frac{\left(z + z^{-1}\right)^2}{\frac{z^2}{2} - \frac{1}{2} + aiz} = \frac{\left(z + z^{-1}\right)^2}{\frac{1}{2}(z - z_-)(z - z_+)} \tag{6.48}$$

$$= \frac{2(z^2 + 2 + z^{-2})}{z_- z_+} \left(\frac{1}{1 - \frac{z}{z_-}} \right) \left(\frac{1}{1 - \frac{z}{z_+}} \right) \tag{6.49}$$

$$= \frac{2(z^2 + 2 + z^{-2})}{z_- z_+} \left(1 + \frac{z}{z_-} + o(z^2) \right) \left(1 + \frac{z}{z_+} + o(z^2) \right). \tag{6.50}$$

So we have the residue given by:

$$\begin{aligned} R_0 &= \frac{2}{z_- z_+} \left(\frac{1}{z_-} + \frac{1}{z_+} \right) \\ R_0 &= \frac{2}{z_- z_+} \frac{(z_- + z_+)}{z_- z_+} = 4ai. \end{aligned} \tag{6.51}$$

Thus:

$$I = -2\pi\sqrt{a^2 - 1} + 2\pi a. \tag{6.52}$$

So we have (6.42)

$$\int_{-d}^{d} \frac{\sqrt{d(t)^2 - \alpha^2}}{\alpha - x} d\alpha = -\pi\sqrt{x^2 - d^2} + \pi x, \tag{6.53}$$

hence:

$$h_t = -1 + \frac{x}{\sqrt{x^2 - d^2}}, \tag{6.54}$$

and

$$h(x,t) = -t + \int_0^t \frac{x}{\sqrt{x^2 - d(\tau)^2}} d\tau + h(x,0), \tag{6.55}$$

$$= -t + \int_0^t \frac{x}{\sqrt{x^2 - d(\tau)^2}} d\tau, \tag{6.56}$$

as the initial droplet is undisturbed. From the Wagner condition (6.31) we have:

$$\frac{d^2}{2} - h(d(t),t) - t = 0 \tag{6.57}$$

$$\Rightarrow \frac{d^2}{2} = \int_0^t \frac{d(t)}{\sqrt{d(t)^2 - d(\tau)^2}} d\tau. \tag{6.58}$$

Upon substitution of $d(t) = 2\sqrt{t}$ we can see that this is indeed a solution to (6.58), see Oliver (2002). With this known the free-surface shape can be solved for. From (6.56)

$$h(x,t) = -t + \int_0^t \frac{|x|}{\sqrt{x^2 - d(\tau)^2}} d\tau \tag{6.59}$$

$$= -t - \frac{|x|}{2}\sqrt{x^2 - 4t} + \frac{x^2}{2}. \tag{6.60}$$

This gives the free-surface shape as:

$$\eta(x,t) = \frac{x^2}{2} - h(x,t) = t + \frac{|x|}{2}\sqrt{x^2 - 4t}. \tag{6.61}$$

We can also evaluate (6.35) to obtain the velocity potential. To solve we progress in a similar way to before, let $\alpha = d\sin(\theta)$ with $-\pi/2 < \theta < \pi/2$:

$$I = P.V. \int_{-d}^{d} \frac{\sqrt{d(t)^2 - \alpha^2}}{\alpha - x} d\alpha \tag{6.62}$$

$$= d^2 P.V. \int_{-\frac{\pi}{2}}^{\frac{\pi}{2}} \frac{\cos^2(\theta)}{d\sin(\theta) - x} d\theta. \tag{6.63}$$

Let $\Theta = \pi - \theta$, then:

$$I = d^2 P.V. \int_{\frac{3\pi}{2}}^{\frac{\pi}{2}} \frac{\cos^2(\Theta)}{d\sin(\Theta) - x} (-1) d\Theta \tag{6.64}$$

$$= d^2 P.V. \int_{\frac{\pi}{2}}^{\frac{3\pi}{2}} \frac{\cos^2(\Theta)}{d\sin(\Theta) - x} d\Theta, \tag{6.65}$$

upon adding (6.63) and (6.64) together we have:

$$2I = d^2 P.V. \int_{-\frac{\pi}{2}}^{\frac{3\pi}{2}} \frac{\cos^2(\theta)}{d\sin(\theta) - x} d\theta. \tag{6.66}$$

Define c as the unit circle in the complex z plane described anticlockwise. Therefore let $z = e^{i\theta}$ so that $dz = ie^{i\theta} d\theta$ and $d\theta = \frac{dz}{iz}$ so we have:

$$2I = d^2 P.V. \int_c \frac{\frac{1}{4}\left(z + z^{-1}\right)^2}{\frac{d}{2i}\left(z - z^{-1}\right) - x} \frac{1}{iz} dz \tag{6.67}$$

$$= \frac{d}{4} P.V. \int_c \frac{z^2 + 2 + z^{-2}}{\frac{z^2}{2} - \frac{ixz}{d} - \frac{1}{2}} dz \tag{6.68}$$

$$= \frac{d}{2} P.V. \int_c \frac{z^4 + 2z^2 + 1}{z^2(z^2 - \frac{2ixz}{d} - 1)} dz \tag{6.69}$$

$$\frac{4I}{d} = P.V. \int_c 1 + \frac{2ix}{zd} + \frac{4\left(1 - \frac{x^2}{d^2}\right)}{z^2 - \frac{2ixz}{d} - 1} - \frac{1}{z^2} dz. \tag{6.70}$$

In the third term in the integrand in (6.70) using the quadratic formula we can see that both poles lie on the unit circle, c, so we have:

$$z_{1,2} = \frac{ix}{d} \pm \left(1 - \frac{x^2}{d^2}\right)^{\frac{1}{2}}. \tag{6.71}$$

We now redefine our contour of integration with indentations of semicircles around $z_{1,2}$. We shall call these c_1 and c_2. So we have our new contour,

$c' = c \cup c_1 \cup c_2$. Considering the third term in (6.70) the numerator has no z dependence and by Cauchy's Theorem we have:

$$\int_{c'} \frac{1}{z^2 - \frac{2ixz}{d} - 1} dz = 0$$

$$0 = P.V. \int_c \frac{dz}{(z - z_1)(z - z_2)} + \int_{c_1 \cup c_2} \frac{dz}{(z - z_1)(z - z_2)}, \tag{6.72}$$

with:

$$P.V. \int_c \frac{dz}{(z - z_1)(z - z_2)} = \frac{-1}{z_1 - z_2} \int_{c_1 \cup c_2} \frac{1}{(z - z_1)} - \frac{1}{z - z_2} dz \tag{6.73}$$

$$P.V. \int_c \frac{dz}{(z - z_1)(z - z_2)} = \frac{-1}{z_1 - z_2} \left(-\pi i - (-\pi i)\right) = 0, \tag{6.74}$$

in the limit of the radius of the indentations tending to 0. So the only term that does not integrate to 0 in (6.70) is $\frac{2ix}{zd}$ which has a simple pole at the origin. Thus we have:

$$\frac{4I}{d} = P.V. \int_c \frac{2ix}{zd} dz = 2\pi i \frac{2ix}{d} \tag{6.75}$$

$$I = -\pi x. \tag{6.76}$$

From (6.35) we have:

$$\phi_x(x, 0, t) = \frac{-x}{\sqrt{d(t)^2 - x^2}}, \tag{6.77}$$

$$\phi(x, 0, t) = \sqrt{d(t)^2 - x^2}. \tag{6.78}$$

6.5 Conclusions

In this chapter we formulated and solved analytically the post-impact flow of a droplet on an impermeable substrate. Wagner theory was used to close the problem and complex variable theory was used to solve the system of equations to provide exact functions for the free surface, pressure, velocity potential and the function that governs how quickly the droplet spreads, $d(t)$. The results in this chapter are going to be used in the following chapter when we have a porous substrate instead of an impermeable substrate.

7

Post-impact dynamics onto a porous base

7.1 Formulation and solution with a porous base

To incorporate porosity into the post-impact equations we look back at the function $\bar{v}$ introduced in Chapter 6. The objective is to define $\bar{v}$ in such a way that it incorporates the behaviour of the substrate and how the fluid in contact with the substrate reacts. The analytic solutions for the various functions for an impermeable impact from the previous chapter are:

$$\phi_I(x,d) = \sqrt{d^2 - x^2}, \tag{7.1}$$

$$\phi_I(x,d)_x = \frac{-x}{\sqrt{d^2 - x^2}}, \tag{7.2}$$

$$\phi_I(x,d)_t = \frac{2}{\sqrt{d^2 - x^2}}, \tag{7.3}$$

$$h_I(x,d)_t = -1 + \frac{x}{\sqrt{x^2 - d^2}}, \tag{7.4}$$

$$h_I(x,d) = -t - \frac{x}{2}\sqrt{x^2 - d^2} + \frac{x^2}{2}, \tag{7.5}$$

$$d_I(t) = 2\sqrt{t}. \tag{7.6}$$

The subscript I refers to impermeable quantities and below we use subscript p to refer to the porous correction.

We begin by considering simplified model for the contribution to ϕ_y on the boundary between the droplet and the porous layer, the full problem

will be discussed in Chapter 8. At the top of the substrate, let us assume that:

$$\phi_y = 1 + kd\phi_t, \tag{7.7}$$

here we are assuming we have a particular amount of fluid entering the substrate which is proportional to the pressure ($-\phi_t$ from Bernoulli's equation (6.15)), the porosity (k) and the size of the wetted region (d). We are extending the substrate condition used in Parker and Nally (2012) where a constant pressure was assumed across this interface. We have (7.7) as an approximation for any k, however we are going to consider a small porosity, $k \ll 1$.

Expanding our functions in powers of the small-valued parameter k we assume a regular asymptotic expansion in powers of the small parameter k, for each of the three unknowns functions in the model:

$$\phi(x, y, t) = \phi_I(x, t) + k\phi_p(x, y, t) + O(k^2), \tag{7.8}$$

$$d(t) = (2 + ka)\sqrt{t}, \tag{7.9}$$

$$h(x, t) = h_I(x, t) + kh_p(x, t) + O(k^2), \tag{7.10}$$

where a can be a function of t. However, for this analysis we will only consider the simplest case, when a is a constant. Substituting these into our governing equation (6.38) we have:

$$\begin{aligned} h_t &= \frac{1}{\pi\sqrt{x^2 - d(t)^2}} \int_{-d}^{d} \frac{\sqrt{d(t)^2 - \alpha^2}(1 + kd\phi(\alpha, t)_t)}{\alpha - x} d\alpha \\ &= \frac{1}{\pi\sqrt{x^2 - d(t)^2}} \int_{-d}^{d} \frac{\sqrt{d(t)^2 - \alpha^2}(1 + kd\phi_I(\alpha, t)_t)}{\alpha - x} d\alpha + O(k^2) \\ &= \frac{1}{\pi\sqrt{x^2 - d(t)^2}} \left(\int_{-d}^{d} \frac{kd\sqrt{d(t)^2 - \alpha^2}\phi_I(\alpha, t)_t}{\alpha - x} d\alpha \right. \\ &\quad \left. + \int_{-d}^{d} \frac{\sqrt{d(t)^2 - \alpha^2}}{\alpha - x} d\alpha \right) + O(k^2). \end{aligned} \tag{7.11}$$

We now begin to evaluate the integrals in equation (7.11). The second integral is identical to the one solved for the impermeable case, thus we have

the second integral for all $x : |x| > d$ given by:

$$\frac{1}{\pi\sqrt{x^2 - d(t)^2}} \int_{-d}^{d} \frac{\sqrt{d(t)^2 - \alpha^2}}{\alpha - x} d\alpha = -1 + \frac{x}{\sqrt{x^2 - d^2}}. \tag{7.12}$$

We also have:

$$\frac{kd(2+ka)^2}{2\pi\sqrt{x^2 - d(t)^2}} \int_{-d}^{d} \frac{\sqrt{d(t)^2 - \alpha^2}}{\sqrt{d(t)^2 - \alpha^2}(\alpha - x)} d\alpha = \frac{k(2+ka)^2}{2\pi\sqrt{x^2 - d(t)^2}} \int_{-d}^{d} \frac{1}{\alpha - x} d\alpha \tag{7.13}$$

$$= \frac{kd(2+ka)^2}{2\pi\sqrt{x^2 - d^2}} \log\left(\frac{x-d}{x+d}\right), \tag{7.14}$$

which is valid for $|x| > d$. Thus we have the solution to (7.11) given by:

$$h_t = -1 + \frac{x}{\sqrt{x^2 - d^2}} + \frac{kd(2+ka)^2}{2\pi\sqrt{x^2 - d^2}} \log\left(\frac{x-d}{x+d}\right) + O(k^2). \tag{7.15}$$

To obtain $h(x,t)$ we now want to integrate with respect to t, we will proceed by doing an integral with respect to d, we rearrange (7.9):

$$t = \frac{d^2}{(2+ka)^2}, \tag{7.16}$$

we have $dt = \frac{2d}{(2+ka)^2}\mathrm{d}d$. Our limits of integration are 0 to t before the change of variables and after the change we have from 0 to d. This upper limit is due to the integral ranging from the start of the impact ($t = d = 0$) to the current time, t, while our d integral ranges how far the liquid has spread horizontally. Thus we have:

$$h(x,t) = -t - \frac{2x\sqrt{x^2 - d^2}}{(2+ka)^2} + \frac{k}{\pi} \int_0^d \frac{d'^2}{\sqrt{x^2 - d'^2}} \log\left(\frac{x-d'}{x+d'}\right) dd' + h(x,0) \tag{7.17}$$

$$= -t - \frac{2x\sqrt{x^2 - d^2}}{(2+ka)^2} + \frac{k}{\pi} \int_0^d \frac{d'^2}{\sqrt{x^2 - d'^2}} \log\left(\frac{x-d'}{x+d'}\right) dd' + \frac{2x^2}{(2+ka)^2}. \tag{7.18}$$

We now focus on the integral in (7.18), to transform this integral into something we can simplify using integration by parts let $d = Sx$, $f(S) =$

$(1-S^2)^{\frac{1}{2}}\log\left(\frac{1-S}{1+S}\right)$ and $G(S)=\log\left(\frac{1-S}{1+S}\right)$ so we have:

$$\begin{aligned} J &= \int_0^d \frac{d'^2}{\sqrt{x^2-d'^2}}\log\left(\frac{x-d'}{x+d'}\right)dd' \\ &= \int_0^{\frac{d}{x}} \frac{x^2S^2}{\sqrt{1-S^2}}G(S)dS \qquad (7.19) \\ &= x^2\left([-Sf(S)]_0^{\frac{d}{x}} - \int_0^{\frac{d}{x}} -(1-S^2)^{\frac{1}{2}}\left(G(S)-\frac{S}{1-S}-\frac{S}{1+S}\right)dS\right) \\ \frac{J}{x^2} &= -\left(1-\frac{d^2}{x^2}\right)^{\frac{1}{2}}\frac{d}{x}\log\left(\frac{x-d}{x+d}\right)+\int_0^{\frac{d}{x}} f(S)-(1-S^2)^{\frac{1}{2}}\frac{2S}{1-S^2}dS \qquad (7.20) \end{aligned}$$

$$\begin{aligned} J &= -d(x^2-d^2)^{\frac{1}{2}}\log\left(\frac{x-d}{x+d}\right)+x^2\left[2(1-S^2)^{\frac{1}{2}}\right]_0^{\frac{d}{x}} - x^2\int_0^{\frac{d}{x}} f(S)dS \\ &= -d(x^2-d^2)^{\frac{1}{2}}\log\left(\frac{x-d}{x+d}\right)+x^2\left(1-\frac{d^2}{x^2}\right)^{\frac{1}{2}} - 2x^2 - x^2\int_0^{\frac{d}{x}} f(S)dS. \qquad (7.21) \end{aligned}$$

At $t=0$ we have $d=0$ and from the above we can see $J=0$ which is the desired behaviour. As $x\to\infty$ $J\to 0$ which is also what we would expect, we can see as x increases the log term vanishes and the limits of the integration tend to zero. Thus J has both the desired properties. We can now substitute (7.21) into (7.18) and evaluate at $x=d$ to apply the Wagner condition:

$$\frac{d^2}{2}-t=h(d,t), \qquad (7.22)$$

to determine our unknown, a. We have:

$$h(d,t)=-t+\frac{2d^2}{(2+ka)^2}-\frac{d^2k}{\pi}\left(2-\int_0^1 f(S)ds\right)+O(k^2). \qquad (7.23)$$

We can use the trapezium rule and evaluate this integral numerically, we find that $\int_0^1 f(S)ds=-0.832$ to three significant digits, let $c=-0.832$ for simplicity, we can now evaluate a. Substituting into the Wagner condition

we have:

$$\frac{d^2}{2} - t = -t + \frac{2d^2}{(2+ka)^2} - \frac{d^2 k}{\pi}(2-c) + O(k^2) \tag{7.24}$$

$$\frac{(2+ka)^2}{2} = 2 - \frac{k}{\pi}(2-c)(2+ka)^2 + O(k^2) \tag{7.25}$$

$$\frac{4+4ka}{2} = 2 - \frac{k}{\pi}(2-c)(4) + O(k^2) \tag{7.26}$$

$$a \approx -\frac{2}{\pi}(2-c) = -1.803. \tag{7.27}$$

Since a is negative, the porous contact region is smaller and spreads more slowly than for the impermeable substrate. This is intuitive since the fluid can enter the substrate which will reduce the spreading across the surface, and we can appeal to the conservation of mass, with an incompressible fluid to support this. With our new d we can write down our free-surface position for a given small k:

$$\begin{aligned}\eta(x,t) = &\frac{d^2}{2} - t \\ &+ t - \frac{2x\sqrt{x^2-d^2}}{(2+ka)^2} - \frac{2x^2}{(2+ka)^2} \\ &- \frac{k}{\pi}\left(-d(x^2-d^2)^{\frac{1}{2}}\log\left(\frac{x-d}{x+d}\right) + x^2\left(1-\frac{d^2}{x^2}\right)^{\frac{1}{2}}\right. \\ &\qquad \left. -2x^2 - x^2\int_0^{\frac{d}{x}} f(S)dS\right),\end{aligned} \tag{7.28}$$

in which:

$$d(t) = (2 - 1.803k)\sqrt{t}, \tag{7.29}$$

$$f(S) = (1-S^2)^{\frac{1}{2}}\log\left(\frac{1-S}{1+S}\right). \tag{7.30}$$

7.2 Computational results

Figure 7.1 shows the comparison between a droplet impact with and without porosity. It is clear from the figure that the free-surface is less deformed in the porous case which is what would be expected since fluid enters the

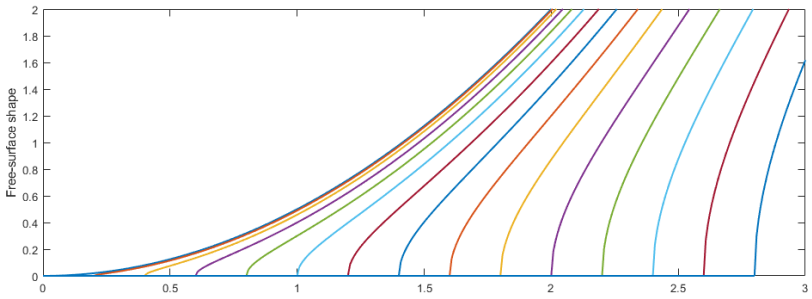

(a) Impermeable solution

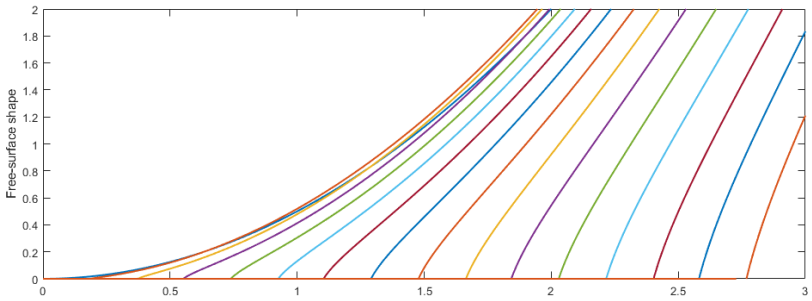

(b) $k = 0.1$ solution

Figure 7.1: Comparison between the impermeable solution and a solution with porosity, each pair of the same-coloured curves occurs at the same time

substrate reducing the spread. We can see a reduced size of the wetted region which can be seen in the figure as this point is the intersection with the x-axis. Figure 7.2 shows a comparison between the two solutions with different values of the porosity. As we can see when we further lower the porosity we recover the same shape of the free surface as for the impermeable plate. The lower panels in Figure 7.2 show the difference between the porous solution and the impermeable solution. At like times, the wetted region is smaller with an impact with a porous substrate than with an impermeable substrate. A comparison is possible provided an allowance is made for the two differing values of d, at any given instant t. There is a region between the two d values in which the region is only wetted in the impermeable

solution. This is more evident for the larger porosity solution, we can see a smooth curve leading to a sharp minimum then another smooth curve which tends to 0 as $x \to \infty$. Figure 7.3 has most of the time steps removed to show more clearly how, as time proceeds, the difference in the boundary of the wetted region becomes much larger.

7.3 Evaluation of the velocity components

We have from (6.35) and (7.7)

$$\begin{aligned}\phi_x &= \frac{1}{\pi\sqrt{d(t)^2-x^2}} P.V. \int_{-d}^{d} \frac{\sqrt{d(t)^2-\alpha^2}(1+kd\phi(\alpha,t)_t)}{\alpha-x} d\alpha \\ &= \frac{1}{\pi\sqrt{d(t)^2-x^2}} \left(\frac{kd(2+ka)^2}{2} PV \int_{-d}^{d} \frac{1}{\alpha-x} d\alpha \right. \\ &\quad \left. + PV \int_{-d}^{d} \frac{\sqrt{d(t)^2-\alpha^2}}{\alpha-x} d\alpha \right). \end{aligned} \tag{7.31}$$

We have a solution to the second principal value integral in terms of d, see (7.2). The first integral we can calculate directly:

$$\phi_x = \frac{-x}{\sqrt{d^2-x^2}} + \frac{kd(2+ka)^2}{2\pi\sqrt{d^2-x^2}} \log\left(\frac{d-x}{d+x}\right). \tag{7.32}$$

We now integrate with respect to x between x and d, we have a boundary condition $\phi(d,t)=0$ needed to integrate this, we have:

$$-\phi(x,t) = -\sqrt{d^2-x^2} + \frac{kd(2+ka)^2}{2\pi} \int_x^d (d^2-x'^2)^{-\frac{1}{2}} \log\left(\frac{d-x'}{d+x'}\right) dx'. \tag{7.33}$$

To simplify this integral we can make a substitution of $x' = d\cos(\theta)$ to simplify the integrand, then we have:

$$\begin{aligned}-\phi(x,t) &= -\sqrt{d^2-x^2} - \frac{kd(2+ka)^2}{2\pi} \int_{\arccos\left(\frac{x}{d}\right)}^{0} \log\left(\left|\frac{\cos(\theta)-1}{\cos(\theta)+1}\right|\right) d\theta \\ &= -\sqrt{d^2-x^2} - \frac{kd(2+ka)^2}{2\pi} \int_{\arccos\left(\frac{x}{d}\right)}^{0} \log\left(\tan^2\left(\frac{\theta}{2}\right)\right) d\theta. \end{aligned} \tag{7.34}$$

We can find an approximation of the integrand using Maple, let:

$$I = \int_{\arccos\left(\frac{x}{d}\right)}^{0} \log\left(\tan^2\left(\frac{\theta}{2}\right)\right) d\theta$$
$$= 2\int_{\arccos\left(\frac{x}{d}\right)}^{0} \log\left(\tan\left(\frac{\theta}{2}\right)\right) d\theta, \tag{7.35}$$

Maple approximates this integrand, which is valid for $0 < \theta < \pi$ to within a relative error of less then 1%, as:

$$\log\left(\left|\tan\left(\frac{\theta}{2}\right)\right|\right) \approx \log\left(\pi^2\left(1 - C^2\theta^2\right)\right) + \log|\theta| - \log(\pi - \theta) - \log(\pi + \theta), \tag{7.36}$$

with $C = 0.1341187916$ and the coefficient of the $O(\theta^4)$ term being negligible. We can now integrate (7.35) by using standard methods.

Figure 7.4 shows a Maple plot of the solution for $I(\theta)$ for a wide range of θ values. The important part of this plot is that at the origin (where $x = d$) we have $I = 0$, due to the range of x we are considering we are only interested in $0 < \theta < \frac{\pi}{2}$.

Figure 7.5 shows a comparison for ϕ between the current analytically derived impermeable solution and the porous solution (here the dashed line is the porous solution). We see that the magnitude of the velocity potential is much lower than for the impermeable case. Figure 7.6 shows how varying the porosity affects the shape of the free surface. The slopes of the free surface at the plate are strongly affected by porosity: when the plate is impermeable the free surface is orthogonal to the plate; for porous plates the free surface meets the plate at an acute angle. For extremely large porosities the model appears to break down (see the yellow line). Figure 7.7 shows a direct comparison between the approximation of the integral (7.35) using a series approximation for the integrand and a direct numerical integration method. As shown, the difference is very small so going forward the series approximation will be used for the benefit of faster computation time. With

$\phi(x, 0, t)$ known calculating the pressure comes from Bernoulli's equation. Figure 7.8 shows this result. We can see we have singularities at the end point of the wetted region, although the peak seems to decrease as time gets larger this is just a facet of the numerical truncation of the numerics, there is indeed a singularity at the turnover point. With the pressure known we can then find the fluid lost into the substrate. Figure 7.9 shows the instantaneous rate of flow of fluid into the substrate. As expected, as time increases the quantity of fluid that enters the substrate increases. An integral of this will show the cumulative fluid that has entered the substrate. Figure 7.10 shows a comparison between two different methods in calculating the fluid lost into the substrate, red circles indicate the value of the fluid lost calculated by integrating the flux of the fluid entering the substrate over length of the wetted region. The blue circles show a direct comparison in free surface shapes between the porous and impermeable models for matching times, the fluid lost here is calculated by integrating to find the area the droplet occupies and finding the difference between these values. We have very good agreement between these two methods.

7.4 Jet region

The dynamics of the jet can help show some further effects of the influence of porosity on the flow. The jet-root region removes the singular properties of the solution found using Wagner theory. Our solution has a singularity at the turnover point, d, this is not physically possible so we look at a smaller region centred on this point to resolve the singularity.

We consider a local region around the contact point $d(t)$, this region is two orders of magnitude smaller than the previously considered problem.

We scale our variables as:

$$x = d(t) + \epsilon^2 x_j, \tag{7.37}$$

$$y = \epsilon^2 y_j, \tag{7.38}$$

$$t = t_j, \tag{7.39}$$

$$\phi = \epsilon^n \left(\phi_j + \dot{d} x_j\right), \tag{7.40}$$

$$\eta = \eta_j, \tag{7.41}$$

where n is to be determined, the subscript j refers to jet variables. We consider the solution for the velocity potential (7.34) and we substitute our new scaled variables into this equation to obtain the matching condition, which will also be the far field condition in this smaller region. This will also provide n. First we will show that the integral in (7.34) will never be at leading order for $k < \frac{\epsilon}{\log(\epsilon)}$ or smaller. We do this to show the leading order for small k the affect of porosity on the jet formed.

The lower limit in (7.34) is $\arccos\left(\frac{x}{d}\right)$, let $\frac{x}{d} = 1 + \epsilon^2 x_j$ and $s = -\epsilon^2 x_j$ then we have $\arccos(1-s) \approx \sqrt{2s}$, let $S = \sqrt{2s}$ as the limit in the integral:

$$\begin{aligned} &\int_{\arccos\left(\frac{x}{d}\right)}^{0} \log\left(\tan^2\left(\frac{\theta}{2}\right)\right) d\theta \\ =&\int_{S}^{0} \log\left(\left|\frac{\cos(\theta)-1}{\cos(\theta)+1}\right|\right) d\theta. \end{aligned} \tag{7.42}$$

Since θ is very small over the integration range, we can approximate using a Maclaurin series $\cos(\theta) = 1 - \frac{\theta^2}{2}$, thus we have:

$$\begin{aligned} &\int_{S}^{0} \log\left(\left|\frac{\cos(\theta)-1}{\cos(\theta)+1}\right|\right) d\theta \\ =&\int_{S}^{0} \log\left(\frac{\theta^2}{4+\theta^2}\right) d\theta \\ \approx&\int_{S}^{0} \log\left(\frac{\theta^2}{4}\right) d\theta \end{aligned} \tag{7.43}$$

$$=2S\log(S) - 2S - 2S\log(2). \tag{7.44}$$

We have neglected the θ^2 in the denominator in (7.43) as it is very small compared to 4. In (7.44) $2S\log(S)$ is non-singular, and is the dominant term as $S \to 0$. Since $S = O(\epsilon)$ we have the integral is $O(\epsilon \log(\epsilon))$. Taking the factor multiplying this integral into account the leading order of this factor is $O(k)$. So for small k this term will never be present at leading order leaving only the term corresponding to the impermeable solution present.

The impermeable part of this solution for ϕ is:

$$\begin{aligned}
&\sqrt{d^2 - x^2} \\
=&\sqrt{d^2 - (d + \epsilon^2 x_j)^2} \\
=&\epsilon\sqrt{-2dx_j - \epsilon^2 x_j} \\
=&\epsilon\left(\sqrt{-2dx_j} + O(\epsilon^2)\right),
\end{aligned} \tag{7.45}$$

valid for $x_j < 0$, with $d = O(1)$ we have the leading order to be $O(\epsilon)$. Thus our matching condition at leading order is:

$$\epsilon^n\left(\phi_j + \dot{d}x_j\right) = \epsilon\sqrt{-2dx_j} \tag{7.46}$$

$$\phi_j(x, 0, t) = \sqrt{-2dx_j} - \dot{d}x_j, \tag{7.47}$$

to achieve balance, the power $n = 1$. We have our substrate condition given by:

$$\phi_y = 1 + kd\phi_t, \tag{7.48}$$

after substituting in our new scaled variables we have:

$$\frac{1}{\epsilon}\phi_{j_{y_j}} = 1 + \epsilon kd\left(\phi_{j_t} + \ddot{d}x_j\right) \tag{7.49}$$

$$\phi_{j_{y_j}} = \epsilon + \epsilon^2 kd\left(\phi_{j_t} + \ddot{d}x_j\right) \tag{7.50}$$

$$\phi_{j_{y_j}} = 0 + O(\epsilon). \tag{7.51}$$

On the free surface we have $\phi_y = \eta_t$, after substituting our scales in we have:

$$\phi_{j_{y_j}} = \epsilon\eta_{j_t} = 0 + O(\epsilon). \tag{7.52}$$

Substituting these scales into our governing equations we have:

$$\nabla^2\phi = 0 \qquad \text{in the droplet,} \tag{7.53}$$

$$\phi_y = 0 \qquad \text{on flow boundries,} \tag{7.54}$$

$$|\nabla\phi| = \dot{d} \qquad \text{on the free surface.} \tag{7.55}$$

To solve this system we use a hodograph plane. We define a complex potential $W = \phi + i\psi$ and the complex velocity $U = \frac{dW}{d\zeta} = \phi_x - i\phi_y$ with $\zeta = x + iy$. The complex velocity plane corresponds to the semi-circle ${\phi_X}^2 + {\phi_y}^2 = \dot{d}^2$ with $-\phi_y > 0$. In the far field $x^2 + y^2 \to \infty$ corresponds to $U = -\dot{d}$ since we are in a frame of reference moving with the turnover point our far-field will be stationary. We assume that the jet thickness approaches a constant thickness, H_j as $x \to \infty$ and from the dynamic boundary condition (7.55) we have $\phi_y \to 0$ and $\phi_x \to \dot{d}$. The kinematic condition (7.54) shows that the stream function is independent of x and y on the interface between the fluid and both the substrate and the air. Let $\psi(x, y, t) = 0$ on the substrate-liquid interface and $\psi(x, y, t) = f(t)$ on the free surface, where $f(t)$ is unknown.

Knowing the behaviour of the jet velocities we have:

$$\phi_x = \psi_y = \dot{d}, \tag{7.56}$$

$$[\psi]_{y=0}^{y=H_j} = \left[\dot{d}y\right]_{y=0}^{y=H_j}, \tag{7.57}$$

$$f(t) = \dot{d}H_j. \tag{7.58}$$

From the matching condition (7.47) we have:

$$W(\zeta) = \sqrt{-2d\zeta} - \dot{d}\zeta, \tag{7.59}$$

$$U(\zeta) = \frac{dW}{d\zeta} = -\dot{d} - d(-2d\zeta)^{-\frac{1}{2}}, \tag{7.60}$$

rearranging (7.60) we have:

$$\zeta = \frac{-1}{2d}\left(\frac{\dot{d} + U}{d}\right)^{-2}. \tag{7.61}$$

Substituting this into (7.59) to eliminate ζ we have:

$$W = \frac{\dot{d}d}{2}\left(\dot{d}+U\right)^{-2} + \frac{d}{\dot{d}+U} \tag{7.62}$$

$$W \approx \frac{\dot{d}d}{2}\left(\dot{d}+U\right)^{-2}, \tag{7.63}$$

since we are considering as $U \to -\dot{d}$ the dominant term we have taken is the more singular term.

Consider:

$$U = \frac{dW}{d\zeta} = \frac{dW}{dU}\frac{dU}{d\zeta}, \tag{7.64}$$

$\frac{dW}{dU}$ will be zero at the stagnation point, $U = 0$ given $\frac{dU}{d\zeta} \neq 0$. We split W into a sum of two parts, let $W(U) = W_1(U) + W_2(U)$, with:

$$W_1 = -\frac{dU(U+\dot{d})^{-2}}{2}, \tag{7.65}$$

$$W_2 = -\frac{2f(t)}{\pi}\log\left(\frac{\dot{d}-U}{\dot{d}+U}\right), \tag{7.66}$$

with W_1 having the correct behaviour as $U \to -\dot{d}$ on the boundary and W_2 satisfies the condition on W when $|U| = \dot{d}$. Close to the stagnation point, $U = 0$ by looking at a Taylor expansion of these function we have:

$$W_1 \approx -\frac{dU}{2\dot{d}^2}, \tag{7.67}$$

$$W_2 \approx \frac{4f(t)U}{\pi\dot{d}}. \tag{7.68}$$

We have the condition at the stagnation point $\frac{dW}{dU} = 0$, so we have:

$$\frac{dW_1}{dU} + \frac{dW_2}{dU} = 0 \tag{7.69}$$

$$-\frac{d}{2\dot{d}^2} + \frac{4f(t)}{\pi\dot{d}} = 0 \tag{7.70}$$

$$f(t) = \frac{\pi d}{8\dot{d}}\ . \tag{7.71}$$

From (7.58) we have now found that the jet thickness is given by:

$$H_j(t) = \frac{\pi d(t)}{8\dot{d}(t)^2}. \tag{7.72}$$

We have $d(t) = (2 - 1.803k)\sqrt{t}$ with $k = O(\epsilon)$, expanding our jet thickness in powers of ϵ we have:

$$\begin{aligned} H_j &= \frac{\pi t^{\frac{3}{2}}}{2} \frac{1}{2 - 1.803k} \\ &= \frac{\pi t^{\frac{3}{2}}}{2} \left(\frac{1}{2} + \frac{1.803k}{4} + O(\epsilon^2) \right) \qquad (7.73) \\ H_j &= \frac{\pi t^{\frac{3}{2}}}{4} + k \frac{1.803 \pi t^{\frac{3}{2}}}{8} + O(\epsilon^2). \qquad (7.74) \end{aligned}$$

The volume flux of the jet can be calculated, we can integrate the velocity of the jet over the thickness. Assuming that the jet thickness tends to H_j quickly we have:

$$\begin{aligned} \psi_j &= \int_0^{H_j} \dot{d}(t) dy \\ &= \dot{d} H_j \qquad (7.75) \\ \psi_j &= \frac{\pi t}{4}. \qquad (7.76) \end{aligned}$$

This flux is independent of k and equal to the flux of the jet on a impermeable substrate. We have that for a porous substrate the jet is thicker, however, the fluid has a lower velocity.

7.5 Conclusions

In this Chapter we have presented and solved a model of the post-impact behaviour. The governing equations for an impact with a general substrate were formulated. These general equations can be modified to give the equations for impermeable or more complicated substrates. Firstly we solved the case for an impact with an impermeable substrate. Complex analysis methods were used to solve this system of equations to obtain the free surface deformations and velocity fields. We then went on to formulate and solve the case with a porous substrate. We used a simple approximation for the substrate condition. Upon comparing these result to that of the

impermeable case the rate which the droplet spreads out on the substrate is given by $\dot{d}(t)$, for all values of permeability we have this function, (7.29), is strictly less than the same function for the impermeable case. This can be explained simply because we are allowing fluid to enter the substrate, so we have less overall fluid in the droplet. This reduced fluid in the droplet is also reflected in the free surface shapes, Figure 7.10 displays this difference. In the jet region we found that the jet's volume flux remains constant for any k although we also found that the thickness increases as k increases. Despite the constant volume flux of the jet, independent of the value of k, an increase in k leads to a thicker and slower jet.

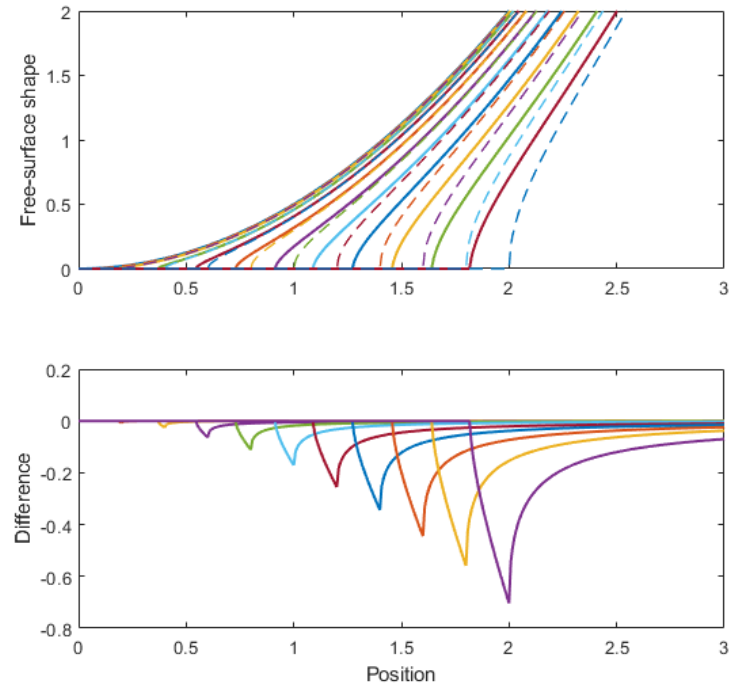

(a) $k = 0.1$ free-surface comparison

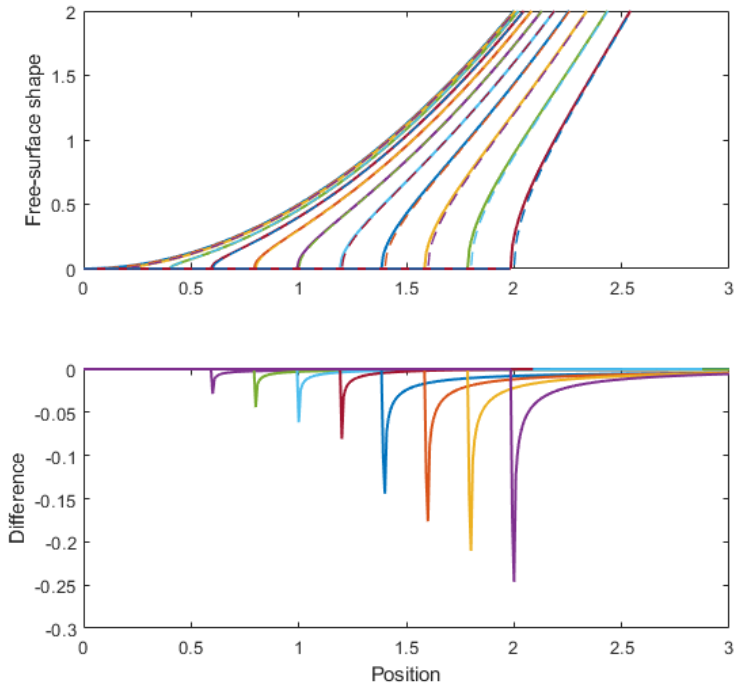

(b) $k = 0.01$ free-surface comparison

Figure 7.2: Upper panels show comparisons between the impermeable (dashed curves) and porous (solid curves) solutions the same time steps. Lower panels show the difference between the two solutions.

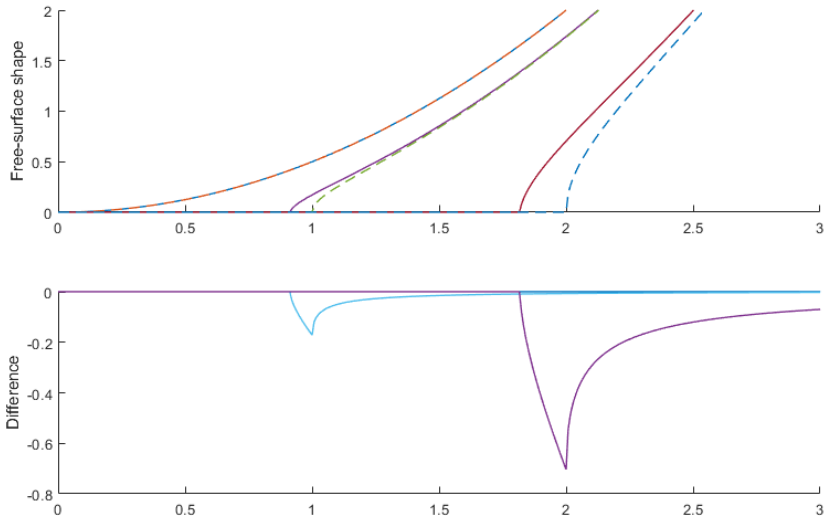

Figure 7.3: A view at particular time steps to show more clearly the differences in the free-surface shapes between the impermeable solution and the $k = 0.1$ porous solution.

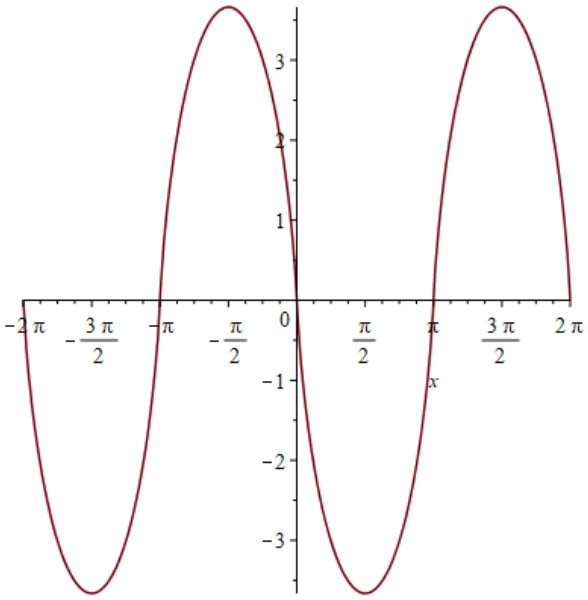

Figure 7.4: This plot shows a plot for $I(\theta)$, which is a function of $\theta = \arccos\left(\frac{x}{d}\right)$, which is an angle in the interval $0 < \theta < \pi$ from equation (7.35).

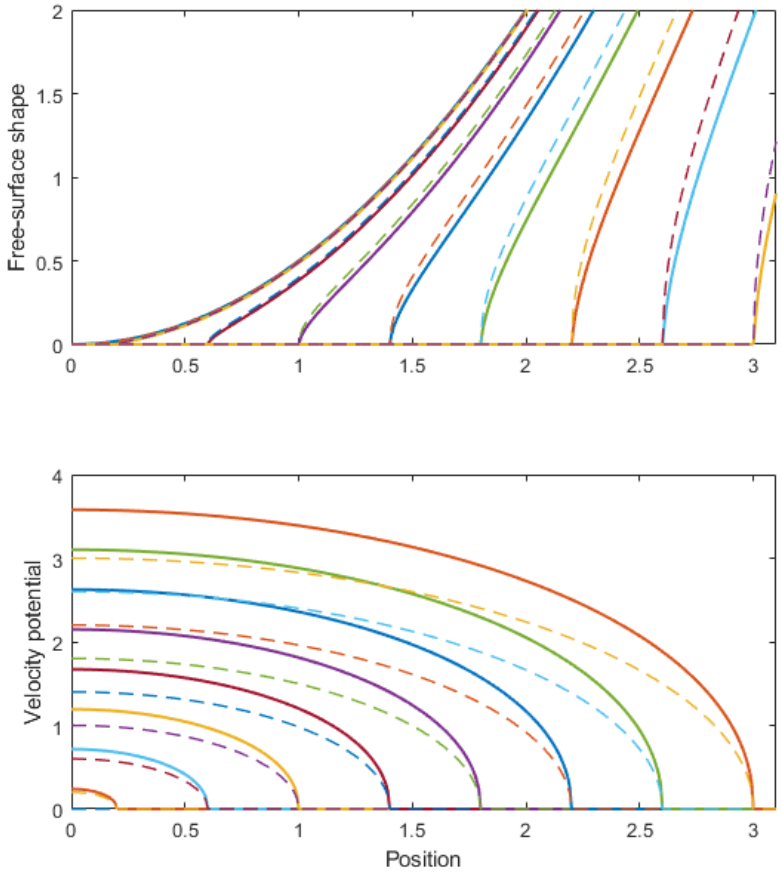

Figure 7.5: Comparison between $\phi(x,t)$ for impermeable (dashed curves) and porous (solid curves) solutions, here $k = 0.1$.

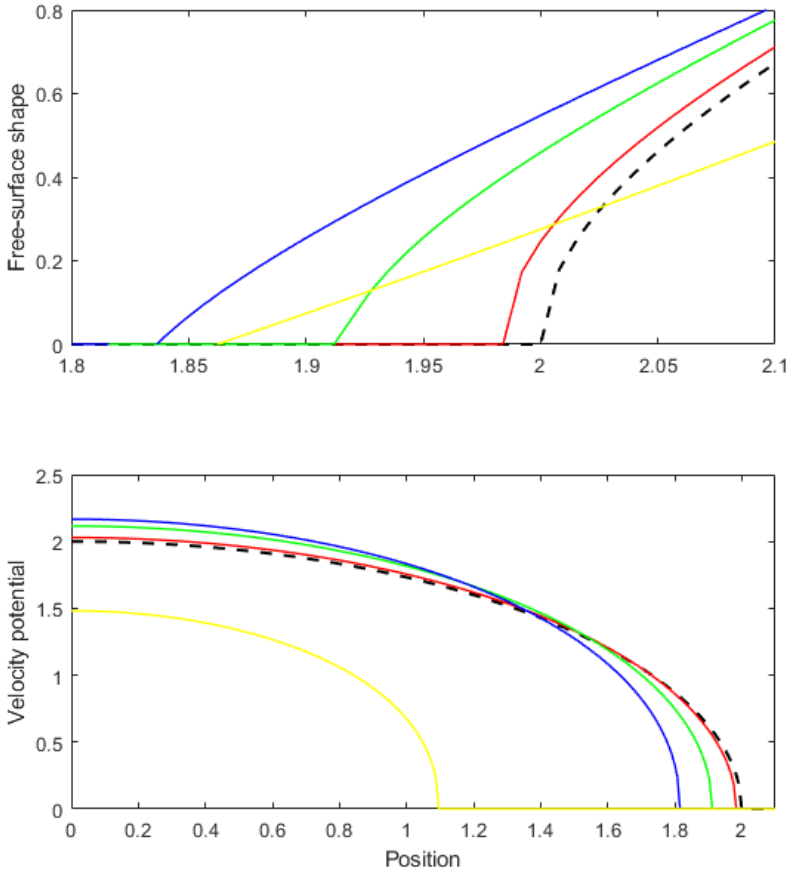

Figure 7.6: Comparing the solutions for varying the porosity for like times for $k = 0.001, 0.05, 0.5$ corresponding to red, green, blue and yellow lines. The dashed line represents the impermeable case.

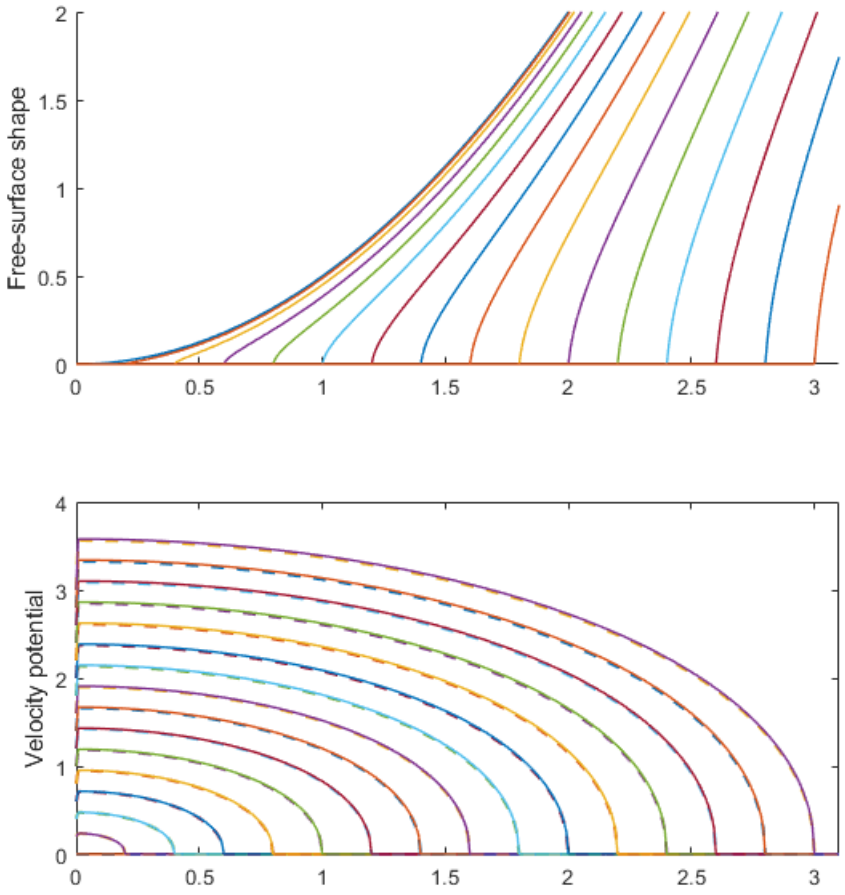

Figure 7.7: Comparison between using the estimated series approximation ((7.36) and (7.34) and numerical integration when solving for ϕ.

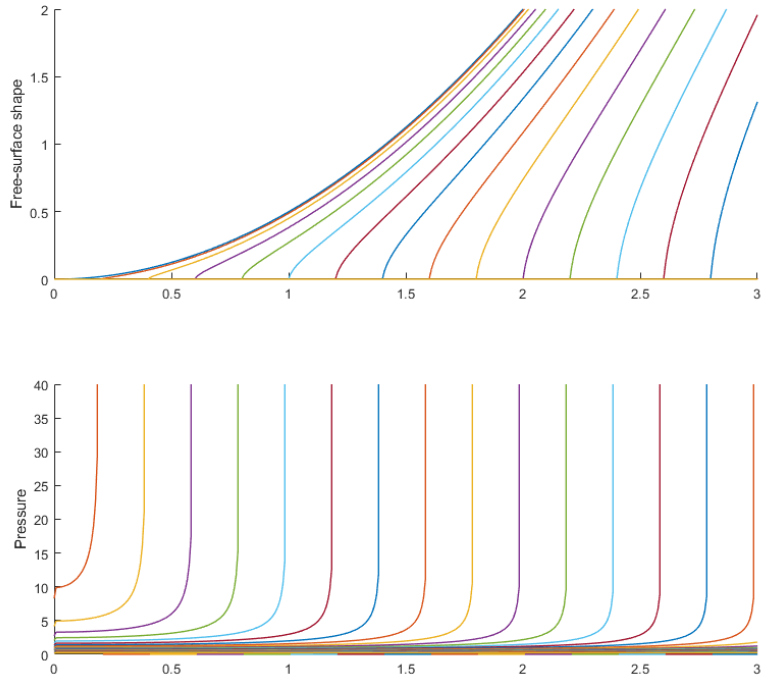

Figure 7.8: A plot for the pressure as a function of x for increasing times.

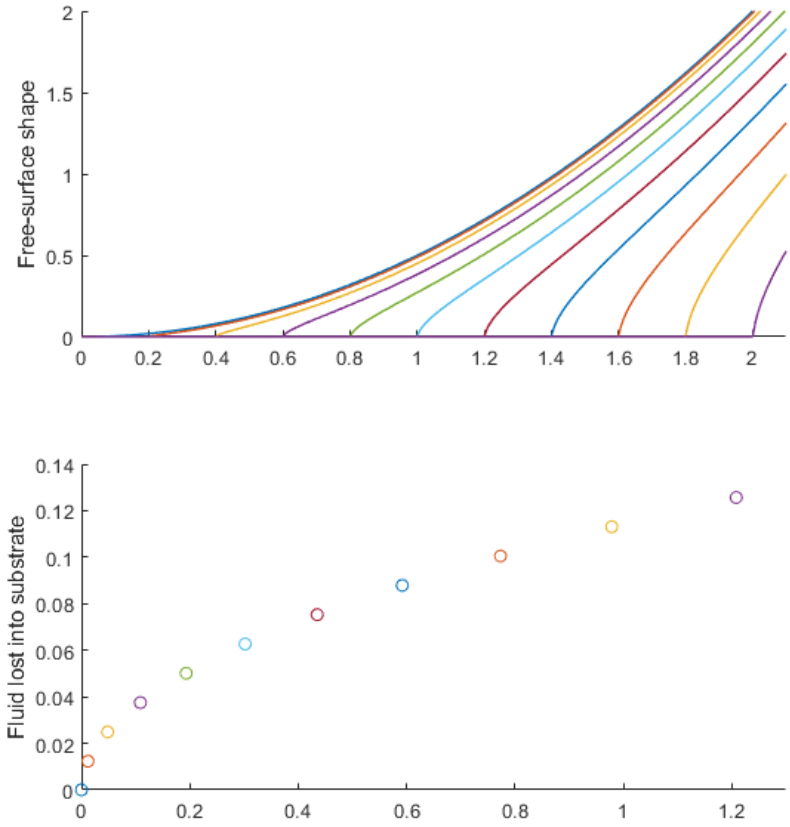

Figure 7.9: Plot showing the instantaneous rate of flow of fluid into the substrate as a function of time, in the lower panel.

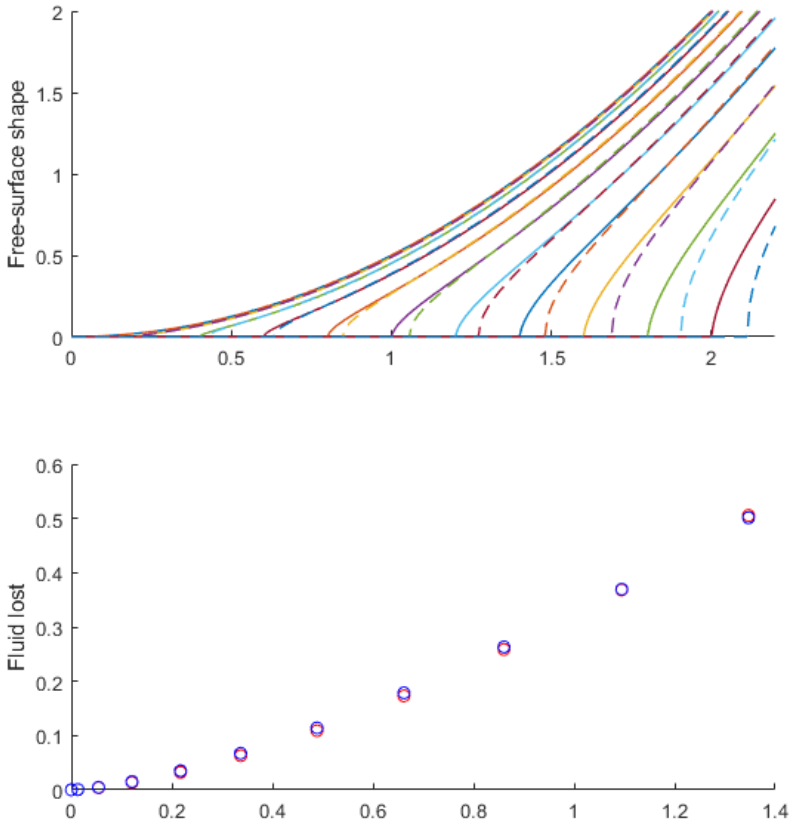

Figure 7.10: Plot comparing the fluid lost into the substrate using different methods, the symbols are so close they are indistinguishable.

8

Conclusions and further study

8.1 Conclusions

In this thesis various cases for pre- and post-impact droplet dynamics were considered. At the start we considered a typical droplet impact and included surface tension and obliqueness in the derivations of the coupled equations to solve. These were solved numerically showing how obliqueness makes touchdown happen faster and surface tension making the touchdown slower. In Chapter 3 we considered a shallow-water layer impact. Here we obtained a different system of equations and considered the effect of obliqueness which has not been looked at with this case before. We found results that agreed with the obliqueness addition from Chapter 2, seeing an acceleration into touchdown. In chapter 4 we considered the shallow-water impact onto a porous media which again hasn't been considered before. Interesting behaviour was seen when the porous layer depth and porosity were varied giving rise to regions of delayed touchdown time. In Chapter 5 we considered thicker porous layers, initially deriving the system for an intermediate depth layer before considering an infinitely deep layer. We observed the effects of varying the porosity and depth of these layers and the unexpected behaviour of changing the layer depth. The entry of air, forced into the substrate, and the exiting of air from the substrate as fast narrow jets, are all new discoveries.

Chapter 6 considered the post-impact dynamics of a droplet impact.

Using Wagner theory to close the problem, the system was derived and solved analytically for the simple case of an impermeable substrate. Chapter 7 considered the introduction of a porous base for the post-impact dynamics. This has not been studied before, we used an approximation for the velocity of the liquid entering the substrate. The system for this problem was derived and solved numerically. The jet region caused from this impact was also considered which gave an interesting relationship between the jets with a porous base and with an impermeable base.

8.2 Further study for pre-impact dynamics

To add to the content covered in chapter 2, future work could look at the case of having both obliqueness and surface tension. This would be an interesting case to consider given each of the two physical effects (obliqueness and surface tension) has an opposite influence on touchdown time. Running both surface tension and obliqueness numerically is difficult with the methods used to solve them separately so another method of solving these would have to be used. Similarly considering the shallow-water layer impact with surface tension would be interesting but suffers from the same problem of it being difficult to solve without a very different numerical method. Other regimes for the fluids such as compressible or inviscid air would be interesting modifications to the current theory.

8.3 Further study for post-impact dynamics

To begin looking at more accurate physical models that include substrate dynamics for porosity there are two cases we will consider. First, a dry porous layer where the substrate is occupied by air (which we are ignoring); secondly, a wet porous layer, where the substrate is pre-saturated with the same fluid as the droplet.

In each case we have three sub-cases depending on the depth of the substrate. We have thin, where the depth is order of magnitude smaller than the width; intermediate, where the width and depth are comparable; and deep, where we have infinite depth substrate. In all cases we have a mixed boundary value problem, the aim is to calculate the velocity, ϕ_y, of the fluid entering the substrate for the contact region. For the intermediate case the full Laplace's equation in a rectangle needs to be solved for both cases. Here we define the subscript $_s$ to refer to substrate quantities and $_d$ to refer to droplet quantities, v is the vertical velocity component and p is the pressure.

Inside the contact region on $y = 0$ and $-d < x < d$ the pressure in the droplet is approximated by $p_d = -\phi_t$ from Bernoulli's equation. We assume Darcy flow inside the substrate and so we have:

$$\nabla^2 p_s = 0 \qquad \text{in substrate,} \tag{8.1}$$

$$v_s = v_d \qquad \text{on } y = 0 \text{ and } |x| < d, \tag{8.2}$$

$$p_s = p_d \qquad \text{on } y = 0 \text{ and } |x| < d, \tag{8.3}$$

$$p = 0 \qquad \text{on } y = 0 \text{ and } |x| > d, \tag{8.4}$$

$$\phi = 0 \qquad \text{on } y = 0 \text{ and } |x| > d. \tag{8.5}$$

8.3.1 Dry substrate

In a dry porous medium when the droplet makes contact there will be a free surface that moves through the medium, let this free-surface be $y = g(x, t)$, since this is a free surface we have that $p_s(x, t) = 0$ on $y = g(x, t)$. So we have in the substrate:

$$\nabla\phi_s = 0, \qquad \text{in substrate,} \tag{8.6}$$

$$v_s(x,0,t) = v_d(x,0,t) \qquad \text{in wetted region,} \tag{8.7}$$

$$P_s(x,g(x,t),t) = 0, \tag{8.8}$$

$$v_s = g_t + u_s g_x \qquad \text{from the kinematic condition,} \tag{8.9}$$

$$P_s(x,0,t) = p_a(x,0,t) \qquad \text{outside of the wetted region.} \tag{8.10}$$

8.3.2 Saturated porous

With a saturated porous layer of depth H we have alternative boundary conditions for the layer. At the bottom we expect a zero normal velocity component on $y = -H$ and the flow to tend to zero as we move far away from the contact region, we also have an initial condition that the flow is stationary. So we have:

$$v_s = 0 \qquad \text{on } y = -H, \tag{8.11}$$

$$u_s, v_s \to 0 \qquad \text{as } |x| \to \infty, \tag{8.12}$$

$$u_s = v_s = 0 \qquad \text{at } t = 0. \tag{8.13}$$

From the conservation of mass, we would expect jets to come out of the substrate (to compensate for the droplet entering it).

8.3.3 Air effects

In the models presented in chapters 6 and 7 we have neglected the air. With the inclusion of air we would have some minor resistance and deformation of the free surface of the droplet. We would also have jets of air exiting the dry region of the substrate. These jets would disrupt the jets of fluid along the substrate and the free surface of the drop would would change the dynamics of the problem considerably. Further work could be done to investigate the problem with the incorporation of air.

Bibliography

D Acheson (1990), Elementary Fluid Dynamics, *Oxford University Press*

D Bartolo, C Josserand and D Bonn (2005), Retraction dynamics of aqueous drops upon impact on non-wetting surfaces, *J. Fluids Mech.*, vol **545**, pp 329–338

G S Beavers and D D Joseph (1967), Boundary conditions at a naturally permeable wall, *J. Fluid Mech.*, vol **30**, pp 197-207

P Brunet, F Lapierre, F Zoueshtiagh, V Thomy and A Merlen (2009), To grate a liquid into tiny droplets by its impact on a hydrophobic microgrid, *Appl. Phys. Lett.*, vol **95**, 254102

G F Carrier, M Krook and C E Pearson (2005), Functions of a Complex Variable: Theory and Technique, *Society for Industrial and Applied Mathematics*

M V Chubynsky, K I Belousov, D A Lockerby and J E Sprittles (2020), Bouncing off the Walls: The Influence of Gas-Kinetic and van der Waals Effects in Drop Impact, *Phys. Rev. Lett.*, vol **124**, 084501

R Cimpeanu and M R Moore (2020), Early-time jet formation in liquid-liquid impact problems, theory and simulations, *J. Fluid Mech.*, vol **865**, pp 764–796

D B van Dam and C Le Clerk (2004), Experimental study of the impact of an ink-jet printed droplet on a solid substrate, *Phys. Fluids*, vol **16**, pp 3403-3414

L Duchemin and C Josserand (2011), Curvature singularity and film-skating during drop impact, *Phys. Fluids*, vol **23**, 011704

J W Elliott and F T Smith (2015), Ice formation on a smooth or rough cold surface due to the impact of a supercooled water droplet, *J. Eng. Math.*, vol **102**, pp 35-64

R W Gent, N P Dart and J T Cansdale (2000), Aircraft icing, *Phil. Trans. R. Soc. Lond. A*, vol **358**, pp 2873-2911

I S Gradshteyn and I M Ryzhik (2000), Table of Integrals, Series, and Products, *Academic Press*, Section 3.723

M Grizen, T Maitra, J P Bradley and M K Tiwari (2020), Nanotextured Aluminium-Based Surfaces with Icephobic Properties, *Heat Transfer Engineering*, vol **41**, pp 1663-1672

J Hao , J Lu, L Lee, Z Wu, G Hu and J M Floryan (2019), Droplet splashing on an inclined surface, *Phys. Rev. Lett.* **122**, 054501

N I J Henman, F T Smith, M K Tiwari (2021), Pre-impact dynamics of a droplet impinging on a deformable surface, available at https://arxiv.org/abs/2104.01594v4, accessed 19/09/21

P D Hicks and F T Smith (2011), Skimming impacts and rebounds on shallow liquid layers, *Proc. R. Soc. A*, vol **467**, pp 653-674

P D Hicks and R Purvis (2010), Air cushioning and bubble entrapment in three-dimensional droplet impacts, *J. Fluid Mech.*, vol **649**, pp 135-163

P D Hicks and R Purivs (2011), Air cushioning in droplet impacts with liquid layers and other droplets, *Phys. Fluids*, vol **23**, 062104

P D Hicks, E V Ermanyuk, N V Gavrilov and R Purvis (2012), Air trapping at impact of a rigid sphere onto a liquid, *J. Fluid Mech.*, vol **695**, pp 310-320

P D Hicks and R Purvis (2013), Liquid-solid impacts with compressible gas cushioning, *J. Fluid Mech.*, vol **735**, pp 120-149

P D Hicks and R Purvis (2015), Gas-cushioned droplet impacts with a thin layer of porous media, *J. Eng. Math.*, vol **102**, pp 65-87

S D Howison, J R Ockendon and S K Wilson (1991), Incompressible water-entry problems at small deadrise angles, *J. Fluid Mech.*, vol **222**, pp 215-230

S D Howison, J R Ockendon, J M Oliver, R Purvis and F T Smith (2005), Droplet impact on a thin fluid layer, *J. Fluid Mech.*, vol **542**, pp 1-23

C Josserand and S T Thoroddsen (2016), Drop Impact on a Solid Surface, *Ann. Rev. Fluid Mech.*, vol **48**, pp 365-391

T Von Karman (1929), The impact on Seaplane floats during landing, *NACA*, Technical notes **321**

D J Knox, S K Wilson, B R Duffy and S McKee (2015), Porous squeeze-film flow, *IMA J. Appl. Math.*, vol **80**, pp 376-409

A A Korobkin (1999), Shallow-water impact problems, *J. Eng. Math.*, vol **35**, pp 233-250

A A Korobkin, A S Ellis and F T Smith (2008), Trapping of air in impact between a body and shallow water, *J. Fluid Mech.*, vol **611**, pp 365-394

J S Lee, B M Weon, J H Je and K Fezzaa (2012), How does an air film evolve into a bubble during drop impact?, *Phys. Rev. Lett.*, vol **109**, 204501

M B Lesser and J E Field (1983), The impact of compressible liquids, *Ann. Rev. Fluid Mech.*, vol **15**, pp 93-122

E Q Li and S T Thoroddsen (2015), Time-resolved imaging of a compressible air disc under a drop impacting on a solid surface, *J, Fluid Mech.*, vol **780**, pp 636–648

J O Marston, S T Thoroddsen, W K Ng and R B H Tan (2010), Experimental study of liquid drop impact onto a powder surface, *Powder technology*, vol **203**, pp 223-236

M R Moore (2014), New mathematical models for splash dynamics, *Dphil thesis, Oxford University*

L Mouzai and M Bouhadef (2003), Water drop erosivity: Effects on soil splash, *J. Hydraul. Res.*, vol **41**, pp 61-68

M J Negus, M R Moore, J M Oliver and R Cimpeanu (2020), Droplet impact onto a spring-supported plate:analysis and simulations, *J. Eng. Math.* vol **128**, article 3

J M Oliver (2002), Water entry and related problems, *DPhil thesis, Oxford University*

J M Oliver (2007), Second-order wagner theory for two-dimensional water-entry problems at small deadrise angles, *J. Fluid Mech.*, vol **572**, pp 59-85

S Parker and J Nally (2012), Liquid interactions with porous media and the fate of toxic materials, report from the European Study Group (ESGI) 85, available at www.cimr.uea.ac.uk/workshops/esgi85/liquid-interactions, accessed (20/07/2021)

M Pegg, R Purvis, A Korobkin (2018), Droplet impact onto an elastic plate: a new mechanism for splashing, *J. Fluid Mech.*, vol **839**, pp 561-593

R Purvis and F T Smith (2004), Large droplet impact on water layers, 42nd AIAA Aerospace Sciences Meeting and Exhibit

R Purvis and F T Smith (2004), Air-water interactions near droplet impact, *Euro. Jnl of Applied Mathematics (2004)*, vol **15**, pp 853-871

R Purvis and F T Smith (2005), Droplet impact on water layers: post-impact analysis and computations, *Phil. Trans. R. Soc. A*, vol **363**, pp 1209-1221

R Ramachandran, K Sobolev and M Nosonovsky (2015), Dynamics of Droplet Impact on Hydrophobic/Icephobic Concrete with the Potential for Superhydrophobicity, *Langmuir*, vol **31**, pp 1437-1444

P G Saffman (1971), On the boundary condition at the surface of a porous medium, *Stud. Appl. Math*, vol **50**, pp 93-101

F T Smith, L Li and G X Wu (2003), Air cushioning with a lubrication/inviscid balance, *J. Fluid Mech.*, vol **482**, pp 291-318

S C Tan, M Papadakis, D Miller, T Bencic, P Tate and M C Laun (2007), Experimental study of large droplet splashing and breakup, *AIAA-2007-904, AIAA conference, Reno, 2007*

S T Thoroddsen, T G Etoh and K Takehara (2003), Air entrapment under an impacting drop, *J. Fluid Mech.*, vol **478**, pp 125-134

S T Thoroddsen, T G Etoh, K Takehara, N Ootsuka and Y Hatsuki (2005), The air bubble entrapped under a drop impacting a solid surface, *J. Fluid Mech.*, vol **545**, pp 203-212

J M Vanden-Broeck, F T Smith (2008) Surface tension effects on interaction between two fluids near a wall, *QJMAM*, vol **61**, pp 117-128

H Wagner (1932), Phenomena associated with impacts and sliding on liquid surfaces, *Z. Angew. Math. Mech.*, vol **12**, pp 193-215

R J M De Wiest (1969), Flow Through Porous Media, *Academic Press*

S K Wilson (1989), The mathematics of ship slamming, *DPhil thesis, Oxford University*

S K Wilson (1991), A mathematical model for the initial stages of fluid impact in the presence of a cushioning fluid layer, *J. Eng. Math.*, vol **25**, pp 265-285

A M Worthington and R S Cole (1900), Impact with a liquid surface studied by the aid of instantaneous photography, *Phil. Trans. R. Soc. A*, vol **194**, pp 175-199

L Xu, W W Zhang and S R Nagel (2005), Drop Splashing on a Dry Smooth Surface, *Phys. Rev. Lett.*, vol **94**, 184505

W Zhao, S Lin, L Chen, E Li, S T Thoroddsen and M Thoraval (2020), Jetting from an impacting drop containing a particle, *Phys. Fluids*, vol **32**, pp 011704